POLITECNICO DI MILANO

School of Industrial and Information Engineering

Master of Science in
Materials Engineering and Nanotechnology

Development of Tantalum-Doped Titanium Oxide Nanostructures for Plasmonic Applications

Supervisor:
Prof. Andrea Li Bassi

Co-supervisor:
Beatrice Bricchi

Graduation thesis of:

Federico Gaetani
899509

Academic Year 2018 - 2019

Abstract

Shortcomings of metals (namely interband and intraband losses) as materials for plasmonic applications have spurred research into novel materials for these purposes. Among the most promising candidates as plasmonic materials, transparent conductive oxides (TCOs) are particularly notable due to their high carrier density and behavior tunability. While today's TCO market revolves around the manufacturing of flat panel displays and thin film solar cells, research is being made on more exotic applications of this material class, of which plasmonics is one example. The most studied materials in this framework are indium tin oxide, aluminum zinc oxide and gallium zinc oxide. Starting from the early 2000s, titanium oxide based TCOs were investigated as well. While substoichiometric titanium oxide is naturally conductive, it is by doping it with niobium or tantalum that electrical properties comparable to those of top notch TCOs are obtained. In particular, tantalum doped titanium oxide seems to be a promising material in the field of plasmonics, because of its high doping efficiency and low effective mass for the donor electron, two key properties when it comes to tune the plasmonic response of the material to external stimuli. This thesis work aims to expand the knowledge about tantalum doped titanium oxide (TaTO) in the light of future plasmonic applications. Thin films of this material were deposited by the pulsed laser deposition (PLD) method, which allows to finely tune the stoichiometry and the morphology of the deposited films.

Two main themes were explored: the deposition of nanoporous films and nanoparticle assemblies, and the creation of bilayered and multilayered films. The main aim of the first topic was to obtain crystalline anatase nanostructures – and as an ultimate goal, anatase nanoparticles – with a high carrier density (which is key when plasmonic applications are envisioned). Doing so is problematic when PLD is used, as the prime strategy for obtaining high specific surface structures consists in having a high pressure inside the deposition chamber. If the in-chamber gas is oxygen, the nanostructures will end up being stoichiometric and with a low carrier density, despite the presence of a dopant. The idea of depositing in a mixed argon-oxygen atmosphere is presented in this work: such strategy would allow to obtain porous structures while keeping the oxygen partial pressure low. The pressure range spanning from 4 Pa to 15 Pa was explored, and a comparison between deposition in pure oxygen and a mixed atmosphere was made. The effect of different post-annealing treatments was studied as well. This strategy was not successful as expected. Deposition at high pressures resulted in the formation of significant rutile and amorphous fractions. It is still unclear whether the bad crystallization of the nanostructures was due to an incorrect mixture in the deposition atmosphere, or rather to the post-annealing treatment. A belated study on *capped* nanostructures, (i.e. covered by a compact layer) pointed towards the second hypotesis. The second topic covered by this thesis work concerns the synthesis of dielectric-TCO interfaces, achieved by in-series deposition of doped and undoped titania. This configurations should be able to sustain plasmonic excitations known as surface plasmon polaritons (SPPs). While the actual activation and observation of such excitations goes beyond the scope of this work, single dielectric-TCO interfaces, as well as multiple ones (the latter, at the base of metamaterials), were successfully deposited. Presumed plasmonic interfaces were obtained from the juxtaposition of different materials or by inducing a planar discontinuity in the properties of the same material. One particular material couple – substoichiometric TaTO and stoichiometric titania – was chosen in order to attempt the deposition of ultrathin TaTO films. The core idea behind this strategy was that a lattice matching substrate would allow for an optimal film percolation and thus pave the way to sub 10 nm conductive thin films. This goal was unfortunately not reached, however this study shed light on the reciprocal interface behavior of titania and TaTO.

Estratto in lingua italiana

Le limitazioni dei metalli (nello specifico, dissipazioni dovute alle transizioni interbanda e intrabanda) come materiali plasmonici ha stimolato la ricerca di materiali alternativi per queste applicazioni. Tra i candidati più promettenti come materiali plasmonici alternativi ai metalli, i TCO (*transparent conductive oxides*) rivestono un ruolo di primo piano, per via dell'elevata densità di portatori e per la possibilità di regolare in maniera fine la loro risposta plasmonica. Anche se la più grande fetta del mercato dei TCO ruota intorno al loro impiego nella manifattura di schermi piatti e celle solari a film sottile, è prolifica la ricerca riguardo applicazioni più esotiche di questa classe di materiali, e la plasmonica ne è un esempio. I materiali più studiati in questo contesto sono l'ossido di indio e stagno, l'ossido di zinco drogato alluminio e l'ossido di zinco drogato gallio. A partire dai primi anni 2000, inoltre, è stato esplorata la possibilità di impiegare il biossido di titanio come TCO. Questo materiale è moderatamente conduttivo quando sottostechiometrico; tuttavia, è drogandolo con niobio o tantalio che si possono ottenere proprietà elettriche paragonabili a quelle dei migliori TCO. In particolare, il biossido di titanio drogato tantalio sembra essere promettente per applicazioni plasmoniche, grazie alla sua elevata efficienza a drogaggio e alla ridotta massa efficace degli elettroni di conduzione, due proprietà fondamentali per controllare in maniera fine la risposta plasmonica del materiale a stimoli esterni.

Questo lavoro di tesi mira ad ampliare le conoscenze sul biossido di titanio drogato tantalio (TaTO) alla luce di future applicazioni plasmoniche. Film sottili di questo materiale sono state depositate mediante *pulsed laser deposition* (PLD). Questa tecnica permette di controllare in maniera fine la stechiometria e la morfologia di film sintetizzati. Due argomenti principali sono stati affrontati: la deposizione di film nanoporosi e sistemi di nanoparticelle, e la realizzazione di film bi-strato o multistrato. Lo scopo principale del primo tema è stato quello di sintetizzare nanostrutture cristalline in fase anatasio – con l'idea di lungo termine di ottenere *nanoparticelle* – ad elevata densità di portatori (fondamentale per applicazioni plasmoniche). Questo processo non è scontato quando si utilizza la PLD, poiché la principale strategia usata per ottenere strutture ad elevata superficie specifica consiste nell'aumentare la pressione all'interno della camera di deposizione. Se il gas in camera è ossigeno, le nanostrutture depositate risulteranno essere stechiometriche e caratterizzate da una bassa densità di portatori, nonostante la presenza di una agente drogante. In questo lavoro è proposta l'idea di depositare in una atmosfera mista di argon-ossigeno: questo accorgimento renderebbe possibile ottenere strutture porose mantenendo bassa la pressione parziale dell'ossigeno. L'intervallo di pressioni compreso tra 4 Pa e 15 Pa è stato indagato, così come è stato fatto un paragone tra deposizioni condotte in ossigeno puro e in miscela. Inoltre, è stato studiato l'effetto di diversi trattamenti termici. Questa strategia non ha avuto il successo sperato. La deposizione a pressioni elevate ha portato alla formazione di frazioni significative di rutilo e fase amorfa. Non è stato possibile stabilire se la cattiva cristallizzazione delle nanostrutture è da imputare ad una composizione non ottima dell'atmosfera di deposizione o ad un effetto dovuto al trattamento termico. Uno studio tardivo su nanostrutture *protette* (cioè coperte da un film compatto) sembra indicare verso la seconda ipotesi. Il secondo argomento trattato in questo lavoro riguarda la sintesi di interfacce dielettrico-TCO, realizzata attraverso la deposizione in serie di TiO_2 e TaTO. Queste configurazioni dovrebbero essere in grado di sostenere le eccitazioni plasmoniche superficiali note come SPP (dall'inglese *surface plasmon polariton*), anche se l'attivazione e l'osservazione di tali stati esula dagli obiettivi di questo lavoro di tesi. Interfacce dielettrico-TCO (presumibilmente capaci di sostenere modi SPP) sono state sintetizzate con successo sovrapponendo materiali diversi o creando discontinuità planari all'interno dello stesso materiale. In aggiunta, una tra queste coppie di materiali – più precisamente TiO_2 stechiometrico e TaTO sottostechiometrico - è stata scelta come punto di partenza per la deposizione di film ultrasottili di TaTO. L'idea di fondo dietro questo approccio è il fatto che un substrato avente la medesima struttura cristallina del film può favorire una percolazione ottimale di quest'ultimo, e pertanto aprire la strada alla deposizione di film con spessore inferiore a 10 nm. Questo obiettivo non è stato raggiunto, ma questo studio ha fatto maggior chiarezza sul reciproco comportamento all'interfaccia di TiO_2 e TaTO.

Contents

List of Figures

List of Tables

Introduction

Plasmonics is a discipline of physics that studies the entangled behavior of electromagnetic fields and oscillations of conduction electrons. When we speak of conduction electrons, we generally refer to a system in which electrons are not participating into a covalent or ionic bond, but can, while still interacting with the ions, move freely. This happens in plasmas (hence the name) but also in condensed matter, for example in metals. In these cases, electrons possess collective behaviors known as *plasma oscillations*. These oscillations are characterized by a frequency known as *plasma frequency* (ω_P) which depends on the electronic number density, on the permittivity of the surrounding medium and on the effective mass of the electron in that given system. When a so described particle system interacts with an electromagnetic field whose frequency is close to ω_P, a separate description of the two systems is not possible: we say they are *coupled*. This gives rise to familiar effects, as the shiny appearance of metals, and more exotic applications which involve some particular *excitations* of these coupled systems. One of these excitations is known as *surface plasmon polariton* (SPP) and it is usually observed at metal-dielectric interfaces. Another one is called *localized surface plasmon polariton* (LSPR), and is typically observed in colloidal dispersion of metal nanoparticles. As it will be clearer later, these systems are not the only ones that can sustain plasmonic excitations. Applications of these phenomena include subwavelength light confinement in the form of *plasmonic waveguides*, local amplification of electric fields (employed in *Surface Enhanced Raman Spectroscopy*) and light harvesting in the framework of thin films solar cells. Moreover, a new type of metamaterials, known as *hyperbolic metamaterials* has in the discipline of plasmonics its foundation.

Metals such as gold and silver are commonly used in plasmonics because of their small ohmic losses. However, such materials have high intraband losses in the NIR range and high interband losses in the visible range, especially at small wavelengths (actually, their plasmonic resonance and range of application is usually in the visible!). Moreover, metals suffer severe dewetting effects when deposited on non-dedicated substrates, and this sets a lower limit to the thickness of metallic films. These reasons spurred research towards materials which could be employed in this field as an alternative to metals. A very promising material class which could be suitable for this is that of transparent conductive oxides (TCOs), which nowadays are employed in flat panel displays and thin film solar cells. They combine optical transparency with electrical conductivity. Due to their carrier density, which is lower than in metals, TCOs have a plasma frequency in the NIR range. Even though TCOs are a quite mature technology, research is done on new materials and new applications in the field of plasmonics. To this respect, the most studied ones are AZO (aluminum zinc oxide), GZO (gallium zinc oxide) and ITO (indium tin oxide), which is also the most used commercial TCO. More niche example include niobium-doped titanium oxide ad tantalum doped titanium oxide, whose properties are discussed in this thesis work. This material was deposited in the form of compact and porous thin films via the pulsed laser deposition method, with the goal of expanding the knowledge acquired from previous works on the topic. In past works, depositions conditions were optimized with respect to electrical properties. Compact films with low resistivity and high carrier density were synthesized. The idea of raising the deposition pressure in order to make nanoporous films was explored.

In this thesis work, these concepts are further investigated, with a focus on the growth of nanoporous thin films and on the synthesis of dielectric-TCO interfaces. These topics, and other collateral ones are discussed throughout five chapters, as reported below.

- **Chapter 1** provides a general introduction on transparent conductive oxides and their main applications. Their behavior in the framework of solid state physics is briefly discussed, and the possibility of using them in the field of plasmonics is outlined. A pan on major TCO types is made, with a focus on those based on titanium oxide. The behavior of this material is then discussed, both in its pure and doped form. In particular, the results achieved in this laboratory are summarized, and compared to other pieces of literature. The objectives of this thesis are finally outlined.

- **Chapter 2** describes the experimental setup used during this work, including both synthesis and characterization of films.

- **Chapter 3** discusses the synthesis of porous nanofilms and hierarchical nanoparticle assemblies. While in previous works tantalum doped titanium oxide was deposited in a pure oxygen atmosphere, the idea of depositing in a mixed argon-oxygen atmosphere is here explored. Since porous structure synthesis requires a high pressure, but at the same time an excessive oxygen content is deleterious to the electrical properties (specifically, it greatly reduces the doping efficiency), depositing in a mixed atmosphere allows to increase the *overall* pressure while keeping the oxygen partial pressure low. The efficiency of this strategy, jointly to the effects of different thermal treatments, is investigated here. Raman, morphological and optical characterization is reported.

- **Chapter 4** discusses the synthesis of interfaces between materials with different conductivity, and thus different dielectric function. This basic scheme is at the base of SPPs. Two bilayered configurations were made, by suitably combining tantalum doped titania, substoichiometric titania and stoichiometric titania. Afterwards, stoichiometric titania was employed as a seed layer to attempt the deposition of ultrathin doped titania layer, down to the thickness of 5 mm. Raman, morphological and electrical characterization is reported.

- **Chapter 5** merges the techniques described in the previous two chapters. Bilayered and multilayered films are made, with each layer being deposited at different pressures. Raman, morphological, electrical and optical characterization is reported.

A short summary of the thesis work follows, highlighting the main achievements reached and the work that still need to be done. Additionally, a brief theoretical appendix is included, where a qualitative discussion about the concepts of *plasma* and *plasmonic excitations* is presented.

During this work, I personally performed the synthesis of samples by pulsed laser deposition and vacuum annealing, as well as their subsequent characterization by Raman spectroscopy, four point probe method, scanning electron microscopy and UV-vis-NIR spectrophotometry. All data elaboration was performed by myself.

Chapter 1

Transparent conductive oxides

As their name suggests, transparent conductive oxides (TCOs) are a special class of materials which combine transparency in the visible range with electrical conductivity. While the first attempts at producing such materials date back to the early 1900s, TCOs experienced a renewed interest in the last decades, due to the emergence of new photovoltaic technologies and the capillary diffusion of flat-screen monitors. In both cases, it is necessary to have electrical contacts that won't absorb light within a certain range of the spectrum [1].

As an example, thin film and dye sensitized solar cells cannot bear copper contacts, as traditional silicon cells do, but rely instead on a TCO film located between the active layer and the glass cladding, as shown in figure 1.1. While TCOs can't match copper in terms of electrical conductivity, cell architecture partly offsets this issue, since an entire layer of material, rather than narrow contacts, covers the cell [2].

TCOs are usually highly doped metal oxides. Dopant concentration is much higher if compared to those of microelectronic or photovoltaic applications. Sometimes we don't even speak of doped oxides, but of ternary compounds: it is the case of indium tin oxide, (ITO) which nowadays dominates the thin film photovoltaic and flat-panel display markets.

Indium's price and an expected growth in TCO demand [3] have stimulated the research of cheaper alternatives to ITO, mostly in the form of doped binary oxides, such as fluorine-doped tin oxide (FTO) and aluminum-doped zinc oxide (AZO). In addition to that, novel applications of these material – one example, plasmonics – are also being investigated nowadays.

1.1 Working priciples of TCOs

TCOs are both transparent and conductive; these properties are usually not seen together in the same material, for reasons related to the physical principles behind light absorption and charge transport. In fact, the performance of these materials is always the result of a compromise between conflicting goals.

An essential requirement for such materials is to have a bandgap greater than approximately 3 eV, the upper limit of the visible spectrum. This is a necessary but by no means sufficient condition for transparency. Many metal oxides fulfill this requirement. However, due to their structure and composition they don't have enough free carriers

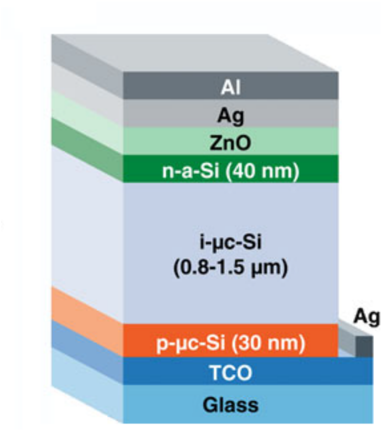

Figure 1.1: The TCO layer in a thin film solar cell constitutes the front contact, while the back contact can be made of a non transparent material. Taken from [1].

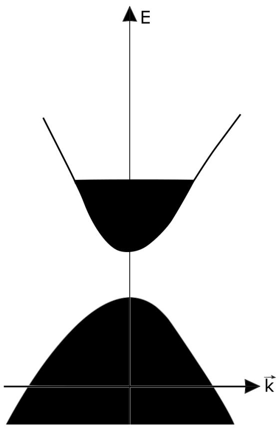

Figure 1.2: Sketch of the band structure of a TCO.

to conduct electricity. This problem is overcome by heavy doping, at 5% or more [1]. While depending on doping efficiency, this usually corresponds to a carrier density of the order of 10^{21} cm^{-3}.

1.1.1 Effects of doping

Such a high doping level (we speak of *degenerate* doping when $n > 10^{18}$ cm^{-3}) pushes the Fermi energy well above the bottom of the conduction band, as shown in figure 1.2, allowing free carriers conduction. However, the free carrier density cannot be too high, otherwise the plasma frequency (see Appendix) will fall into the visible range, leading to a severe increase in reflection due to the collective modes of electrons in the conduction band known as *plasma oscillations* [4]. This creates an inescapable tradeoff between electrical conductivity and long wavelength transparency. The mere *presence* of too many free carriers hinders visible transparency.

Most TCOs are n-type, even if some research on p-type ones has been made [5]. Technically speaking, a distinction should be also made between intrinsic and extrinsic

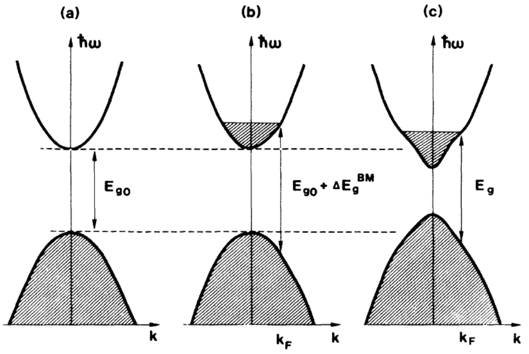

Figure 1.3: The bandgap of an oxide (a) experiences a Moss Burstein shift when dopants are introduced (b). At very high doping levels (c) this effect is reduced by band distortion. Taken from [8]

TCOs. Intrinsic conduction is achieved by means of oxygen vacancies or metal ion interstitials. It can be promoted by exposing the material to a reducing atmosphere. However, practical applications of TCOs typically involve extrinsic doping, due to the far superior achievable conductivity. This having been said, it should be pointed out that in some cases (as it will be discussed in this work) a perfect oxide stoichiometry actually hinders the effect of the dopant: there is an interplay between intrinsic and extrinsic doping mechanisms.

1.1.2 Optical behavior

Two main changes in material properties are promoted by the large carrier density. The first is called the Moss-Burstein effect [6]. Due to the high doping level, the conduction band is partially full, and the Fermi level lies above its bottom. This means that optical transitions from the top of the valence band to the bottom of the conduction band are not allowed, due to the absence of empty states. For example, in the case of a direct gap, allowed transitions are those from $\mathbf{k} \neq 0$ states in the valence band to corresponding empty states in the conduction band. This causes an increase of the effective bandgap, as shown in figure 1.3. It should be noted that this is not detrimental to the material's transparency, and it is not a constraint to dopant concentration. While a thorough discussion of the physics of this effect goes beyond the scope of this work, it is should be known that the magnitude of the bandgap shift can be related to the material carrier density. As an example,

$$\Delta E \sim n^{2/3}$$

if a free electron model is considered [7]. The second effect caused by the dopant is the presence of a plasma frequency

$$\omega_P = \left(\frac{ne^2}{\varepsilon m^*}\right)^{1/2}$$

in the near-infrared region (more details on the Appendix). Generally speaking, materials will exhibit changes in transmittance and reflectance in the region *around* the plasma wavelength

$$\lambda_P = \frac{2\pi c}{\omega_P}$$

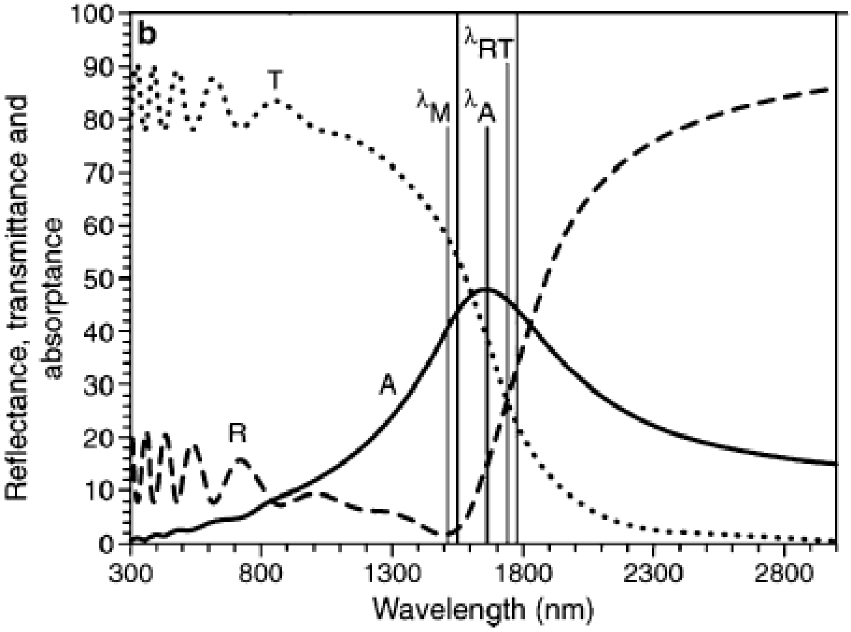

Figure 1.4: The T-A-R curves for a modeled TCO thin film. The plasma frequency of a conductive material is a good proxy for determining its optical properties (reflectance, transmittance, and absorbance). The reported spectrum was modeled assuming $n = 5 \times 10^{20}$, $m^* = 0.4 \times m_e$, $\varepsilon_\infty = 4$, $\mu = 50\ \mathrm{cm^2V^{-1}s^{-1}}$ and film thickness 500 nm. Adapted from [1].

As shown in figure 1.4, these transitions are not abrupt; in fact there is a specific wavelength at which $T = R$, called λ_{TR}. However, its value slightly differs from that of the plasma wavelength. Moreover, the decrease in transmittance is not exactly matched by an increase in reflectance. There is an *absorption* peak centered in λ_A, which differs both from λ_P and λ_{TR}. Unlike λ_P, the absorption peak and the T-R intersection frequencies don't have a simple analytical expression. Also, their positions change according to the examined material. However, since they all fall in good proximity, it is possible to have an estimate of the plasma frequency by performing optical characterization experiments.

1.1.3 Electrical behavior

Charge transport in TCOs is not as effective as in metals, but it can be similarly modeled, according to a semiclassical Drude theory [1]. Compared to a metal, a TCO has a lower carrier density and possibly different scattering mechanisms active for electrons, which hinder carrier mobility. The four main scattering mechanisms are:

1. electron-phonon scattering
2. impurity scattering
3. grain-boundary scattering
4. surface scattering

The first one is always present, in all materials at $T \neq 0$ K, while the last one is a typical feature of thin films (see section 1.1.4).

The contribution of ionized impurities scattering to the overall reduction in mobility is a typical trait of doped materials in general. While a perfectly pure metal can conduct electricity, a semiconductor (or oxide) *relies* on impurities in order to conduct. In TCOs this scattering type is even more relevant than in semiconductors, due to the higher tenure of dopants. It should also be noted that other defects such as vacancies, even though technically not impurities, can contribute to this type of scattering.

In the case of polycrystalline TCOs, grain boundary scattering could become relevant as well. Energetically speaking, grain boundaries induce electronic states within the bandgap of the material that can act as free-carrier traps. As such states become occupied, an electrical charge accumulates around the grain boundary, and an electrostatic potential barrier builds up at the boundary site. The barrier would thus generate the scattering. Contrasting opinions are found in literature regarding the relevance of grain-boundary scattering in TCOs. Some give great importance to this kind of scattering [9], while other consider the higher conductivity of monocrystalline TCOs to be a consequence of more refined synthesis techniques which inevitably create a less defectuous material [7].

What is certain is that ion-impurity scattering becomes the dominant mechanism at carrier densities higher than 5×10^{21} cm^{-3} [10]. It is easy to understand that an excessive doping level leads to a reduction in conductivity, because of the increased scattering frequency by ionized impurities.

The overall scattering rate can be calculated by Mathiessen's rule [11] if the relaxation times for each event are known:

$$\frac{1}{\tau_{tot}} = \frac{1}{\tau_{ph}} + \frac{1}{\tau_{imp}} + \frac{1}{\tau_{GB}} + \frac{1}{\tau_{surf}}$$

A typical TCO has a mobility of about $1 \sim 10$ cm^{2}V$^{-1}s^{-1}$, a resistivity of the order of $10^{-4} \sim 10^{-3}$ Ωcm and a carrier density of 10^{22} cm^{-3}. In the case of conventional TCOs, the carrier density is generally a function of the dopant concentration and doping efficiency, while the mobility (and thus the conductivity) depend on the aforementioned crystal and film properties: purity, grain size, and thickness.

1.1.4 Effects of thickness

For most applications, TCOs are manufactured in the form of thin films. For this reason it is crucial to understand how the electrical properties depend on the film thickness, and thus how thin films possibly differ from the bulk material. A thorough study of thickness-effects in TCO thin films was made by D.C. Look [12] [13].

The model quantifies the thickness-dependence of carrier mobility and sheet carrier density in terms of two phenomenological quantities, δd and d^*, where δd is the thickness of a "dead layer" at the interface, and d^* is a parameter that can be seen as the thickness needed to get a mobility of about a half of that achieved in a very thick layer (see figure 1.5.a). The reason for the presence of a dead layer (of the order of some nanometers) is a possible discrepancy between the metallurgical thickness and the fraction of it that is actually active for conduction. This difference could be due to unsuccessful doping or interface phase segregation. In this model, the sheet carrier density is given by

$$n_s(d) = n_\infty(d - \delta d)$$

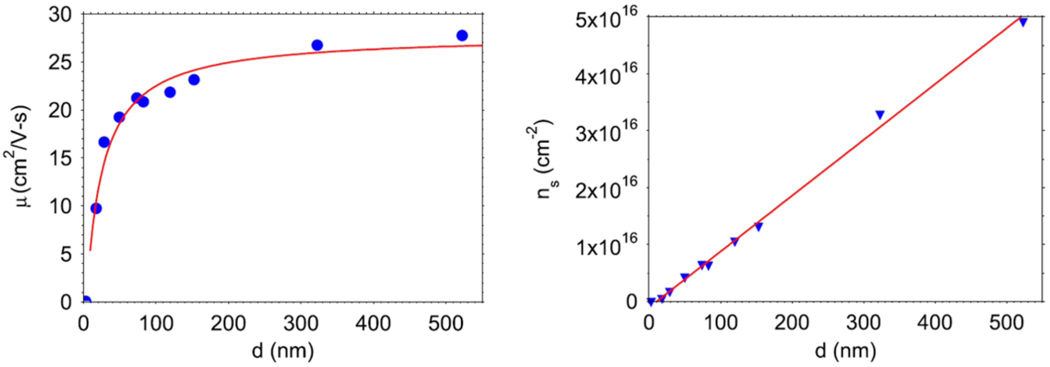

Figure 1.5: Left: carrier mobility as a function of film thickness. Right: sheet carrier density as a function of the film thickness. From [13].

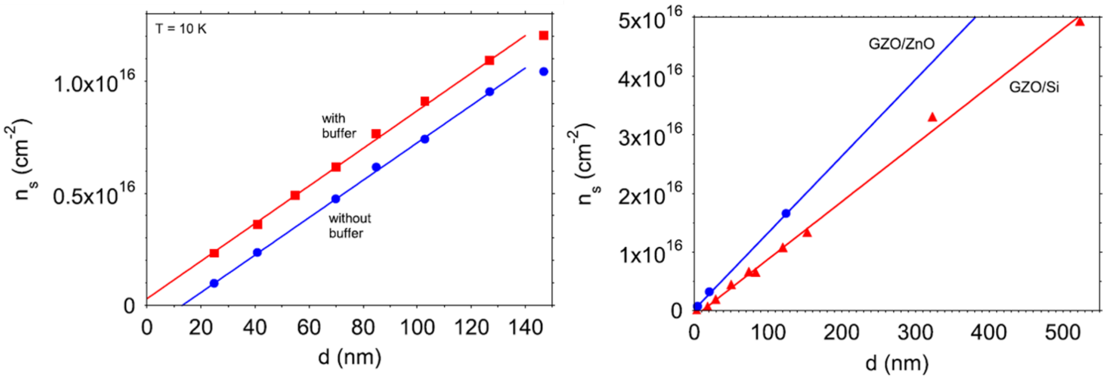

Figure 1.6: Sheet carrier density as a function of film thickness. On the left the effect of a buffer between unmatching lattices is shown On the right, a comparison is made between a lattice matched interface and an unmatched lattice one. From [13].

while the carrier mobility is

$$\mu(d) = \frac{\mu_\infty}{1+\frac{d^*}{(d-\delta d)}}$$

where n_∞ is the predicted bulk carrier concentration, and μ_∞ is the predicted bulk mobility.

In the specific case studied by D.C. Look (that is, AZO and GZO films) layers thicker than 600 nm are assumed to behave as bulk. This is a somewhat arbitrary value, and depends on the analyzed material. In bulk-like films, phonon scattering and impurity scattering dominate, while in thinner films surface-effects become more and more relevant. The main observation was that the sheet carrier density follows a linear trend if plotted against the film's thickness, as shown in figure 1.5.b, which means the bulk carrier density (the slope) does not depend on thickness, as long as $d > \delta d$. Conversely, carrier mobility depends on thickness even for $d > \delta d$, until it approaches the bulk value. It is possible to estimate the magnitude of the dead layer by taking the x-intercept of the sheet density linear trend.

The electrical behavior of film deposited on buffered substrates or lattice matching substrates was also covered. In the case of buffered substrates, it was found that the while the sheet carrier density increased, the bulk density remained constant (figure 1.6.a). The increase in sheet density was interpreted as a negative dead layer resulting in free electrons *spilling* into the buffer. Conversely, films deposited on matching substrates showed an increased bulk carrier density, associated to the better crystal quality (figure 1.6.b).

1.2 TCOs for plasmonic applications

Noble metals, usually gold or silver, are employed in traditional plasmonic devices, due to their small ohmic losses and easy tunability [14]. However, at optical frequencies, losses due to interband transitions arise [15]. These are responsible for the distinctive colors of noble metals. Even at the wavelengths at which interband transition are not an issue, intraband transitions and scattering losses are inevitably present. In order to overcome this issue, interest in TCO-based plasmonic materials arose in the last decade. The main difference between metals and TCOs with respect to plasmonic properties lies in the order of magnitude of the plasma wavelength. While in metals it falls into into the ultraviolet, in TCOs it is usually in the near or mid infrared range. Another difference between these two material classes is in the way the plasmonic response is usually tuned: in the case of metals, by acting on the size (nanoparticle diameter, film thickness), in the case of TCOs by varying the doping level. This does not mean that the plasmonic response of TCOs is shape and size independent: they rather have an additional degree of freedom (which metals lack – it is not possible to change the bulk carrier density of a metal). The fact that – due to their carrier density – TCOs have a frequency in the infrared makes them ideal for applications at telecom wavelengths (i.e. $1260 \sim 1625$ nm) such as waveguides and even logic gates. To this respect it must be said that oxides are much more prone to being deposited on common substrates like glass and silicon, compared to metals. This is true even at very low thicknesses (a few nm), while metals have a tendency to dewet. The possibility of depositing ultrathin films of plasmonic materials is crucial for the creation of optical computation devices. As an example, the scheme of a plasmon-equivalent MOSFET has been proposed [16][17]. This falls into the realm of *plasmonic active modulation*: the idea of tuning the plasmonic response of a material by imposing an electric field [18]. Finally, the plasmonic character of TCOs can be exploited in those devices which already employ this kind of material in the form of regular electrodes (e.g. DSSC photoanodes.).

1.2.1 AZO, ITO and GZO

The most studied TCOs as possible plasmonic materials are aluminum doped zinc oxide (AZO), gallium doped zinc oxide (GZO) and indium tin oxide (ITO). While ITO is also widely used (along with fluorine tin oxide) for flat-panels displays and solar applications, the study of AZO and GZO is more focused on novel and niche field of interest, such as plasmonics. All TCOs can be be manufactured by several deposition techniques. In particular, synthesis of ITO is probably the most mature one, technologically speaking, due to its large commercial use. It can be deposited by magnetron sputtering, pulsed laser deposition, chemical vapor deposition and even wet processes. When talking electrical conductivity alone, ITO is the best pick, having $\rho = 2.1 \times 10^{-4} \Omega$ cm in the case of magnetron sputtered [20] and post-annealed films (a commercially viable solution), and reaching $5.5 \times 10^{-5} \Omega$ cm in the case of epitaxially

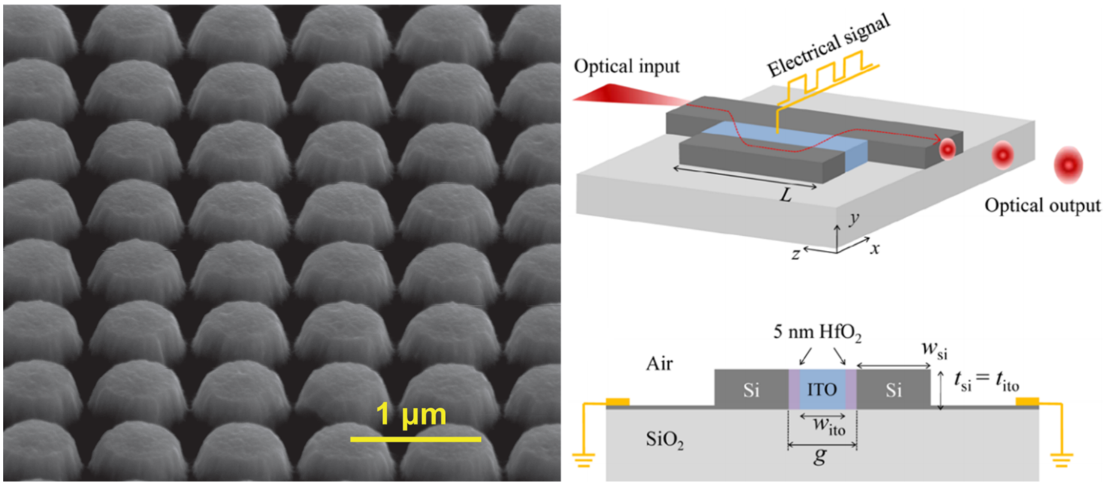

Figure 1.7: Left: scanning electron micrograph image of GZO nanodisks fabricated by e-beam lithography and lift-off processes [14]. Right: scheme of an ITO-based opto-electric modulator [19].

Table 1.1: Resistivity comparison for different TCOs. A difference exists between epitaxially grown and polycrystalline materials. Values are expressed in Ωcm.

TCO	Polycrystalline	Epitaxial
AZO	1.4×10^{-3}	6.5×10^{-4}
GZO	1.2×10^{-3}	2.0×10^{-4}
ITO	2.1×10^{-4}	5.5×10^{-5}

grown films [21]. For a comparison, the corresponding values for AZO and GZO, taken from different studies [22] [23] [24] [25], are reported in table 1.1. Table 1.2 reports instead a comparison of the carrier densities and plasma frequency and wavelength.

There are some reasons for which AZO and GZO are more promising in the field of plasmonics, though. One is that they suffer lower losses. Another one is that they are easier to pattern – compared to ITO – using photolithography and etching techniques. This would be an advantage in applications where nanosized features can determine the material's behavior [14]. As an example, a GZO nanodisk array obtained by etching is reported in figure 1.7.a. Similar structures are interesting when it comes to sustaining LSPRs (see Appendix) on TCOs, whereas the *traditional* tool for this application is generally seen in metal nanoparticles. Beside their physical properties, the great general advantage of TCOs over metals is the possibility of integrating them in already existing technologies and exploit the knowledge in microfabrication that we already have. Another

Table 1.2: Carrier density and plasma properties for different TCOs. From [26]

TCO	n (cm^{-3})	ω_P (rad/s)	λ_P (nm)
AZO	1.2×10^{21}	2.3×10^{15}	820
GZO	6.8×10^{20}	2.9×10^{15}	643
ITO	1.3×10^{21}	2.7×10^{15}	696

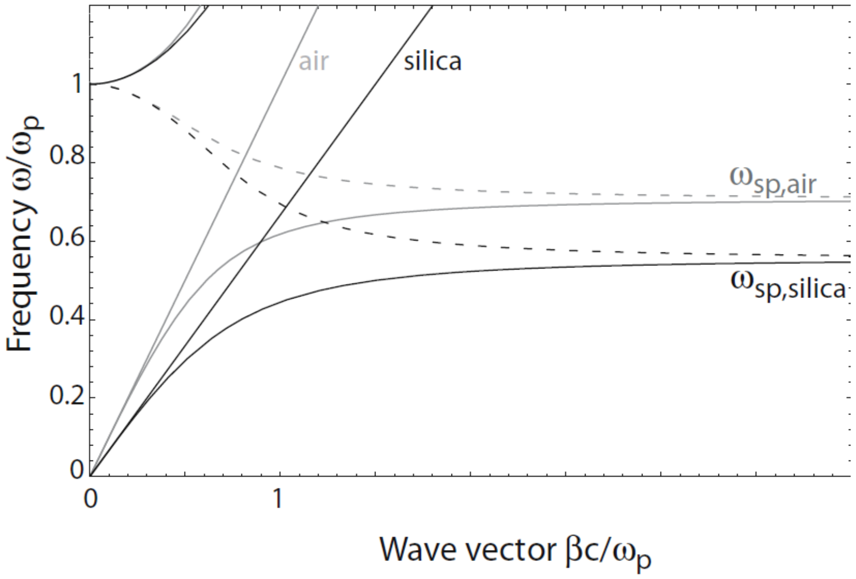

Figure 1.8: Surface plasmon polariton dispersion relations for a metal-air interface and for a metal-silica interface. Taken from [4].

example of plasmonic TCO device (in this case, ITO-based) is shown figure 1.7.b.

1.2.2 TCO-dielectric interfaces

One reason interfaces between TCOs and dielectrics are interesting is that dielectric materials can act as buffer layers between the actual substrate and conducting film. This should improve the crystal quality of the layer above, with benefits to the material's electrical properties. In some applications (think solar cells) the dielectric layer would actually behave as a resistive element: nevertheless, the effect would be outdone by the improved TCO conductivity [27].

A more sophisticated application of TCO-dielectric interfaces revolves around their ability to sustain plasmonic excitations known as *surface plasmon polaritons* or SPPs [28] [4] (see also Appendix). In principle, these modes can exist at various interface types, like metal-air (the dispersion relation is provided in figure 1.8) and metal-dielectric, provided that a some conditions on the permittivities are met. In a TCO-dielectric configuration, the TCO, being the conductive layer, would play the role of the metal [29]. SPPs propagate along the interface and are spatially confined in its near proximity. These plasmonic excitations are at the basis of *plasmonic waveguides* [4] and *hyperbolic metamaterials* [30]. Even though now most research about SPPs has been made on metal-dielectric interfaces, some works have been published about exploring the possibility of using TCO-dielectric interfaces instead [31]. The idea of using AZO for NIR waveguides has been proposed [32], however literature in this direction is not vast, with most schemes still relying on metals.

Concerning hyperbolic metamaterials, a study by Naik *et al.* showed the possibility of making one out of AZO/ZnO. A total of 16 alternating layers of pure zinc oxide and of Al:ZnO 2% wt. were deposited by pulsed laser deposition on silicon substrate. With the setup shown in figure 1.9, it was shown possible to achieve negative refraction in the NIR

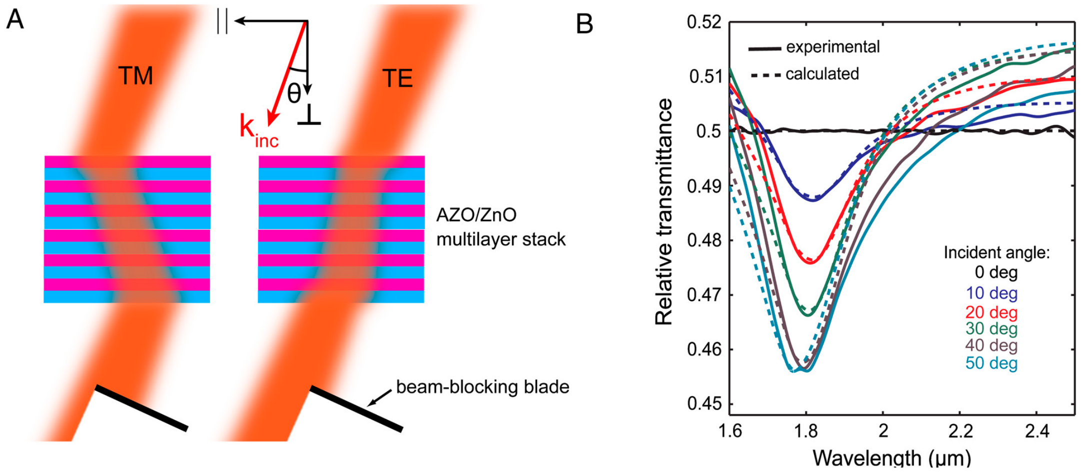

Figure 1.9: Observation of negative refraction: (a) Schematic showing the experimental setup for the measurement of negative refraction. (b) Relative transmittance for different angles of incidence from 0 to 50 degrees. The dip in the relative transmittance provides evidence of negative refraction in the case of TM polarization. Adapeted from [33] .

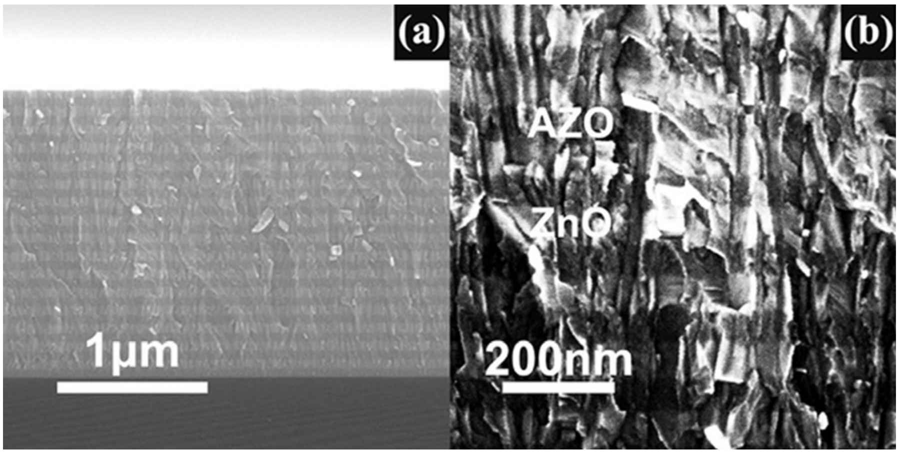

Figure 1.10: SEM images of an AZO/ZnO multilayer, at different zoom levels. Taken from [34].

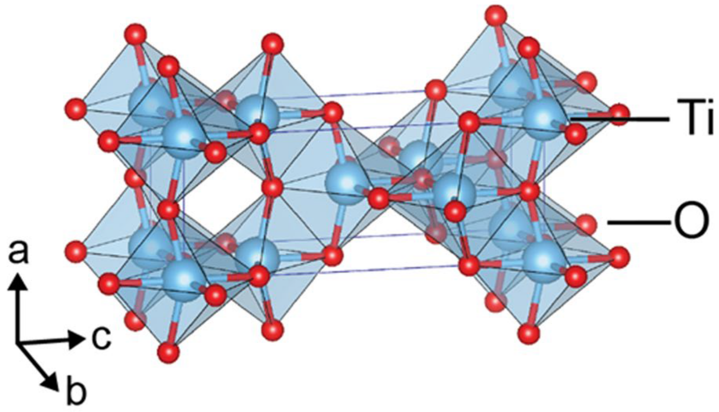

Figure 1.11: Crystal structure of anatase. Adapted from [35].

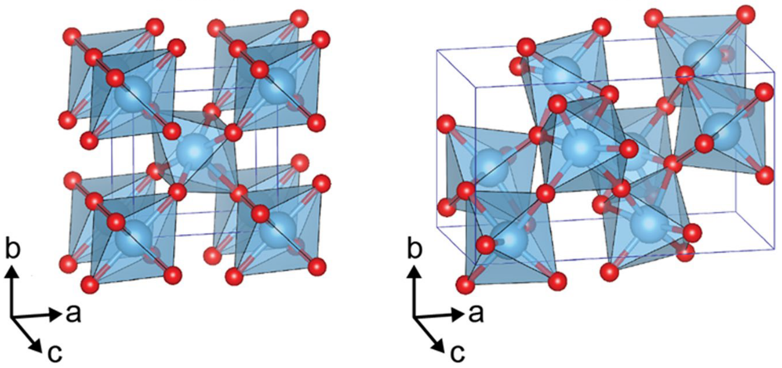

Figure 1.12: Crystal structure of rutile and brookite. Adapted from [35].

for TM modes. The metamaterial proved more performant (less losses, higher refraction) that its metal-dielectric counterparts [33]. Multilayered structures of AZO/ZnO were also tested as near-perfect-absorbers, (figure 1.10) as reported by Zhang *et al.*

While research on dielectric-TCO metamaterials exist, there is still a lot work to be done in this direction, especially concerning the shrinkage of the various material features (e.g. each layer's thickness in the case of multilayered nanofilms). Additionally, faster production techniques for these kinds of structures must be developed in order to open the way to large scale fabrication.

1.3 Titanium dioxide as a TCO

Titanium oxide is one of the most notorious functional materials. The majority of its consumption is due to its use as a white pigment, while specialty applications mainly exploit its behavior as a photocatalyst, after the groundbreaking studies made by Fujishima and Honda [36]. The three best-know allotropic forms of TiO_2 are the stable *rutile* and the metastable *anatase* and *brookite* (figures 1.11 and 1.12). They differ in crystal structure and bandgap [37], as shown in table 1.3.

All three have a bandgap above 3 eV and thus appear transparent in the visible range. The one form that is extensively employed in non-commodity applications is anatase, and

Table 1.3: Main allotropic forms of titanium oxide

Allotrope	Bandgap (eV)	Type
Rutile	3.05	direct
Anatase	3.20	indirect
Brookite	3.40	dubious

Table 1.4: Main peaks of the anatase Raman spectrum

Peak	Position (cm^{-1})
$E_g(1)$	144
$E_g(2)$	197
$B_{1g}(1)$	399
A_{1g}	513
$B_{1g}(2)$	519
$E_g(3)$	638

from now on in this work, unless specified, it will be implicit that doped and undoped titanium oxide is in the anatase form. The Raman spectrum of anatase exhibits six notable peaks. The main peak lies at 144 cm^{-1} in the case of undoped anatase. The six peaks are listed in table 1.4. The Raman spectrum of anatse, rutile and brookite are shown in figure 1.13.

Titanium oxide has too been proposed as an alternative plasmonic material in the framework of transparent conducting oxides. Even though a reasonable conductivity is only achieved by doping, it is useful to understand the conduction properties of undoped titania which arise from its intrinsic defects.

1.3.1 Defect chemistry of undoped titanium oxide

The electrical conductivity of pure titanium oxide is entirely dependent on its nonstoichiometry. Indeed, it is typical for titania to be n-type thanks to the contributions coming from oxygen vacancies and titanium interstitials (see figure 1.14). The actual composition of titanium oxide can be denoted more appropriately as TiO_{2-x} where x represents the oxygen deficiency. It is to be noted that stoichiometry deviations depend on the synthesis method and subsequent treatments, and can also lead to p-type conductivity. As a general rule, exposure to a reducing atmosphere will cause n-type conductivity, while exposure to an oxidizing environment will lead to p-type behavior [39]. Typical reducing environments include hydrogen gas and high vacuum levels; however, as previously stated, titania often exhibits a slight n-type conductivity even without intentional modifications. The presence of point defects also affects the optical properties: for example, an oxygen vacancy can act as a *color center*. When an electron is trapped into a vacancy, it can absorb light in the visible spectrum. This mechanism allows some materials with a bandgap greater than 3 eV to partially absorb in the visible and thus look colored to the human eye [38].

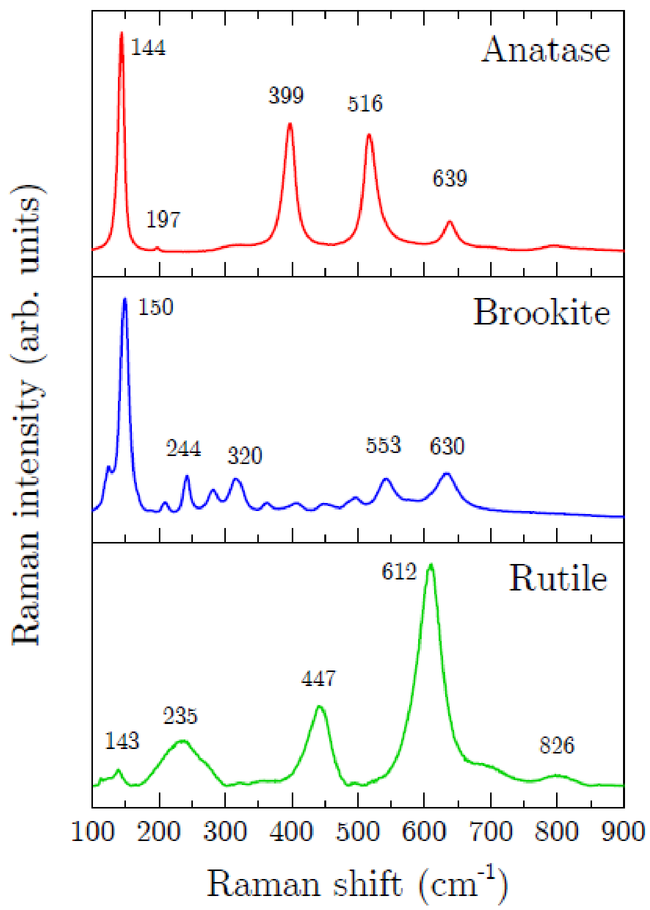

Figure 1.13: Raman spectra of anatase, rutile and brookite. Adapted from [38].

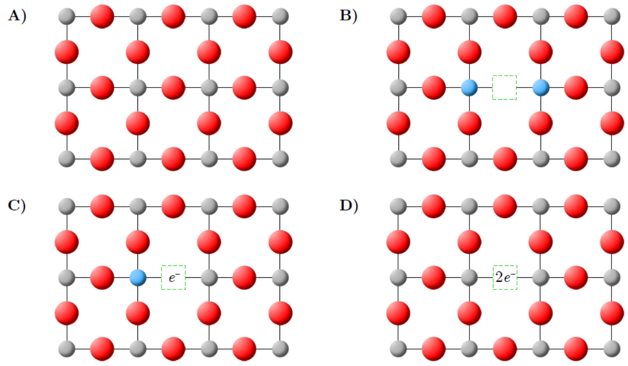

Figure 1.14: Different configurations of intrinsic defect in the lattice of TiO_2. Perfect stoichiometry (a) and oxygen vacancies with different ionization degrees (b,c,d). Taken from [38].

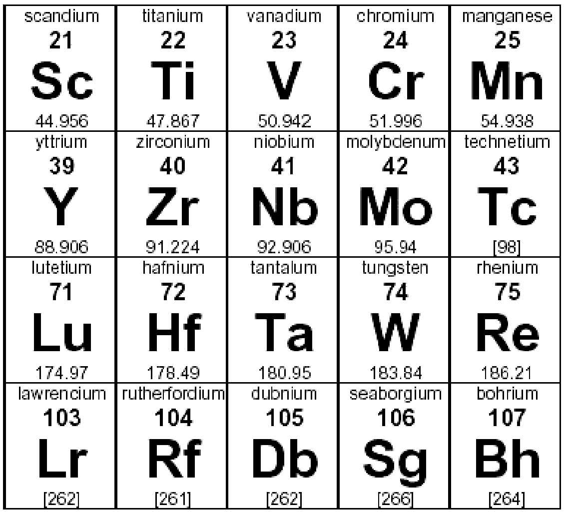

scandium 21 **Sc** 44.956	titanium 22 **Ti** 47.867	vanadium 23 **V** 50.942	chromium 24 **Cr** 51.996	manganese 25 **Mn** 54.938
yttrium 39 **Y** 88.906	zirconium 40 **Zr** 91.224	niobium 41 **Nb** 92.906	molybdenum 42 **Mo** 95.94	technetium 43 **Tc** [98]
lutetium 71 **Lu** 174.97	hafnium 72 **Hf** 178.49	tantalum 73 **Ta** 180.95	tungsten 74 **W** 183.84	rhenium 75 **Re** 186.21
lawrencium 103 **Lr** [262]	rutherfordium 104 **Rf** [261]	dubnium 105 **Db** [262]	seaborgium 106 **Sg** [266]	bohrium 107 **Bh** [264]

Figure 1.15: Substitutional doping is possible with atoms of the V group.

1.3.2 Doping of titanium oxide

The optical and electrical properties which derive from intrinsic defects can be also obtained (on a greater scale) by extrinsic doping. Doping of titanium oxide has been performed and studied with many different materials, mostly for photocatalytic purposes [40] [41] [42] [43] . Significant improvements to the *conductive* properties can instead be obtained by substituting the titanium atom (which belongs to the IV group) with elements belonging to the V group, as it can be seen by looking at the periodic table (figure 1.15).

The first important experimental results date back to 2005, and were obtained by the research group led by Hitosugi [44]. In this study, epitaxial niobium-doped anatase ($Ti_{1-x}Nb_xO_2$) was successfully deposited by pulsed laser deposition onto a $SrTiO_3(100)$ substrate. The substrate was optimized to promote epitaxial growth: as a matter of fact, the high level of order allowed for a very low resistivity of $2.3 \times 10^{-4} \Omega$ cm (figure 1.16), of the same order of magnitude as ITO ($1 \sim 3 \times 10^{-4} \Omega$ cm). Also, compared to ITO, the material showed better *metallic behavior* with respect to its $\rho(T)$ trend, and electron scattering was primarily due to phonons at room temperature. The optimal doping fraction for niobium doped titania was found at $x = 0.06$. This is the lowest conductivity obtained for doped TiO_2 so far, the one that most matches the performances of ITO. However, since epitaxial growth on $SrTiO_3(100)$ is not a realistically scalable process, the possibility of depositing $Ti_{1-x}Nb_xO_2$ on different substrates and/or with different techniques has been investigated.

For example, Hitosugi's group also explored the deposition of this material via PLD on glass substrates, followed by a reducing annealing [45]. The thermal treatment was necessary in order to promote crystallization into the anatase phase. As a matter of fact, since a glassy substrate cannot drive epitaxial growth, the films turned out to be amorphous. In the aforementioned work, the as-deposited films were annealed at 500° C in a H_2 atmosphere at the pressure of 1 atm, and turned into polycristalline anatase. A resistivity of $4.6 \times 10^{-4} \Omega$ cm was reported, corresponding to a doping fraction $x = 0.06$, as in the case of epitaxial films.

Shortly after Hitosugi's works, the synthesis of $Ti_{1-x}Nb_xO_2$ on $SrTiO_3$ by radiofrequency magnetron sputtering was studied by Gillispie *et al* [46]. The group managed to

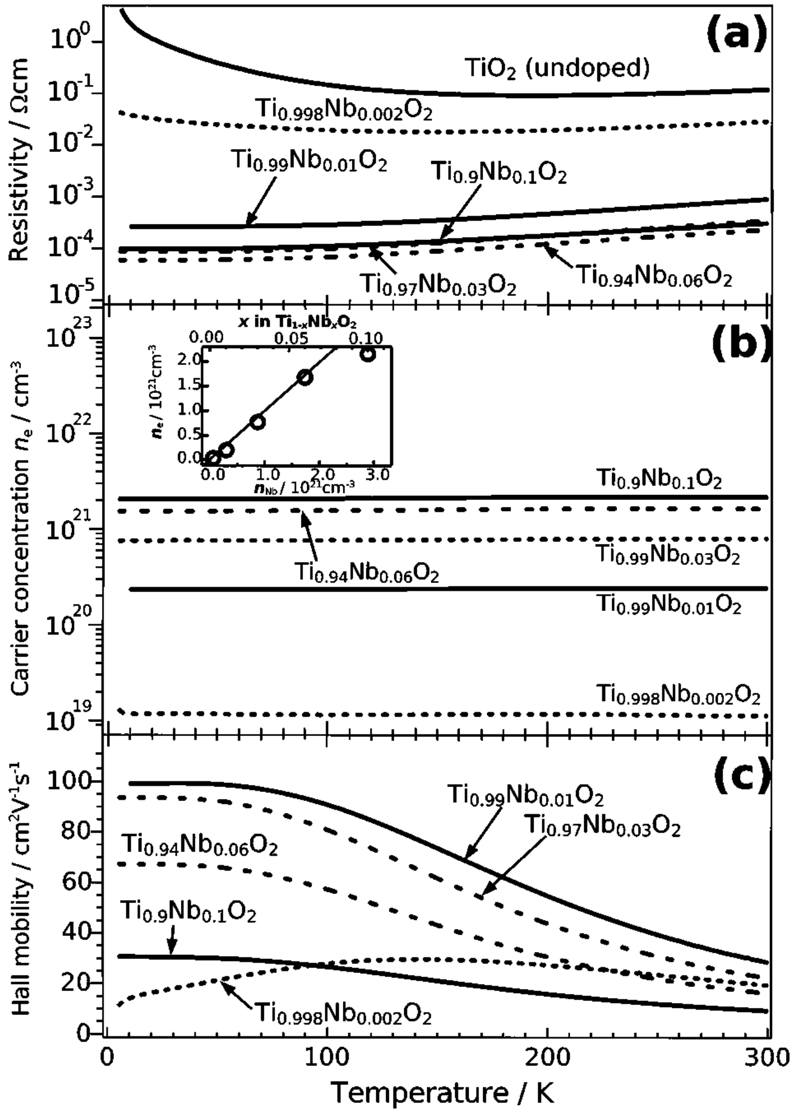

Figure 1.16: Electrical properties of TNO as a function of temperature. Taken from [44]

Table 1.5: Comparison of different synthesis routes for TNO. Doping concentration is at 6%

Author	Growth	Crystal	ρ (ωcm)	n (cm^{-3})
Furubayashi	PLD	epitaxial	2.3×10^{-4}	2.0×10^{21}
Hitosugi	PLD	polycrystalline	6.0×10^{-4}	1.5×10^{21}
Gillespie	RFMS	epitaxial	3.3×10^{-4}	2.4×10^{21}
Sato	DCMS	polycrystalline	1.3×10^{-3}	1.3×10^{21}

obtain epitaxial films with a dopant fraction $x = 0.15$ corresponding to a resistivity of $3.3 \times 10^{-4}\Omega$ cm. A plasma wavelength was also calculated at 1700 nm.

Direct current magnetron sputtering deposition of $Ti_{1-x}Nb_xO_2$ on quartz glass was studied bt Sato *et al* [47]. A dopant fraction of 0.06 led to a resistivity $\rho = 1.3 \times 10^{-3}\Omega$ cm, which is one order of magnitude greater of that of ITO. This shows the limits of using cheap substrates and rougher deposition techniques. The electrical properties of TNO, as reported in the cited works, are shown in table 1.5. While these works were more focused on the *conducting* behavior of TNO, it is instructive to have a look at the carrier density as well, since it determines the material plasma frequency.

A detailed DFT study has been made in 2016 by Matsubara *et al.* [48]. in which the behavior of different dopants in TiO_2 (namely V, Nb, Ta, Cr, Mo and W) is assessed and compared. The main results, which are consistent with experimental values, show that Nb, Ta, Mo and W behave as shallow donors while V and Cr behave as a deep donors. The key difference is that deep donor states greatly reduce the bandgap, allowing optical trasitions in the visible range. The effect is a loss in transparency.

1.3.3 Tantalum doped titanium oxide

Niobium is not the only possible V group dopant for titanium oxide. Since vanadium doping promotes the formation of deep donor states, which hinder transparency, only tantalum remains as an alternative. Tantalum doping of titania was actually studied by Hitosugi *et al.* alongside the more promising niobium [49]. Pulsed laser deposition of $Ti_{1-x}Ta_xO_2$ on $SrTiO_3(100)$ and $LaAlO_3(100)$ substrates was thoroughly investigated at various dopant concentrations. Doping fractions ranging from 0.01 to 0.15 were studied, and an optimum was found at $x = 0.05$ (see figure 1.17). This corresponds to $\rho = 2.5 \times 10^{-4}\Omega$ cm, which is worse than that obtained with niobium but still within the same order of magnitude. Conversely, the carrier density was higher, around 3.2×10^{21} cm^{-3}.

If conductivity alone is considered, then niobium proves better than tantalum as a dopant. However, in the light of possible plasmonic applications, tantalum has two advantages: a *higher dopant solubility* into the titania matrix and a *lower effective mass* for the donor electrons [50].

The key fact to keep in mind here is that plasmonic TCOs can have their plasma frequency tuned by changing the carrier density, even to the detriment of μ and σ. Indeed, while the optimum dopant concentration lies at $5 \sim 6\%$ depending on the material, *a much higher doping level may be used* in order to obtain a certain ω_p. In this framework, a higher solubility is a plus, because it leads to a greater doping efficiency, which helps in fine-tuning the carrier density. Instead, a lower effective mass for the donor electron is

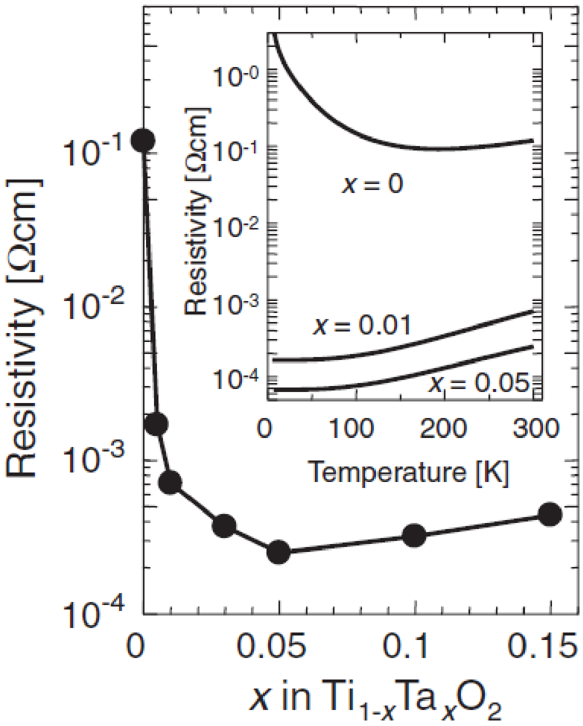

Figure 1.17: Electrical properties of TaTO as a function of dopant concentration. Taken from [49]

beneficial because it allows for better mobility even at high doping levels. In a way, it makes the TCOs *less susceptible* to changes in the carrier density.

A thorough study of tantalum doped titanium oxide (henceforth referred to as TaTO) was performed by Mazzolini [50] [51] [52] [53] in this laboratory. TaTO thin films were deposited by pulsed laser deposition on soda-lime glass and Si(100) substrates. As expected from Hitosugi's works, the films were amorphous and non-conductive. Polycrystallinity (see figure 1.18) was achieved by vacuum annealing at 550° C. Conversely, annealing in air resulted in non-conductive films. This means either that oxygen vacancies play an important (but not yet understood) role in the doping process or that oxygen manages to "kill" the donor states.

Three important achievements were reached by Mazzolini: the optimization of a synthesis process for polycrystalline TaTO, the estimate of a plausible value for its plasma frequency, and the observation of a trend regarding the material's carrier density and Raman spectra.

Thin films were deposited on the substrates by PLD in a pure oxygen background atmosphere, with a ns-puled laser. The frequency was kept at $\lambda = 266$ nm (Nd:YAG, fourth harmonic). After deposition, the amorphous films were vacuum annealed at 550° C to induce anatase crystallization. The effect of pressure during the deposition and its role in determining the electrical properties was investigated. A conductivity optimum was found at $P = 1.25$ Pa of pure O_2 (figure 1.19), corresponding to a resistivity of $5.0 \times 10^{-4}\Omega$ cm. 8×10^{20} For comparison, Hitosugi's group obtained $2.5 \times 10^{-4}\Omega$

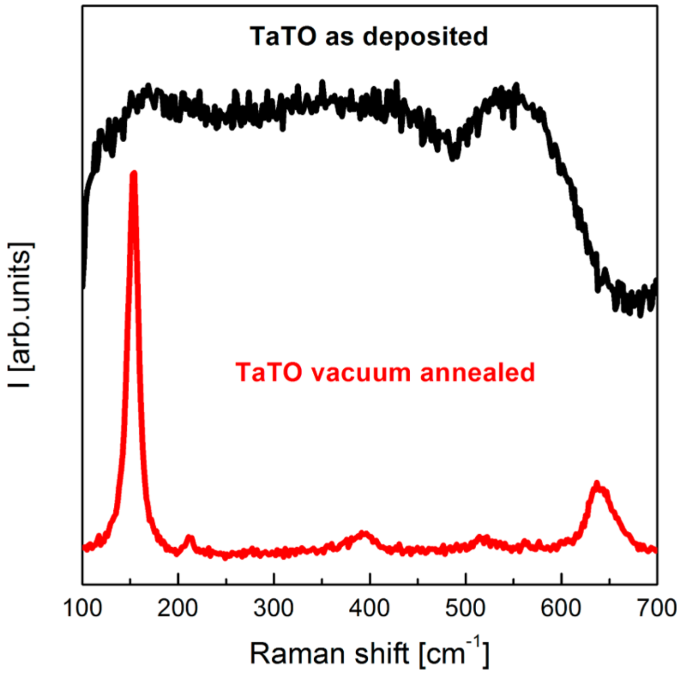

Figure 1.18: A post-anneling promotes crystallization into the anatase phase. Raman characterization is one of the easiest way to assess this phase change. From [51]

cm for monocrystalline TaTO and $4.6 \times 10^{-4}\Omega$ cm for polycrystalline TNO. The so optimized polycrystalline TaTO had $n = 8 \times 10^{20}$ cm^{-3}.

The plasma frequency of the deposited material was estimated by exploiting several known properties of TCOs and conductors in general. First, the material was characterized optically, and a Tauc plot was constructed in order to calculate the bandgap. The latter differs from that of undoped TiO_2 because of the Moss-Burstein effect (see section 1.1.2). If we plot the shift against $n^{2/3}$ where n is the carrier density, we obtain a straight line whose slope is proportional to the effective mass, which was estimated at $2.9 \times m_\circ$, where $m_\circ$ is the electron rest mass. This value can be used, with the empirically measured carrier density and the high frequency permittivity of TiO_2 of $5.9 \times \varepsilon_\circ$, to calculate the plasma frequency and wavelength. A value of $\lambda_P = 4160$ nm was obtained.

The third significant result concerns the Raman spectrum of anatase, and how it changes as a consequence of doping. An increase in carrier density causes a blueshift in the $E_{1g}(1)$ peak position. A monotonical and almost linear correlation between the peak-shift and the density of carriers was found, as shown in figure 1.20. The trend seems to hold regardless of all other parameters, including the dopant concentration and even dopant material.

Mazzolini's work was carried on by Ornago, whose work explored the synthesis of "advanced" TaTO films, experimenting different deposition conditions [54].

Initially, the synthesis of films thinner than 50 nm was investigated. Consistently with what reported in literature [13] the carrier density proved to be constant, while the mobility decreased with thickness, and conductivity followed accordingly (figure 1.21).

Afterwards, the behavior of TaTO at a higher doping level (10%) was studied. The carrier density was found to increase, quite consistently with the doping level, while the

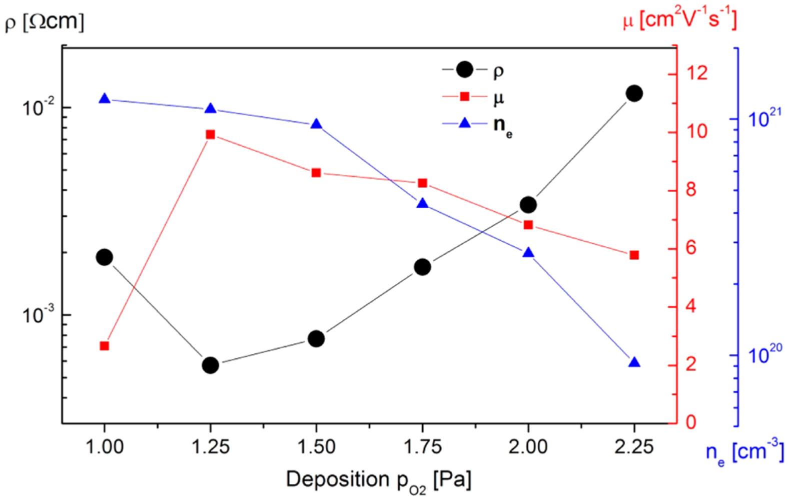

Figure 1.19: Electrical properties of TaTO as a function of the deposition pressure. Taken from [50].

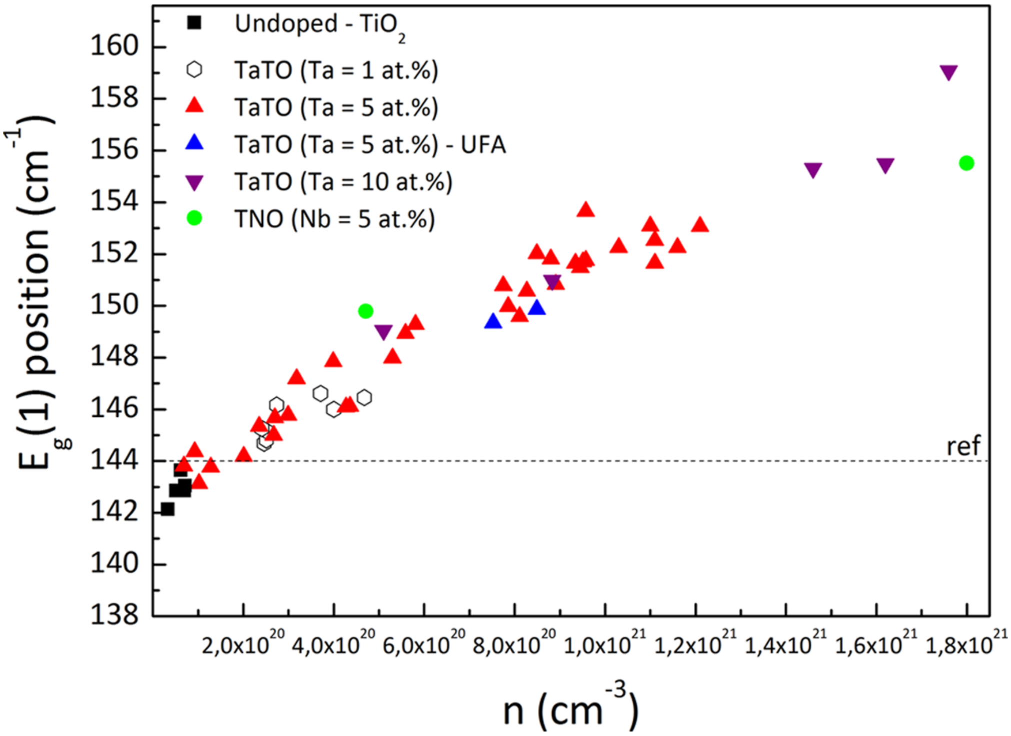

Figure 1.20: Raman shift of the main anatase peak plotted agaist the carrier density. From [50].

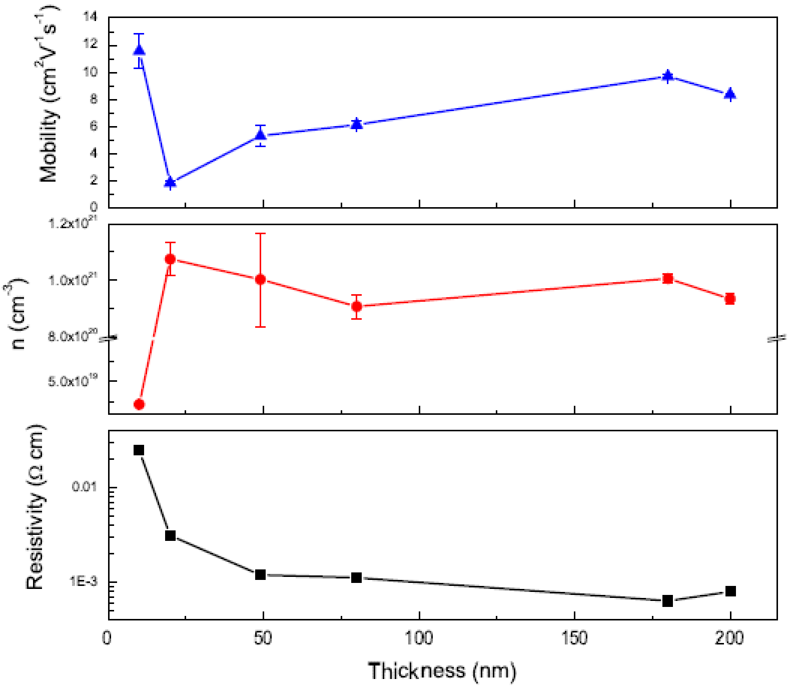

Figure 1.21: Electrical properties of TaTO as a function of thickness. From [54].

mobility experienced a significant decrease. This was likely due to the greater impurity scattering rate and to the bad crystallization caused by a higher tantalum content (figure 1.22). It is interesting to notice that thanks to the high solubility of tantalum in the TiO_2 lattice, a doubling in dopant content translated to a doubling in carrier density.

The role of an inert background gas in the deposition atmosphere was explored as well. An gas mixture was optimized for 4 Pa depositions in the form of $Ar : O_2 = 5 : 1$. Even though films deposited in this conditions did not outperform those deposited in pure oxygen at 1 Pa (both in terms of conductivity and carrier density) they suggested a feasible way to deposited porous TaTO with a higher carrier density that would be obtained by depositing in pure oxygen. The reason behind this is that an excessive oxygen content in the deposition atmosphere is detrimental to the substoichiometry of the final product, which has been shown to be necessary to the activation of the tantalum dopants.

The last topic covered by Ornago's work was the possibility of integrating gold nanoparticles in TaTO, by pulsed laser co-deposition of the two materials. The addition of gold resulted in a decrease in carrier density and increase in mobility, for an overall worsening of the electrical properties. A localized surface plasmon resonance (LSPR) peak was found in the region around $\lambda = 570$ nm of the optical absorption spectra.

It is important to mention that despite working with the same experimental tools, Ornago did not use the same deposition parameters as Mazzolini, and had to optimize the working conditions around a laser wavelength $\lambda = 532$ nm. A more detailed explanation is provided in chapter 2.

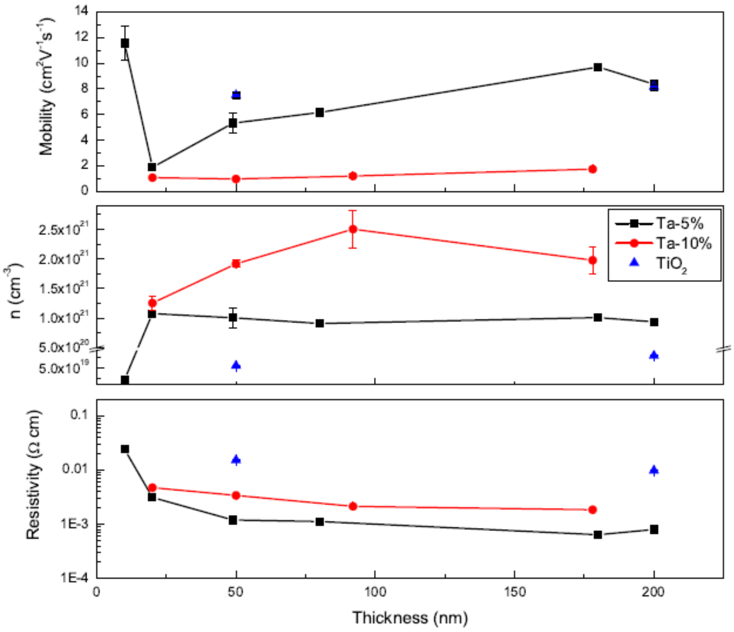

Figure 1.22: Comparison of doping levels. 10% of tantalum yields higher carrier density but higher resistivity and lower mobility. The material exhibits a high doping efficiency. From [54].

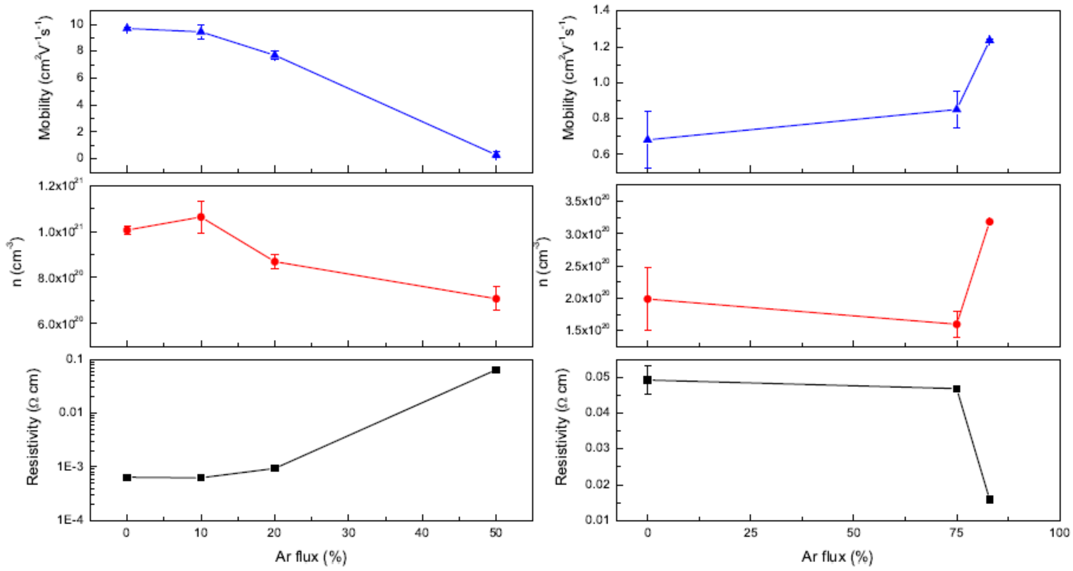

Figure 1.23: Comparison of the role of argon as a background gas in the deposiotion of TaTO at 1 Pa (left) and 4 Pa (right). Different mixture compositions were explored, a ratio of Ar : $O_2 = 5 : 1$ was found to yield the best electrical properties for 4 Pa depositions. From [54].

1.4 Objectives of this thesis work

This thesis work aims to explore the properties of tantalum-doped titanium oxide, in the light of future plasmonic applications. This means to analyze its optoelectrical behavior with a focus on the carrier density, how it is a function of the dopant concentration, and how it can be tuned by acting on the material's morphology. Thin films of TaTO were deposited by pulsed laser deposition (PLD), subjected to different thermal treatments and subsequently characterized via Raman spectroscopy, scanning electron microscopy (SEM), UV-vis-NIR spectrophotometry and four-point probe electrical analysis.

Since the tools at our disposal couldn't allow for a thorough characterization of the material's optical behavior at its plasma frequency, which is expected to be in the near infrared, a deep analysis of the material's morphology, electrical properties and crystallinity was performed. The variation of these physical properties as a function of thickness, deposition pressure and thermal treatments was investigated. Previous works managed to define optimal synthesis conditions for TaTO as far as electrical conductivity is concerned. This work aims to explore synthesis conditions not yet touched by previous dissertations. The main objectives of this thesis are two.

Synthesis of high-*n* nanoparticles It is well known that at increasing pressures, deposited films grow more and more porous, transitioning from a compact form to hierarchical nanoparticle assemblies. However, to increasing deposition pressures (see also section 2.1) is often associated a decrease in the carrier density due to excess of oxygen in the deposition chamber, which ends up hindering the much needed substoichiometry. Hence the idea to deposit in a mixed argon-oxygen atmosphere, in order to obtain nanostructures (increased pressure) but maintaining the oxygen partial pressure low. The role of argon gas in the deposition atmosphere will be investigated, at different overall pressure values. A comparison will be made between pure oxygen depositions and argon-oxygen depositions, to assess whether the lower oxygen content can promote a high carrier density. Still, this may not be the full picture. The type of thermal treatment that is performed on the films can have an influence as well on the electrical properties. After a preliminary study, the role of different thermal treatments on the optoelectronic properties of the film will be investigated.

Synthesis of dielectric-TCO interfaces Different bilayer configurations will be synthesized, all having in common the same basic structure: a TaTO layer deposited on top of a previously made titania layer. Two schemes will be explored: one where TaTO is deposited on substoichiometric (and thus conductive) titania and one where TaTO is deposited on insulating titania. The whole idea behind this kind of interfaces is that they should be able, just like metal-dielectric interfaces, to sustain surface plasmon polaritons. Making TCO-based interfaces of this kind is interesting for two reasons. One is that it would make it possible to stimulate plasmonic excitations in the NIR range. Second, oxides possess qualities which make them better than metals when it comes to fabricating ultrathin (say sub 10 nm) films; in particular, they boast a much greater percolation efficiency. In the light of this, the deposition of ultrathin TaTO films down to 5 nm will be attempted on top of stoichiometric titania, in the hope that the lattice matching substrate will allow for a better crystal quality than that observed on mismatching substrates.

Chapter 2

Experimental techniques

2.1 Pulsed laser deposition (PLD)

Pulsed laser deposition is a physical vapor deposition technique which allows to deposit thin films with a tight stoichiometric control. More precisely, it is based on the production of a *plasma plume* from a target material irradiated by intense laser pulses. The material ablated from the target travels and is eventually deposited on a substrate. While there exist techniques which are far more scalable at the industrial level, such as sputtering, PLD allows to finely tune a film composition by changing one or more of the many deposition parameters. Thus, it allows to explore the behavior of a material according to small variations in the synthesis conditions. In addition to that, PLD has been recognized as the best route to synthesize materials such as superconductors where accurate stoichiometry is paramount [55].

PLD systems can be classified according to the duration of a single laser pulse, which can be of the order of the nanosecond, picosecond or femtosecond. The main difference resides in the light-matter interaction and the timescale needed for energy transfer. In the case of ns-pulses the interaction tends to be a thermal process, with energy being transferred to phonons, while in the case of fs-pulses ablation it is mainly due to electronic absorption and excitation. Also, ns-pulses are long enough to interact with the newly formed plume, which becomes further ionized and energetic [56].

A typical PLD apparatus, as shown in figure 2.1, is composed by a laser source and a vacuum chamber containing the target material and the substrate. Laser pulses hit the target at an angle of around 45° with respect to the normal, while the susbstrate is located in front of the target. In order to ensure a uniform ablation of the target and a uniform deposition on the substrate, the latter experiences a rotational motion, while the former undergoes a *roto-translation*. Obviously a uniformly covered substrate is desiderable, to achieve consistent material properties, but also a uniformly ablated target is key to have a selfconsistent plasma plume, which leads in turn to an even deposition. The *uniform deposition area* is of the order of some square centimeters.

The process takes place inside a vacuum chamber, typically made of stainless steel. Vacuum is obtained by using a primary pump, which can reach pressures of the order of 1 Pa, followed by a turbomolecular pump, which can bring the pressure down to 10^{-4} Pa. The pressure is measured with different methods according to the pressure range.

After a vacuum has been made, one can choose to deposit the ablated material in

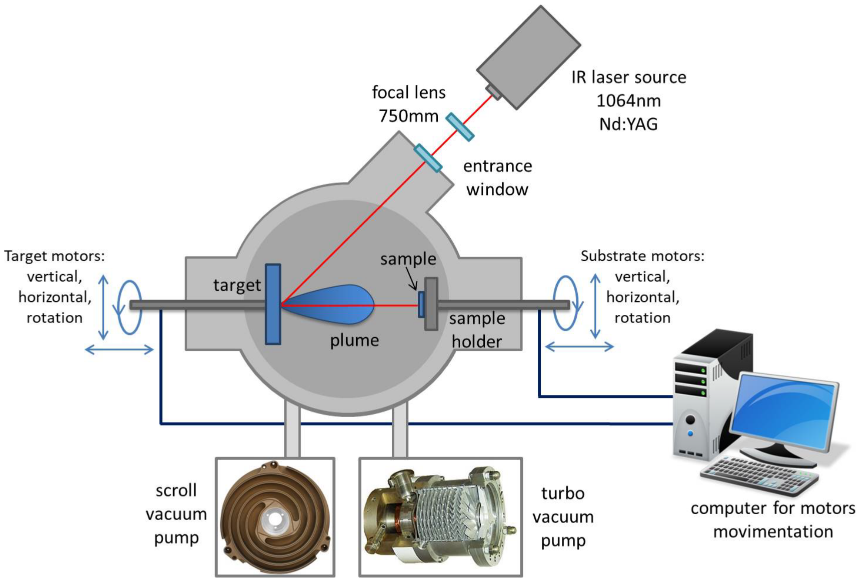

Figure 2.1: Scheme of a typical PLD system. Courtesy of Federica Romeo [57].

vacuum or in some background gas, which can be either inert or reactive (see figure 2.2): the choice of the deposition atmosphere is related to the material's properties and composition. The background gas can be added via a mass-flow control system, which allows to reach the desired pressure inside the chamber.

During the deposition, it is possible to control the film growth by using a quartz crystal microbalance (QCM). It is a vibrating quartz piece which must be placed close to the substrate, in a region deemed to undergo the same level of covering as the actual film. The increase in film thickness results in a change in the vibration frequency, as the crystal gets covered. This way film growth can be monitored in real time.

The main parameters that affect the properties of a deposited film are laser wavelength, pulse duration, pulse frequency, laser fluence, substrate temperature, target-substrate distance and chamber pressure.

The laser wavelength is inversely proportional to the energy transferred to the target *per incident photon*, therefore ablation with shorter wavelengths results in a greater ablated mass and in ablated species having greater kinetic energy.

As previously stated the duration of a single pulse (which lies in the nanosecond-femtosecond range) determines the type of interaction between the electromagnetic radiation and the target atoms. In the case of nanosecond pulses, the time scale is great enough for the excited electrons to thermalize. Thus a region greater than the irradiated one will be thermally affected. This usually results in a greater deposition rate in the case of nanosecond pulses, but higher incidence of droplets. Conversely, femtosecond pulses will create better films at a slower pace, but this can be solved by increasing the pulse frequency, which is the sheer number of pulses per unit time.

Fluence is the energy per unit area that is transferred to the target *by a single pulse* and beside determining the plume dynamics, it affects the quality of the formed film in many different ways. The effect of fluence greatly varies for different materials, but one general rule must be respected: a single pulse must be able to reach the so called *ablation threshold*, that is, it must provide enough energy to the target in order to ablate it.

The temperature of the deposition substrate affects the equilibrium properties of the

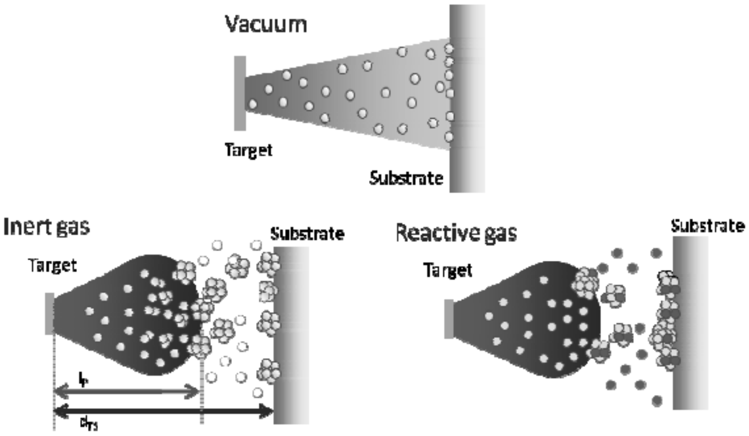

Figure 2.2: Three types of deposition atmosphere exist; vacuum deposition results in highly energetic impinging particles, while a background gas will slow them down. Reactive deposition is preferred for compounds, while vacuum and inert depostion is used for metals. Adapted from [56].

film, and thus its morphology. *In situ* heating leads to better crystallization and lower incidence of nonequilibrium structures such as columnar films.

The target-substrate distance affects the uniformity of the deposition. Because of the plume shape, the deposited material thickness profile will take a bell curve distribution. This effect is stronger when the target is close to the substrate. It can be solved by increasing the distance, but this leads to a greater "waste" of the impinging species and – in the presence of a background gas – a reduction of their kinetic energy. Thus, a compromise must be found. Additionally, strategies as the rotation of the substrates can be employed.

Last but not least, background pressure during deposition affects the film properties. The presence of a gas along the trajectory of ablated species reduces their kinetic energy, and this leads to less compact films (see figure 2.3). For very low background pressures films tend to exhibit residual stresses and possibly significant tribological properties. For very high pressures the ablated particles will arrive to the substrate with very low kinetic energy and may even have time to coalesce into clusters. This creates porous films with bad mechanical properties but high surface area. The *type* of background gas used in a deposition depends on the material that is being deposited. Oxygen is an obvious choice for oxides, while nitrides require nitrogen or an inert gas. It is to be noted that the choice of the ambient gas and the role it plays is also related to the target material. For example, a metal oxide can be deposited by ablating the oxide itself or its metal. While in the former case a reactive atmosphere can help stabilize the oxide stoichiometry, in the latter it entirely contributes to it.

The PLD apparatus used in this work employs a nanosecond-pulsed laser (Nd:YAG second harmonic, $\lambda = 532$ nm, repetition rate $f_p = 10$ Hz, pulse duration about 6 ns). The target-to-substrate distance was kept constant at $d_{ts} = 5$ cm, and laser fluence was set to 2.7 mJ/cm^{-2}. This value was optimized in the previous work carried out in this lab [54] for good electrical properties and low number of droplets. Background pressure was varied within 1 Pa and 15 Pa, and both pure oxygen and oxygen argon mixtures were used. Ta:TiO$_2$ thin films were grown on soda-lime glass and on Si(100) substrates by ablating

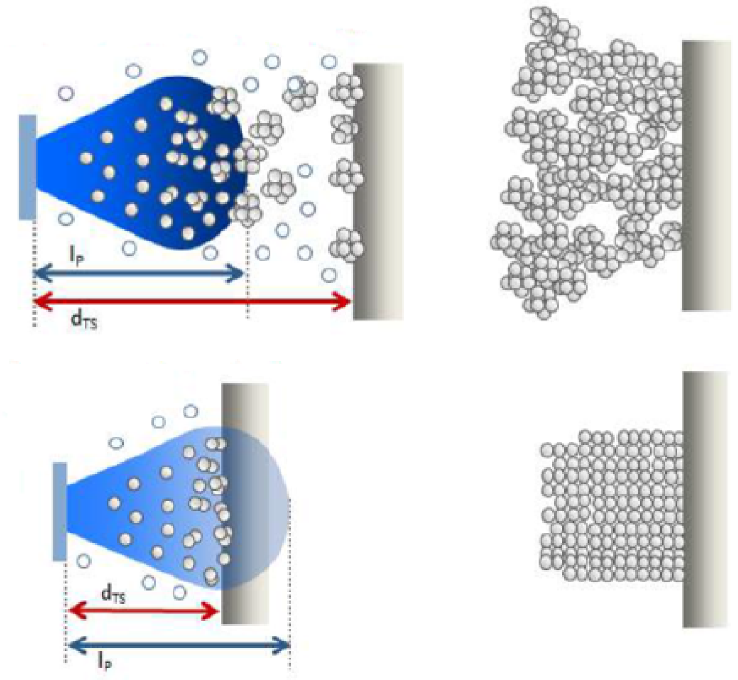

Figure 2.3: Effect of background pressure on film density. Low pressures yields compact films while high pressures promote the formation of columnar films and nanoparticles. Adapted from [58].

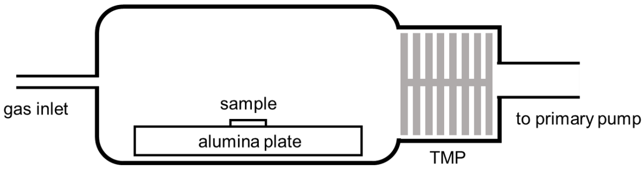

Figure 2.4: Scheme of the annealing system used in this work.

$Ta_2O_5 : TiO_2$ targets with molar ratio 0.025 : 0.975, corresponding to a 5% tantalum atomic content in the final film. The vacuum chamber is custom made and relies on an Agilent TriScroll 600 primary pump, plus a Pfeiffer Vacuum TMU 521 turbomolecular pump. The mass flow is controlled by a MKS Multi Gas Controller 647C.

2.2 Thermal treatments

Thermal treatments were performed with a custom built furnace, capable of carrying on annealing treatments in a controlled atmosphere. The apparatus comprises a vacuum chamber and related vacuum system, plus a heating system located inside the chamber, as shown in figure 2.4.

Samples are placed onto an alumina plate, in thermal contact with a Joule effect heating piece. It is possible to flux inert gases such as argon into the chamber, by manual mass flow control, thus changing the annealing atmosphere and making it more or less reducing. Also, by controlling the heating ramp, it is possible to perform heating procedures at different speeds.

The vacuum system relies on an Edwards rotary pump, which acts as a primary pump, connected in series to a Varian Turbo-V 250 MacroTorr turbomolecular pump. The heating system is run by a Tectra HC3500 Heater Controller, and the temperature data is collected with an Impac IGA 120 pyrometer.

Standard annealing treatment The most used thermal treatment, henceforth referred to as "standard annealing treatment" consists in a vacuum annealing at 550°C, reached with a smooth 10°C/min ramp. Dwell time is one hour. Cooling takes place at the same rate, but towards the end it slows down, since it is not mediated by any gas. The vacuum pressure can vary depending on the material, and it should be low enough to prevent material oxidation; in this thesis work it was always brought at 5×10^{-5} mbar. The heating profile is shown in picture 2.5.

Ultrafast annealing treatment (UFA) It can be seen as the fast paced version of the standard treatment. Once the vacuum pressure has been reached, the sample is rapidly brought to 550°C (the ramp requires approximately one minute). Dwell time was kept at 30 seconds, in this work but other values could be explored in principle. After the dwell, the sample is cooled by fluxating argon at 2 mbar. The heating profile is shown in picture 2.5.

Overpressured annealing treatment (OPA) Similarly to the standard annealing, it has a dwell time of one hour and slow paced heating and cooling ramps of 10°C/min. However, when the vacuum pressure is reached, a reducing mixture of Ar/H_2 (hydrogen: 5%) is fluxed until a pressure of 1050 mbar is reached. The heating profile is shown in figure 2.5. It should be noted that due to the presence of an ambient gas, the cooling curve is exactly linear.

Overpressured ultrafast annealing treatment (OPUFA) It is a combination of the two methods described above. After reaching the vacuum pressure, a reducing/inert mixture is fluxed at 1050 mbar, and a rapid annealing is performed. The ambient gas takes care of the cooling. The heating profile is shown in figure 2.5.

In addition to vacuum annealing treatments, air annealing treatments were performed in some cases, using a Lenton muffle furnace and reaching a temperature of 500°C with heating and cooling ramps of 4°C/min. Dwell time was kept at 2 hours.

2.3 Scanning electron microscopy

Scanning electron microscopy (SEM) is one of the most common microstructural characterization techniques. It allows to acquire images of any electrically conducting sample with a lateral resolution of the order of the nanometer, corresponding to the diffraction constraints imposed by the scanning electrons and some lens-related effects. The working principle of a typical SEM apparatus is shown in figure 2.6.

Samples are placed into a chamber and brought under high vacuum conditions (approximately 10^{-4} Pa). The high vacuum within the SEM column and specimen

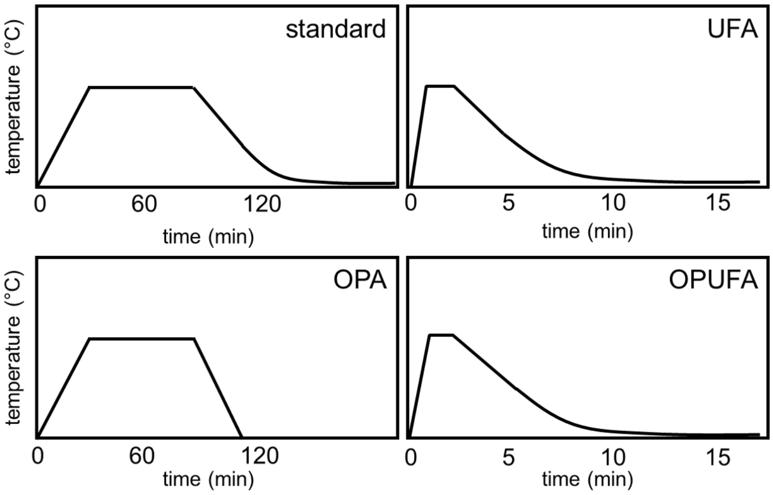

Figure 2.5: Thermal profiles of the four thermal treatments

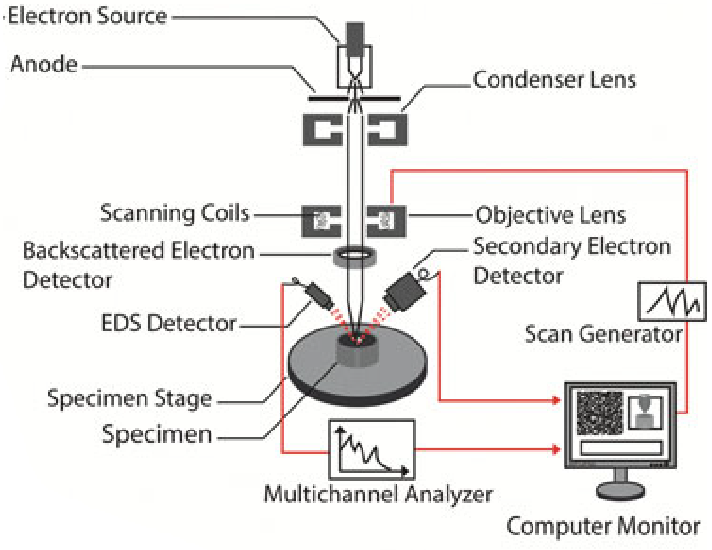

Figure 2.6: Working principle of a scanning electron microscope. Adapted from [59].

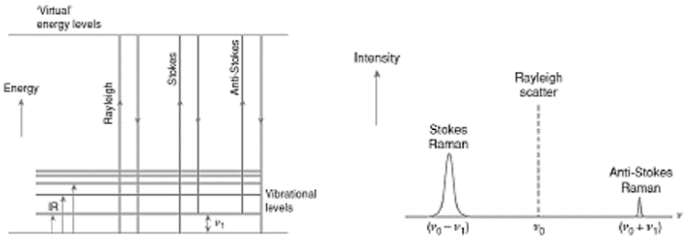

(a) (b)

Figure 2.7: Interaction of electromagnetic radiation with lattice vibrations can have three outcomes. Rayleigh scattering is elastic, while Raman events imply the creation or destruction of a phonon. [60].

chamber ensures a smooth travel of the electron beam without it getting scattered due to any residual gas molecule.

Electrons are emitted from an electron gun, either by field emission or thermionic effect, and accelerated by a voltage that can range from 200 V to 30 kV. An array of electromagnetic lenses collimates the electrons into a beam, which hits the sample. The beam is constantly guided by deflection coils and it scans the surface according to a raster pattern. Once the beam hits the material, a variety of signals are generated, but in this case *backscattered* and *secondary* electrons are exploited. The former are sensitive to crystal structure and orientation, and in particular allow to discern between compact and porous structures. The latter give a strong sense of depth and are used to understand a film's surface morphology [59].

In this thesis work, a Field Emission Zeiss SEM Supra 40 was employed to acquire images of the cross section of the the films. All SEM images presented in this work were obtained by imposing a bias of 5 kV. Both secondary and backscattered electrons were used, but the best results were obtained with the former type, and all the SEM images presented were obtained with secondary electrons.

2.4 Raman spectroscopy

Raman spectroscopy is based on inelastic scattering of light by a molecule or a crystal. This means that scattered photons have a different energy compared to incident ones. When a photon hits a molecule, the overall (photon + molecule) system is brought to a "virtual" state. Then, three things can happen (figure 2.7):
Rayleigh scattering: the molecule is in the same vibrational state as before the collision, meaning that inelastic scattering has occurred. Actually, it is the most frequent event.
Stokes transitions: the molecule is at a higher energy level, while the scattered radiation has a greater wavelength. The ΔE has been transferred from the photon to the molecule.
Antistokes transitions: the molecule is at a lower energy level: it has ceded energy to the photon, therefore the frequency of the scattered light is greater than that of the incident one. Since, in order to happen, this event needs some nonfundamental states to be occupied in the first place, it is the least frequent one [60].

Raman spectroscopy exploits Stokes transitions, whose signals are more intense than Antistokes ones. In the case of molecules, only those whose vibration modes produce a

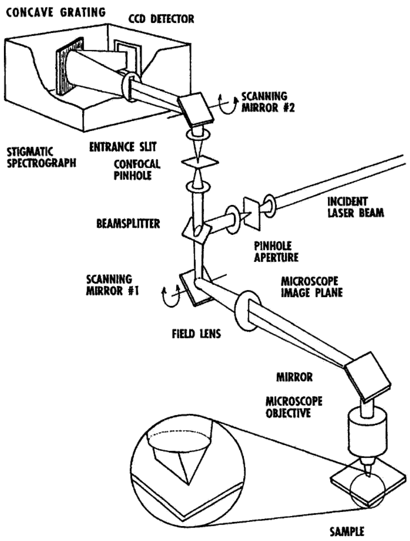

Figure 2.8: A typical Raman apparatus. Taken from [60].

change in the molecule's polarizability will be Raman-active.

The entirety of this work, however, deals with crystalline (and amorphous!) solids rather than molecules. Crystal theory must be taken into account. If an incident laser beam with wavevector $\mathbf{k}_i$ and angular frequency ω_i hits a surface, most of it will undergo Rayleigh scattering, but a fraction of the photons will interact with the lattice creating or destroying phonons having quasimomentum $\mathbf{q}$ and thus diffuse inelastically, with a wavevector $\mathbf{k}_d$ and frequency ω_d. Conservation of energy and quasimomentum implies

$$\mathbf{k}_i = \mathbf{k}_d + \mathbf{q}$$

$$\omega_i = \omega_d \pm \omega_q$$

Since the energy of both the incident and scattered photon is at least one order of magnitude greater than $\hbar\omega_q$ and also since k_i and k_s are much smaller than a reciprocal lattice unit cell, it follows that $\mathbf{q} \approx 0$, which means that only phonons near the center of the first Brillouin zone can take part in the process. It can be also shown that lattice imperfections relax this condition and broaden the Raman signals [61].

A typical Raman apparatus (figure 2.8) is composed of a monochromatic coherent light (laser), an optical system to lase the sample and collect the scattered light, a diffraction grating (wave selector) and a detector.

In this work, Raman spectroscopy was performed with the main aim of assessing the crystallization of the samples as a consequence of vacuum and nonvacuum annealing. A Renishaw InVia micro Raman spectrometer, equipped with an optical microscope, was used. An argon ion laser was employed as a monochromatic light source ($\lambda = 514$ nm) and it was focused on the sample through a 50x objective. The power of the laser source was kept at 1 mW, to avoid modifications in the sample due to the high intensity of radiation. All spectral acquisitions, except when stated, consisted in 30 accumulations, each 10 seconds long.

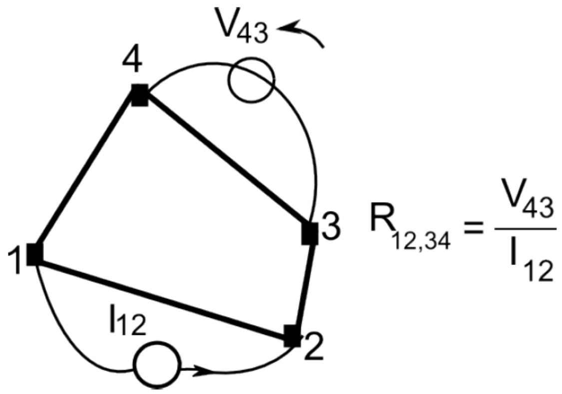

Figure 2.9: Scheme of the four point probe. From [63].

2.5 Van der Pauw method (four-point probe)

The most widespread method for the electrical characterization of thin films is the four-point probe method proposed by Van der Pauw in 1958 [62]. Supposing to have a continuous (with no holes) thin film of uniform thickness, it is possible, independently of the sample's shape, to obtain and calculate its electrical properties.

Four contacts of negligible size and resistance are placed onto the sample, and impressed current (at a known value) flows between two of the four electrodes. The voltage drop between *the other two electrodes* is measured (figure).

This procedure is carried out for the four pairs of adjacent contacts, and then repeated inverting the current direction, for a total of *eight* configurations. Since the current is at a fixed and known value, the degrees of freedom in each configuration are limited. In particular it can be shown that

$$R_{21,43} = R_{12,43}$$

$$R_{32,41} = R_{23,14}$$

$$R_{43,12} = R_{34,21}$$

$$R_{14,32} = R_{41,32}$$

$$R_{21,34} + R_{14,23} = R_{43,12} + R_{34,21}$$

$$R_{32,41} + R_{23,14} = R_{14,23} + R_{41,32}$$

If this holds, then it's possible to evaluate the average resistance values on two sides of the sample, called R_a and R_b. The sheet resistance R_s of the sample is given by Van der Pauw's equation:

$$\exp -\pi \frac{R_a}{R_s} + \exp -\pi \frac{R_b}{R_s} = 1$$

which in the case of a square sample takes the form

$$R_s = \frac{\pi}{\ln 2} R$$

The resistivity is quickly given by

$$\rho = R_s d$$

where d is the thickness of the film.

Using the same setup it is also possible to measure the carrier type, concentration and mobility, by exploiting the Hall effect. If a magnetic field **B** is orthogonally applied to a flux of charges, the Lorentz force will induce some charge separation, which in turn will create a transverse potential difference. This *Hall voltage* is inversely proportional to the carrier density as

$$V_H = \frac{IB}{qdn}$$

where q is the charge of the carrier, negative for electrons, positive for holes. The sign of the voltage reveals the carrier type, since all other variables are known. Carrier mobility can be calculated from equation

$$\sigma = en\mu$$

of the Drude model (see also Appendix).

The measurements are performed the same way as the resistivity ones, except "cross" configurations are used instead of parallel ones. By setting a current (in both directions) across opposite electrodes, four configurations are obtained. Since the magnetic field can be inverted too, a total of eight configurations can be reached. Also, in order to separate the naturally arising voltage contribution of flowing currents from the Lorentz-induced Hall voltage, zero-B measurements are performed as well.

The apparatus used in this work comprises a Keithley 2400 SourceMeter, used as a current source, and a Keysight 34972A LXI Data acquisition unit controlled remotely with a computer, to log the voltage measurements. A custom built switch allowed to progressively select every required electrical configuration. Five pieces of data were collected for for each configuration and then averaged before proceeding with the above described calculations, which were performed by an ad-hoc made Matlab code. Hall measurements were performed using a 0.57 T permanent magnet. In order to obtain an error bar, each sample was characterized three times.

2.6 UV-vis-NIR spectrophotometry

When a film surface is hit by electromagnetic radiation, a portion of it will be transmitted, while another portion will be reflected. Also, as light travel across the whole thickness, some of it will be absorbed and some will be scattered. To assess these quantities across a selected portion of the electromagnetic spectrum, a spectrophotometer can be used. Light is shone from a lamp through the sample, at various frequencies. The portion of light that *comes back* is collected by some detectors.

Adding together the contributions from the reflected, transmitted, absorbed and scattered intensities one should get the overall intensity as in

$$R + T + A + S = 1$$

In particular, the fraction of scattered light is of a certain relevance when porous film are characterized. Traditional spectrophotometers fall short in this respect, since they are unable to collect the light scattered from a film's porous features. The obtained

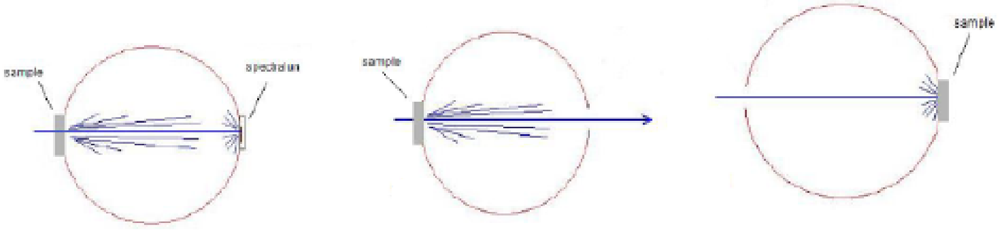

(a) (b) (c)

Figure 2.10: Three measurement schemes were used to determine (a) total transmittance, (b) diffuse transmittance and (c) reflectance.

measurements would not be correct. In order to collect all the light scattered from a sample, an *integrating sphere* must be used. This module is made of *Spectralon*, a fluoropolymer having the highest diffuse reflectance of all materials. The light collected from the sphere comes back *as if* it was reflected normally.

Three measurements schemes were used in this study, as shown in figure 2.10. They differ among themselves with respect to sample position and the possibility of having an extra opening on one side of the sphere. By performing measurements according to these three schemes one can then – by difference – calculate absorbance A and haze factor

$$HF = \frac{S}{T}$$

It is to be noted that since the samples were deposited on glass substrates, a normalization of the data was necessary, and it was performed according to

$$T_{film} = \frac{T_{tot}}{T_{glass}}$$

$$R_{film} = R_{tot} - (R_{glass} T_{film}^2)$$

The measurements were performed at the Center for Nanoscience and Technology (CNST) of the Italian Institute of Technology (IIT) in Milan, using a Lambda 1050 UV/vis/NIR system with a Perkin Elmer 150 nm integrating sphere. Transmittance and reflectance measurements were performed in the range 250-2500 nm, with a data interval of 2 nm.

Chapter 3

From compact films to nanoparticles

In this chapter, different deposition conditions are investigated, with the aim of obtaining porous films and nanoparticles. As explained in section 2.1, this can be achieved by employing pressures higher than those used for depositing compact films [54]. The pressure range spanning from 4 Pa to 15 Pa was investigated, as well as the effect of using different background gas compositions, (which modify the deposition chemistry). The effect of post-annealing treatments on the nanoparticle assemblies was also studied. However, before proceeding with annealing the films, a preliminary investigation of different thermal treatments was performed on optimized 1 Pa TaTO layers (section 3.1). On the basis of the outcome of this study, two annealing cycles were chosen in order to treat nanoparticles.

3.1 Compact films

As reported from previous works [50][54], compact films are obtained by working at pressures not greater than $2 \sim 4$ Pa. The exact pressure value for synthesizing "optimum" compact films, i.e. featuring the lowest possible resistivity, depends on fluence, and with the deposition conditions used in this work sits at 1 Pa of pure O_2. Lower pressure values still yield compact films, but with worse electrical properties. Higher pressures (at least 4 Pa) allow to deposit films which exhibit some columnar traits, and with pressures even higher, nanoparticles are obtained (see section 3.2).

The optimized deposition conditions refined by Ornago [54] yielded the following values for electrical properties:

$$\rho = 8 \times 10^{-4}\ \Omega\text{cm}$$

$$n = 9.3 \times 10^{20}\ \text{cm}^{-3}$$

$$\mu = 8.4\ \ \text{cm}^2\,\text{V}^{-1}\text{s}^{-1}$$

These quantities refer to a 180 nm compact film deposited at 1 Pa in a pure oxygen atmosphere. As it can be seen in figure 1.21, the electrical properties tend to stabilize in the $50 \sim 200$ nm thickness range, suggesting bulk values of these orders of magnitude for these quantities. Ornago's values have been used in this thesis work as a tool of comparison to evaluate the properties of porous films and nanoparticle systems. In particular, in section 3.2 the effects of an increased pressure on film morphology, Raman

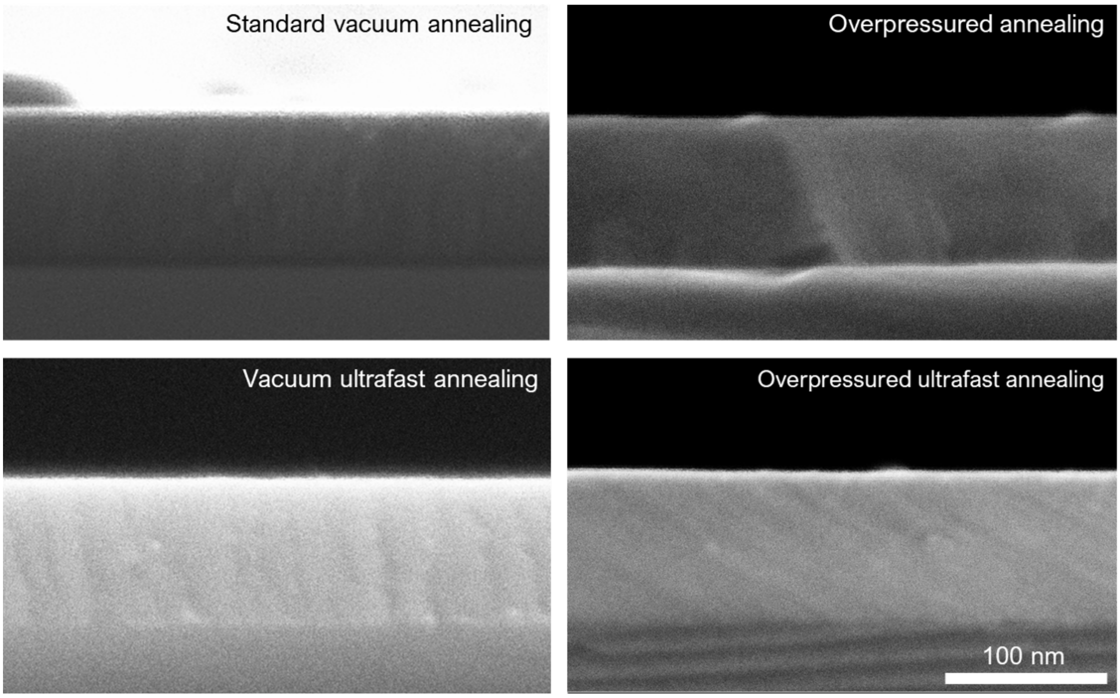

Figure 3.1: SEM images of compact TaTO films deposited at 1 Pa of pure O_2 annealed under different conditions: (a) standard vacuum annealing [54], (b) ultrafast vacuum annealing, (c) overpressured annealing in an Ar/H_2 atmosphere and (d) ultrafast overpressured annealing in an Ar/H_2 atmosphere. All samples are 100 nm thick and were annealed at 550°C.

spectrum and optical absorption spectrum are discussed, and the results are compared with those of the 1 Pa samples.

Compact 1 Pa films were deposited in this work in order to explore the effect and study the effect of different thermal treatments, as will be discussed next.

3.1.1 Effect of thermal treatments

A preliminary study of different thermal treatments was made before annealing porous and nanoparticle films, in order to determine which procedures were to be chosen. As reported more extensively in section 2.2, three annealing treatments, other than the "standard" one, were tested, based on previous works [53] and new ideas. In particular, it must be specified that both standard annealing cycles and overpressured ultrafast annealing cycles have already been performed by Mazzolini, although with a different apparatus. Therefore, one of the goals of this preliminary study was to replicate those results and corroborate their validity. The annealing tests were performed on 1 Pa samples in order to verify their effect on well known sample types.

Different annealing treatments do not seem to have an effect on the film morphology, as shown in figure 3.1. All films appear compact, and the only observed features are probably due to an imperfect cleavage of the samples for cross-section SEM analysis.

The samples reported in figure were Raman-characterized in multiple spots to assess the consistency of the crystal structure, and they proved to be homogeneous, with one exception. The sample treated with an overpressured annealing treatment features at least two types of spectra, even though both distinctly referable to anatase (figure 3.2). The

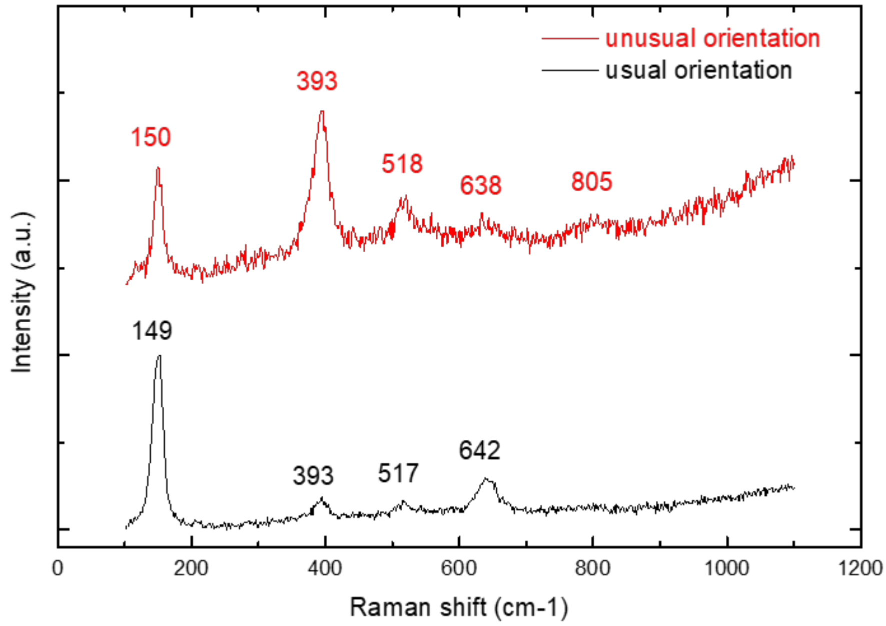

Figure 3.2: Raman spectrum of a compact TaTO film annealed in a Ar:H_2 atmosphere. Some crystalline grains exhibited a different orientation. Except for a weak signal at 805 cm^1 (top spectrum), the peak positions for both spectra are those typical of anatase. The top spectrum has widths for the $E_g(1)$ and B_1g peaks equal to 15 and 21 cm^{-1}, respectively, while the bottom one has 29 and 30 cm^{-1}.

Table 3.1: $E_g(1)$ peak position and width as a result of different thermal treatments

Thermal treatment	Peak position (cm^{-1})	Peak width (cm^{-1})
Standard	151.9	13.8
UFA	151.1	14.0
OPA	149.2	21.0
OPUFA	151.2	15.7

quaint spectra corresponds to an abnormal orientation for the anatase grain. As a matter of fact, the peak positions correspond to the expected value for anatase (except for a band at 805 cm^{-1}).

Small differences emerge when the Raman spectra are compared (figure 3.3). All samples crystallized into anatase and the obtained spectra exhibit comparable values for the position of the $E_g(1)$ peak, except for the OPA sample, whose spectrum exhibits a lot of noise as well. Details are reported in table 3.1.

The imperfect crystallization was likely caused by the long exposure (one hour of dwell time) to the annealing atmosphere. Conversely, samples exposed to Ar:H_2 for a short time – or to a vacuum – crystallized correctly, as confirmed by Raman analysis.

These results are coherent with the electrical characterization of the samples, performed via four-point-probe analysis. The badly crystallized sample turned out to be too insulating to be measured with the instrumental setup at our disposal, while the other ones were successfully characterized. The electrical properties of the samples are reported in table 3.2. Vacuum ultrafast annealing treatments yielded slightly more conducting films

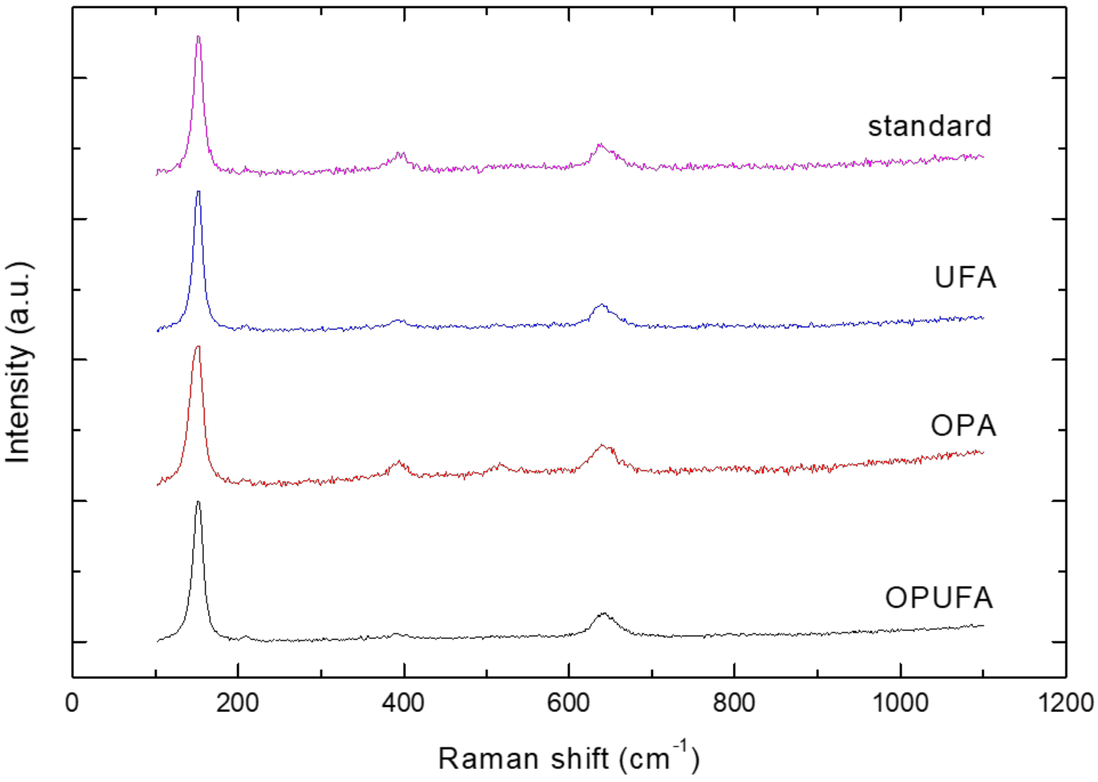

Figure 3.3: Raman spectra comparison for different annealing types: standard, vacuum ultrafast (UFA), overpressured (OPA) and overpressured ultrafast (OPUFA). For the OPA sample the *normal* spectra is reported. All samples have crystallized into the anatase phase.

Table 3.2: Electrical properties of 1 Pa O_2 TaTO after different thermal treatments.

Thermal treatment	Resistivity (Ωcm)	Carrier density (cm^{-3})	Mobility (cm^{2}V^{-1}s^{-1})
Standard	8.0×10^{-4}	9.3×10^{20}	8.4
UFA	7.5×10^{-4}	1.1×10^{21}	7.9
OPA	—	—	—
OPUFA	1.1×10^{-2}	$\sim$	$\sim$

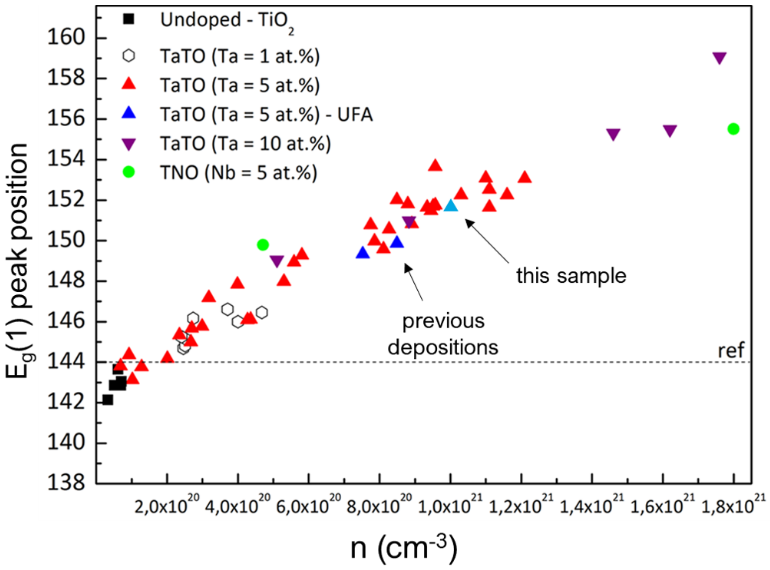

Figure 3.4: Raman shift versus carrier density. Ultrafast annealed samples from previous works are also highlighted. Adapted from [51].

compared to standard ones, even though all the electrical properties lie in the same orders of magnitude. The measured carrier density of 1.1×10^{21} cm^{-3} was among the highest obtained with a tantalum content of 5%, and was plotted against the position of the $E_g(1)$ peak of the Raman spectrum, located at 151.1 cm^{-1}, as shown in figure 3.4. Conversely, overpressured ultrafast annealed films showed worse electrical properties. Resistivity was more than one order of magnitude higher, and Hall measurements were deemed unreliable. This is not consistent with the results obtained by Mazzolini [53], possibly due to slightly different experimental conditions. In that work, a gas composition of $\text{Ar} : \text{H}_2 = 98 : 2$ was used, while in this work the hydrogen gas percentage was 3%.

Since the most effective thermal treatments proved to be the standard one and the vacuum ultrafast one, it was chosen to use these two, and to compare their effects, during the study of TaTO nanoparticles.

3.2 Porous films and nanoparticles

In order to deposit non-compact films it is necessary to increase the deposition pressure. From previous works it was known that in the case of TaTO and undoped titania a pressure of 15 Pa is enough to obtain hierarchical nanoparticle structures, although this result was obtained by working with different fluence and wavelenght values [50]. The pressure range spanning from 4 Pa to 15 Pa was studied, in order to observe the transition from a compact morphology to a hierarchical one. Even though films were mainly deposited in an argon-oxygen mixture, some were deposited in pure oxygen for comparison. Besides the effects of the deposition atmosphere, those concerning the annealing process were studied.

All samples were characterized by SEM to determine film morphology, and by Raman spectroscopy to assess anatase crystallization. When possible (that is, in the case of compact films) electrical properties where investigated by four-point-probe analysis.

Porous samples where characterized by UV-vis-NIR spectrophotometry in order to determine the transmittance, reflectance and absorbance. Tauc plot calculations [64] were also performed to estimate the optical bandgap.

3.2.1 Effects of the deposition atmosphere

Two deposition atmospheres were studied: pure oxygen and an $Ar : O_2 = 5 : 1$ mixture. This gas composition ratio was based on Ornago's work [54]. The composition had been optimized for 4 Pa depositions and was thus *extended* to higher pressures in this work. As explained in section 1.3.3 and section 1.4, an excessive oxygen content in the deposition atmosphere leads to the nanostructures being *not substoichiometric enough*, which is detrimental to the carrier density. While in this work most samples were deposited in an argon-oxygen mixture, some reference films were deposited in pure oxygen as well, for comparison.

From a purely morphological point of view, the most evident effect of introducing argon gas into the mixture – compared to pure oxygen depositions – is that of *compacting* the film. This happens because argon atoms are less massive than oxygen molecules, therefore the background atmosphere has less "stopping power" against the ablated species traveling towards the target. For equal deposition times, films deposited in an $Ar{:}O_2$ mixture appear thinner, as shown in picture 3.5.

Samples were deposited in an $Ar : O_2 = 5 : 1$ atmosphere at the pressures of 4 Pa, 6 Pa, 8 Pa, 10 Pa and 15 Pa, in order to study the evolution of the films in this range, and to better define at what point compact structures leave way to nanoparticle assemblies. Figure 3.6 shows SEM images for these samples; a fairly smooth transition from a compact morphology to nanoparticles can be observed. Intermediate pressure values yielded porous/columnar structures.

3.2.2 Effects of the standard annealing treatment

The first annealing process to be investigated was the *standard annealing process* (section 2.2). From the morphological point of view (figure 3.7), few differences can be observed in the case of films deposited in an argon-oxygen mixed atmosphere. Conversely, pure oxygen-deposited films seem to exhibit some sintering effects (figure 3.8), even though this is somewhat open to interpretation. A direct comparison between the films' morphology prior to and after the annealing process is provided in figure 3.9.

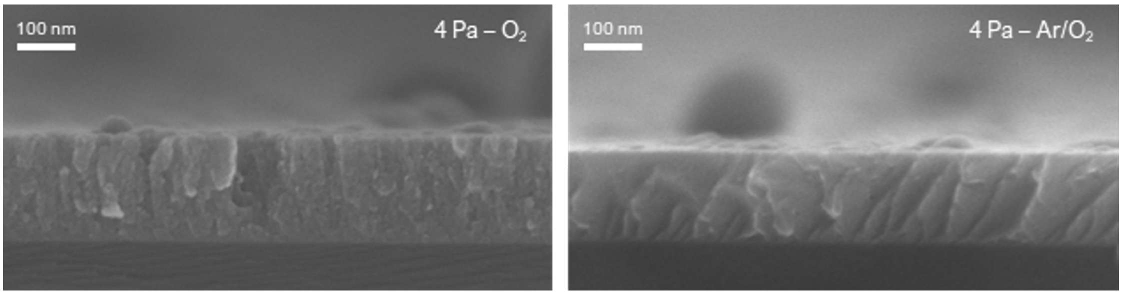

Figure 3.5: SEM images of TaTO films deposited at different pressures in pure oxygen (left) and Ar/O_2 mixture (right).

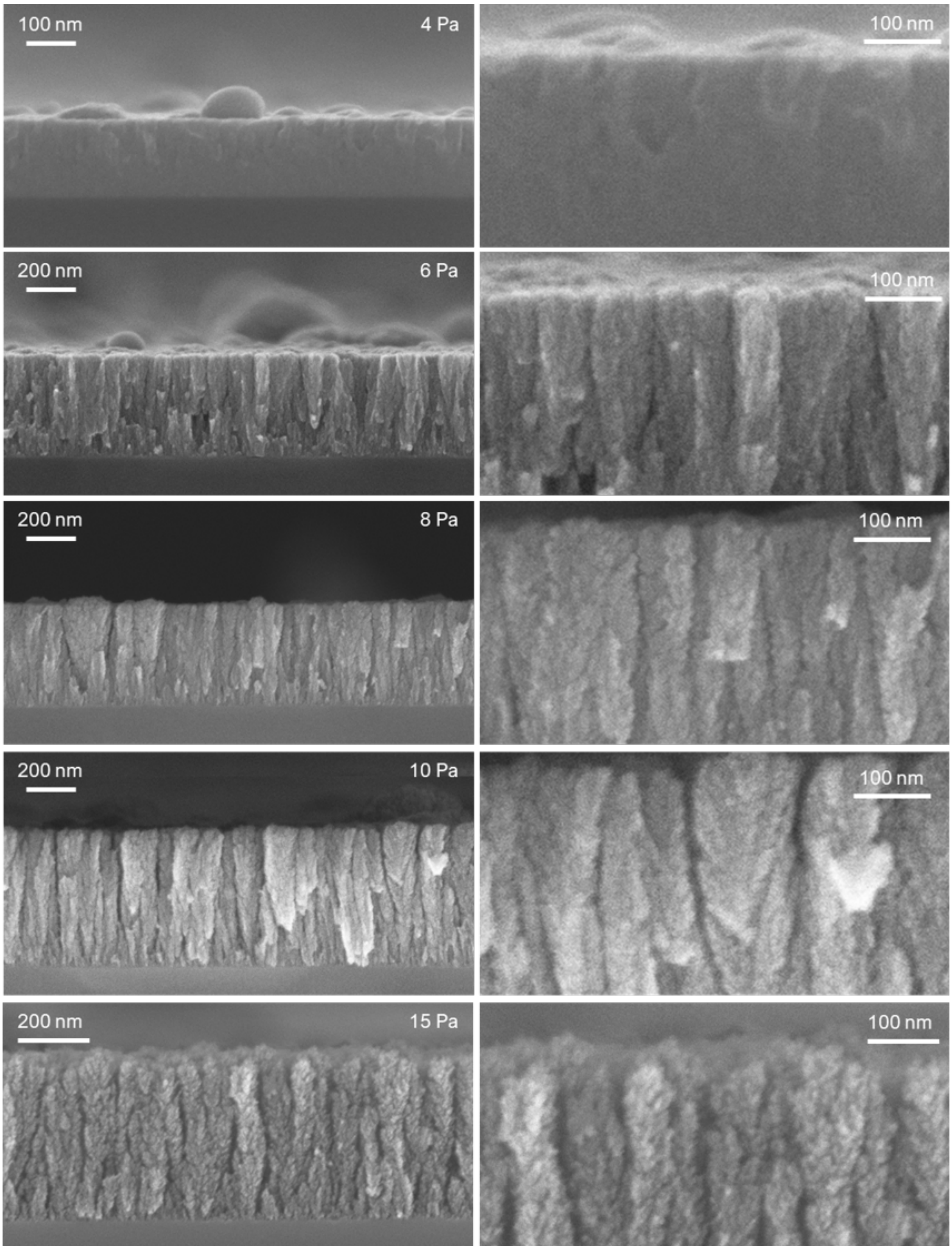

Figure 3.6: SEM images of TaTO films deposited at different pressures. The pictures were taken before the thermal treatment. It is possible to distinguish compact films at 4 Pa, porous films at 6 Pa, 8 Pa and nanoparticle asssemblies for 10 Pa and 15 Pa. All samples were deposited in an Ar:O_2 atmosphere. The films were synthesized with different deposition times, therefore film thickness is not to be looked at. Details for every film are shown on the right.

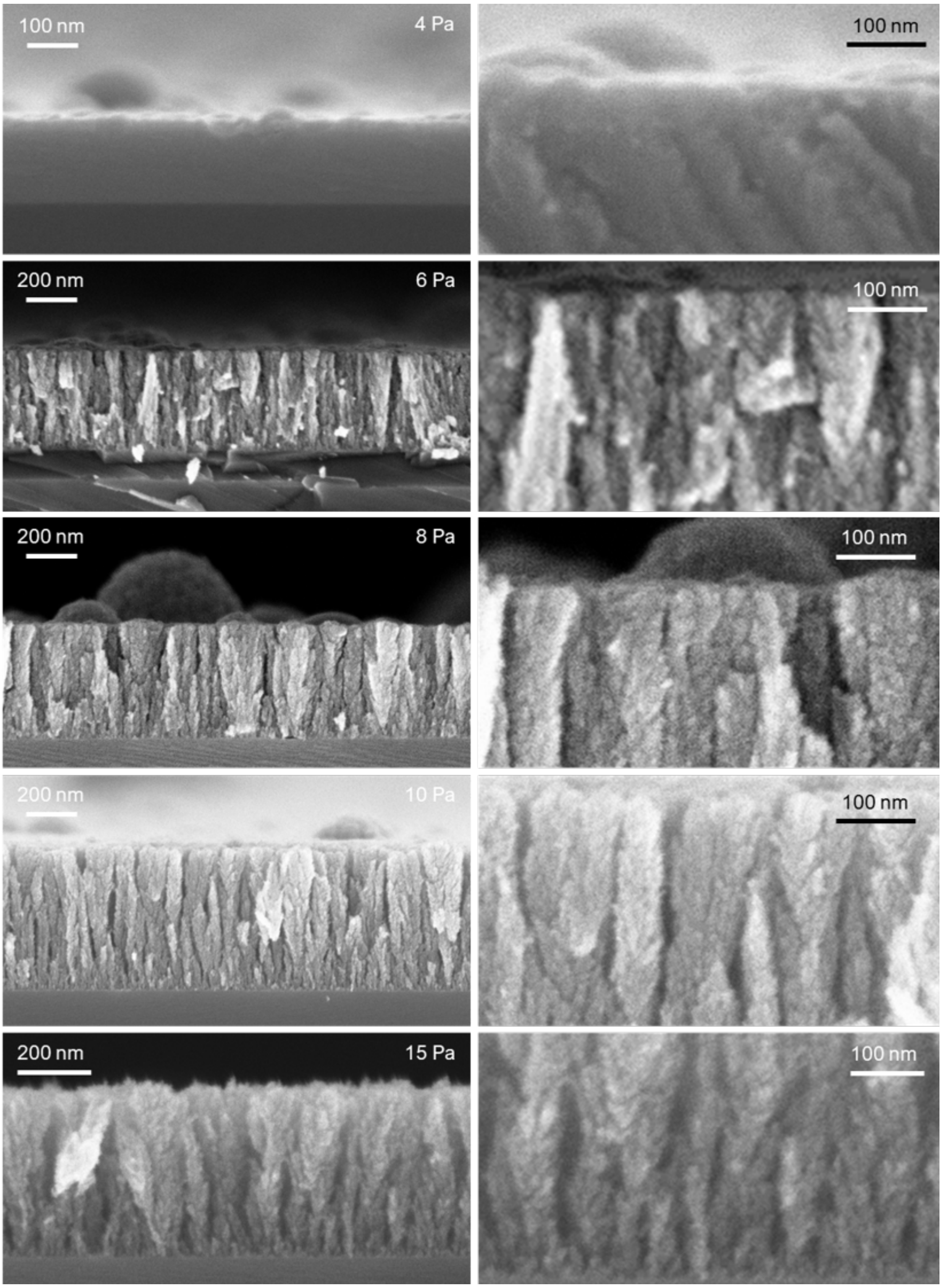

Figure 3.7: SEM images of TaTO films deposited at different pressures. The pictures were taken after a standard annealing treatment. It is possible to distinguish compact films at 4 Pa, porous films at 6 Pa, 8 Pa and nanoparticle asssemblies for 10 Pa and 15 Pa. All samples were deposited in an Ar:O_2 atmosphere. The films were synthesized with different deposition times, therefore film thickness is not to be looked at. Details for every film are shown on the right.

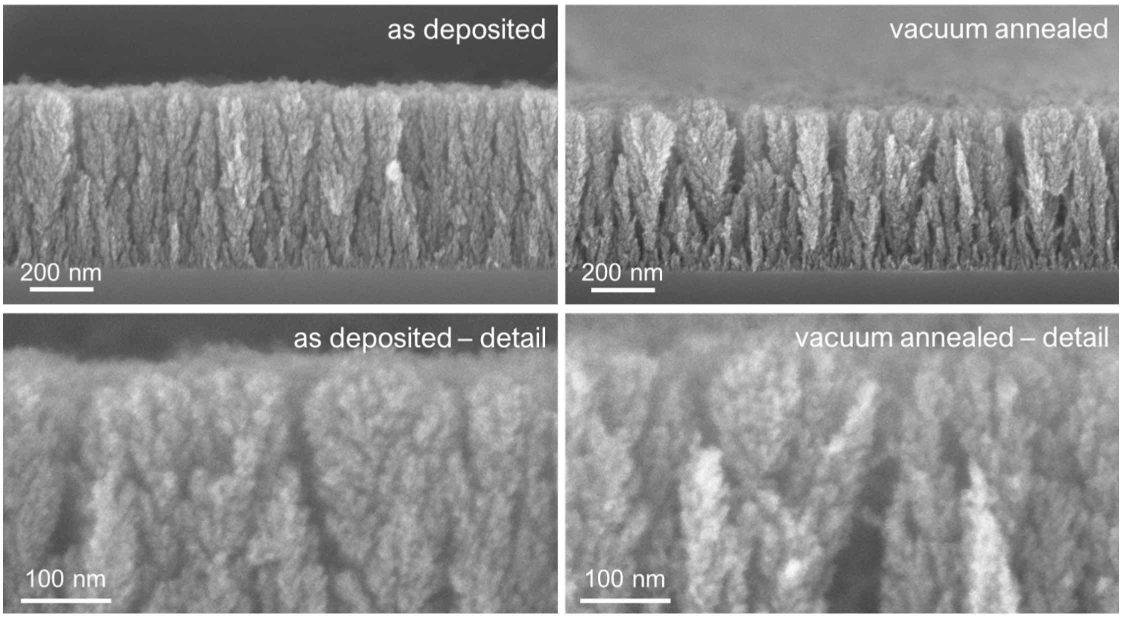

Figure 3.8: Effect of a standard annealing on a TaTO film deposited at 15 Pa of pure O_2. A weak sintering effect is visible: it is easier to discern among different nanotrees.

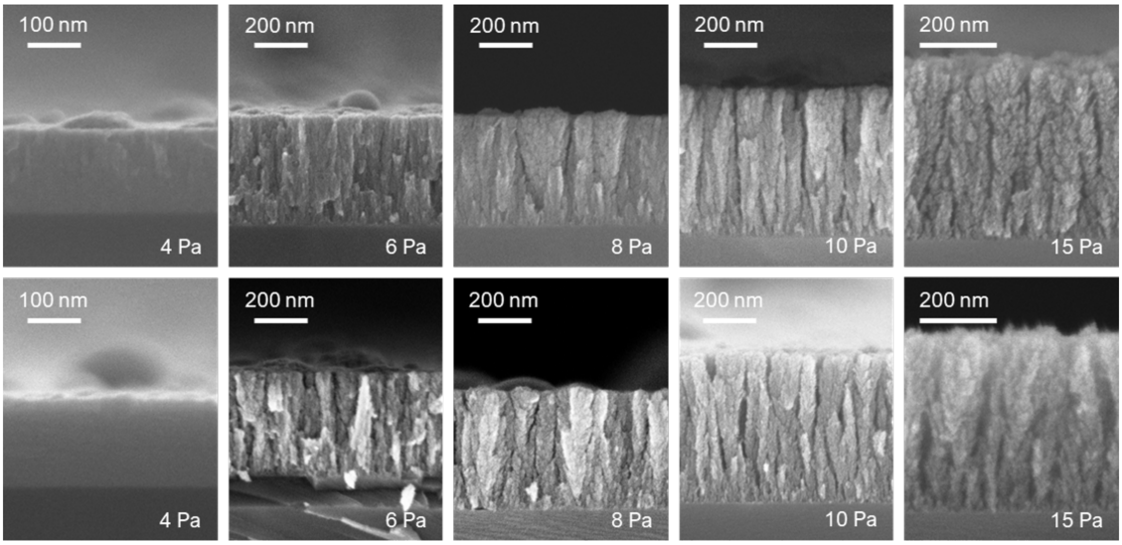

Figure 3.9: Effect of a standard annealing treatment on TaTO films deposited at various pressures in an argon-oxygen mixture. Top: *as deposited* films. Bottom: films after a standard annealing treatment.

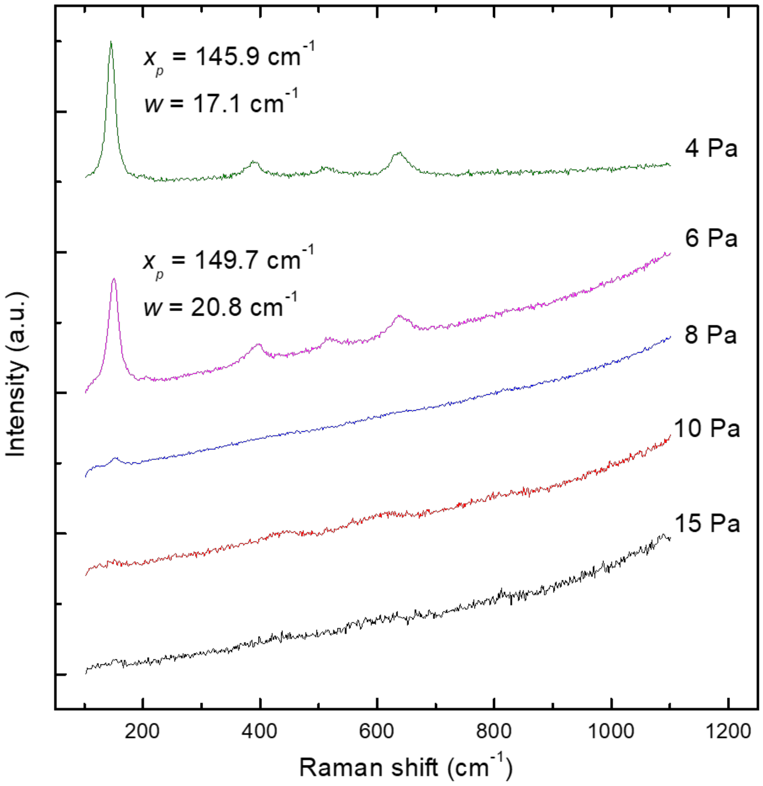

Figure 3.10: Raman spectra of TaTO films deposited at different pressures. It is possible to observe a photoluminescence background in the more porous films. All samples were deposited in an Ar/O_2 atmosphere. The pictures were taken after a standard thermal treatment.

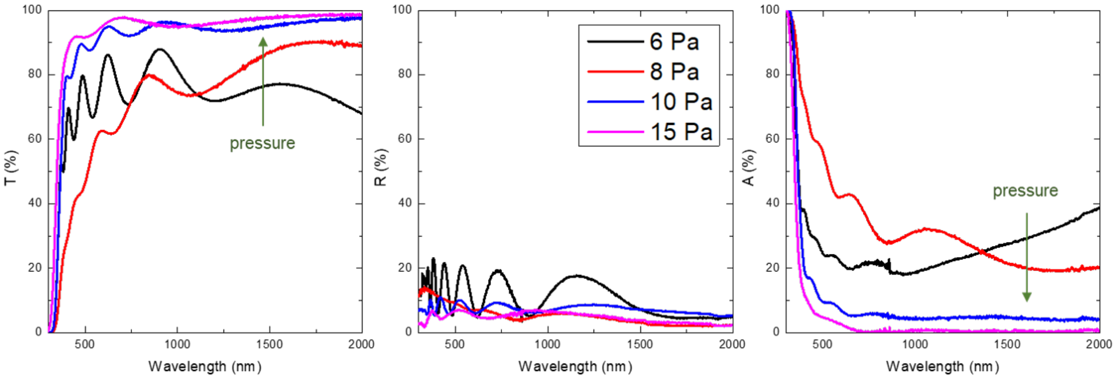

Figure 3.11: Transmittance, reflectance and absorption spectra of nanoporous films deposited at different pressures in an Ar:O_2 atmosphere.

The crystallization of the annealed films was investigated by Raman analysis. It was found that compact films had correctly crystallized into anatase, while the same cannot be said with certainty in the case of nanoparticle assemblies. Indeed, the latter show a strong background rising towards higher Raman shifts, and a weak hint of the $E_g(1)$ peak. A possible explanation for this is to be looked for in the occurrence of photoluminescence. A nanostructure with a high surface area (as high-pressure films are expected to be) could be very sensitive to the reducing character of vacuum, and a long time exposure to this atmosphere would result in a severe oxygen desorption, leading to the formation of defects (in-gap states) which are the cause for photoluminescence. This effect is stronger as pressure increases, suggesting a correlation with the film porosity. The evolution of Raman spectra and the position of the $E_g(1)$ peak (when clearly present) as a function of the deposition pressure are shown in figure 3.10.

Electrical characterization was possible only on 4 Pa samples (deposited in both oxygen and mixed atmosphere, and treated by a standard annealing cycle), while more porous ones were not conducting enough to be measured with the available equipment, and even the "conducting" ones provided unreliable Hall mobility and carrier density values. The measured resistivities were $\rho = 4.0 \times 10^{-2}\,\Omega$cm for the pure oxygen sample and $\rho = 2.2 \times 10^{-2}\,\Omega$cm for the mixed atmosphere sample, coherently with previous works [54].

It is important to notice that these samples where characterized by the four-point-probe method, which gives *in plane* electrical properties. Having the nanoparticle assemblies a strong directionality, *cross plane* properties would be also relevant. Some attempts in this sense have been done [50] but could not provide absolute/intrinsic results. Even if cross plane conductivity proved very low due to nanotree porosity, which hinders mobility, the system might still have a significant value of carrier density, and a plasma wavelength in the NIR region.

The effect of an increase in the deposition pressure can also be seen in the optical properties of the samples. The main observed behavior (figure 3.11) is an increase of transmittance in the NIR range as pressure increases, coherently with previous works [54]. More compact films, conversely, have a stronger absorbance in this region.

3.2.3 Effect of ultrafast annealing treatment

The second thermal treatment that was tested was the *ultrafast annealing treatment* (section 2.2). Due to technical constraints, it was not possible to treat all samples and allow for a full comparison between the two annealing processes. SEM images of the fast annealed samples are reported in figure 3.12. Figure 3.13 shows instead the same sample before any thermal treatment and after a standard and an ultrafast annealing treatment, respectively. No great change can be observed – from a purely morphological perspective – when the two process are compared.

Differences between thermal treatments emerge more clearly when Raman spectra are compared, as shown in figure 3.14. While all films show significant photoluminescence backgrounds, this effect is weaker in the case of ultrafast annealed samples. At first glance, peaks appear more pronounced, suggesting that a better nanoparticle crystallization is promoted by this kind of treatment. This is likely due to a lower oxygen desorption during the ultrafast process, for purely *kinetic* reasons. However, while the 6 Pa spectrum is that of anatase, the same cannot be said in the case of the 8 and 10 Pa spectra. A more detailed analysis of the observed features reveals that while the first one is at 144 cm^{-1}, the other two sit *around* 450 cm^{-1} and 600 cm^{-1}, respectively. These values do not belong to anatase: in fact, they are probably due to the presence of rutile or to the joint presence of anatase *and* rutile (see section 1.3 for the spectrum of rutile). The occurrence of rutile in films deposited at high pressure has been already reported by Di Fonzo *et al.* [65] in the case of undoped titanium oxide annealed in air at 400°C. In that case – but the same is true for this work – rutile formation was attested at an annealing temperature below the anatase-to-rutile transition temperature, suggesting that rutile nanocrystals might have been already present in the *as deposited* film, and later acted as low-T nucleation centers. Despite it being somewhat puzzling, the shapes of the here presented Raman spectra can be rationalized as follows:

- higher deposition pressures favor in-plume nucleation of rutile clusters;
- such clusters act in turn as crystallization seeds for rutile;
- thermal treatments below the anatase-to-rutile transition temperature are able to promote rutile formation, *unless* they have a strong reducing character.

In particular, the standard annealing cycle would qualify as reducing, while the UFA cycle would not, despite being in vacuum, due to its short duration. The effect of the thermal treatment may fade as pressure increases, as a greater amount of rutile is formed in the "amorphous" *as deposited* film. It must be said that while this is a reasonable explanation for the observed phenomena, more tests – on wider pressure and *annealing time* ranges – should be performed, in order to verify it.

Figure 3.15 shows the same spectra reported in figure 3.14, range, after a background subtraction. High pressure spectra appear quite noisy, revealing the presence of a strong amorphous fraction in the films. Nevertheless, a very rough estimate of the relative content of anatase and rutile can be made. A study on different $\mathrm{TiO_2}$ powder mixes by Li Bassi *et al.* found a correlation between the anatase and rutile content ratios and the Raman intensity of their characteristic peaks. More specifically it was shown that

$$\frac{x_A}{x_R} \approx \frac{I_A(144)}{I_R(447)+I_R(612)}$$

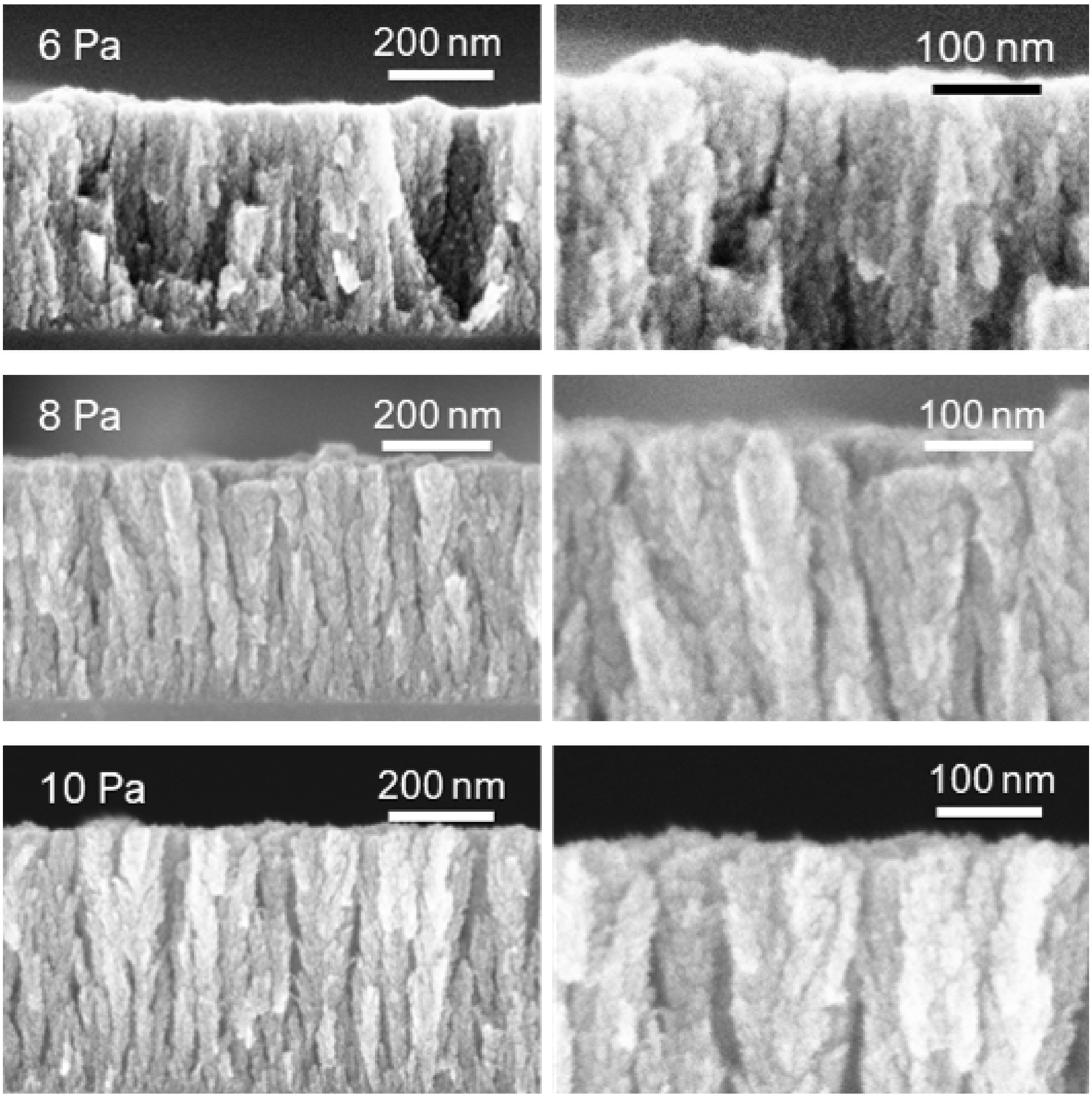

Figure 3.12: SEM images of TaTO films deposited at different pressures. The pictures were taken after an UFA treatment. All samples were deposited in an Ar:O_2 atmosphere. The films were synthesized with different deposition times, therefore film thickness is not to be looked at. Details for every film are shown on the right.

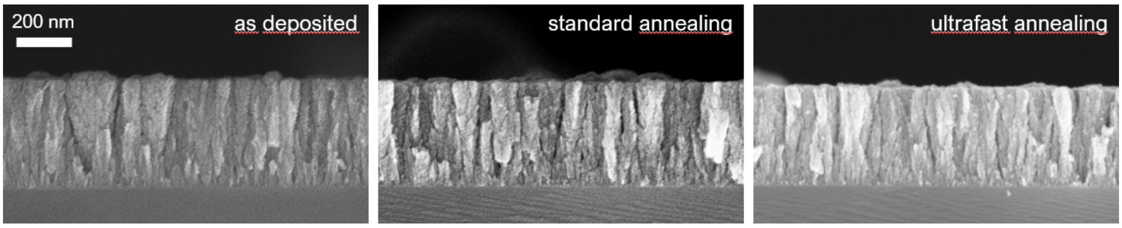

Figure 3.13: SEM images of a TaTO film deposited at 8 Pa in Ar:O_2, *as deposited*, after a standard annealing cycle and after a vacuum ultrafast treatment.

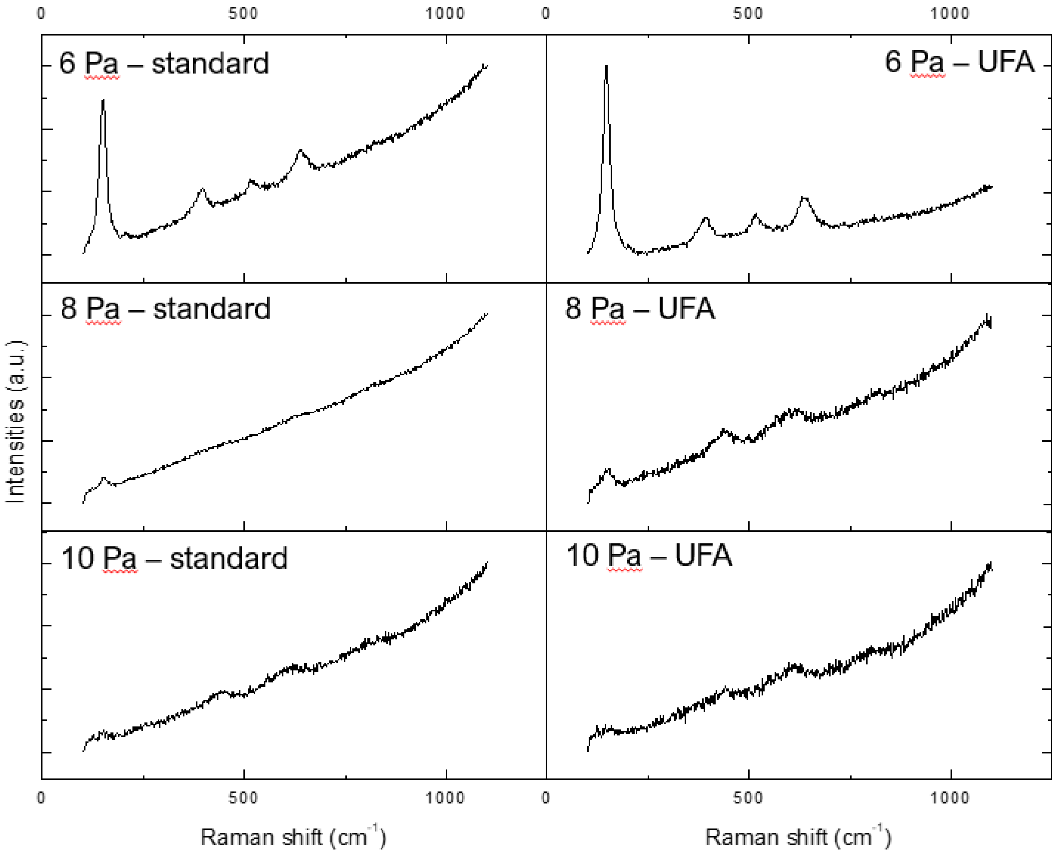

Figure 3.14: Raman spectra of TaTO films deposited at different pressures and treated with a standard or ultrafast cycle. Photoluminescence is stronger for higher pressures and for standardly annealed films.

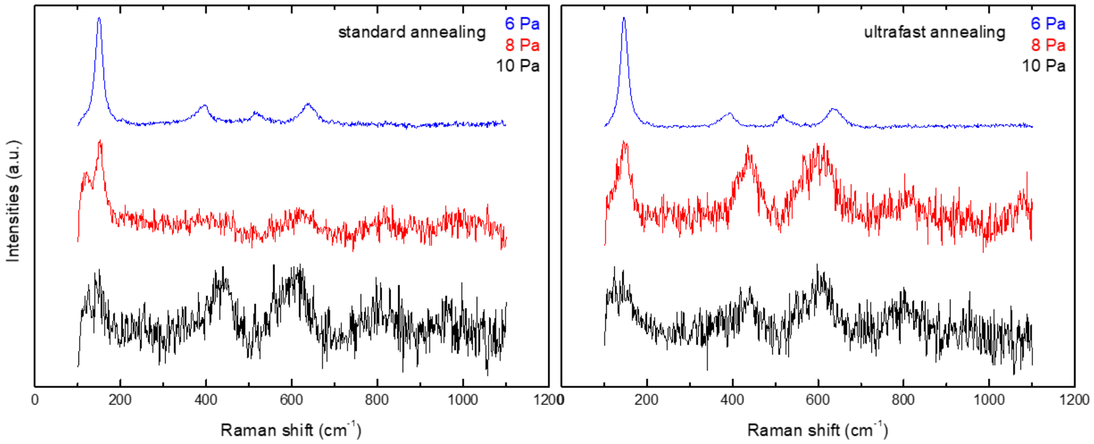

Figure 3.15: Effect of thermal treatments and increasing pressure on TaTO films. A baseline subraction reveals the presence of rutile, which is stronger for higher pressures and after an ultrafast annealing, rather than a standard one. All sample but those deposited at 6 Pa show very noisy spectra, indicating the presence of a strong amorphous fraction. The $E_g(1)$ peak for the 6 Pa sample is at $x = 146.4$ cm^{-1} and has $w = 21.2$ cm^{-1}.

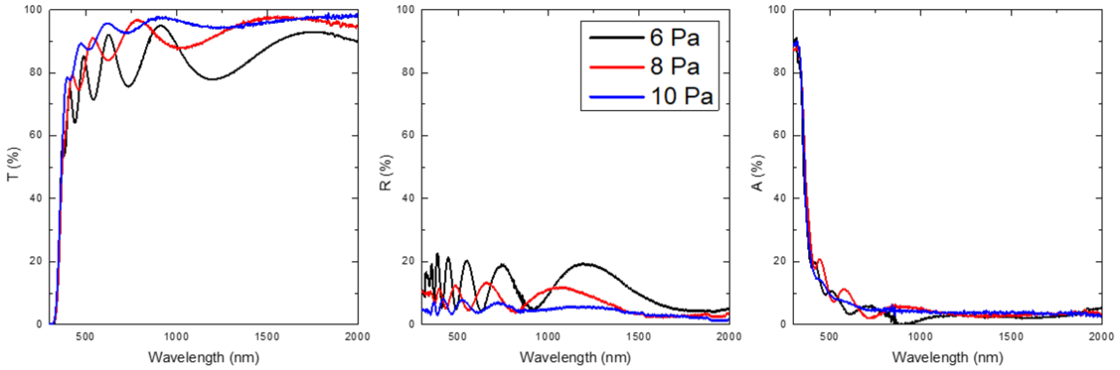

Figure 3.16: Optical spectra of 6 Pa, 8 Pa and 10 Pa samples after an ultrafast annealing process.

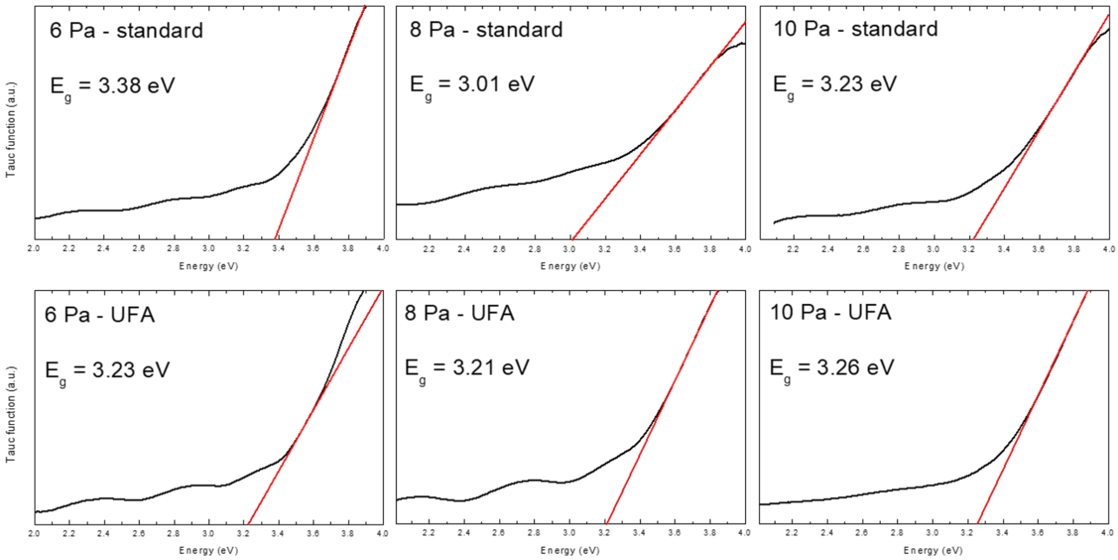

Figure 3.17: Tauc plots for annealed nanoporous systems. The Tauc function was taken to be $(\alpha\hbar\omega)^{0.5}$ instead of $\alpha^{0.5}$ to better suit the poor material crystallinity.

where x_A and x_R are the anatase and rutile fractions, while $I_A(144)$, $I_R(447)$ and $I_R(612)$ are the peak intensities of the modes at 144 cm^{-1} (anatase), 447 cm^{-1} (rutile) and 612 cm^{-1} (rutile).

By calculating the intensity for the relevant peaks it was found that the content of rutile was about three times as much than that of anatase, except in the case of the standardly annealed 8 Pa film, which has a much stronger peak at 144 cm^{-1}. It must be stressed that this method provides no information about the abundance of the amorphous phase, whose strong presence is suggested by the spectral noise.

The type of annealing also influences the optical spectra of the films. As shown in figure 3.16 the NIR transmittance is much higher and the absorbance is much lower in the case of ultrafast annealed samples.

3.2.4 Estimate of optical bandgaps

A bandgap estimate for the films was performed by Tauc plot calculations [64]. Indeed, a relation exists between the transimission and reflection spectra of a material and its optical bandgap. The theoretical value of the absorption coefficient α for photons of energies *just above* the optical gap E_g is given by

$$\alpha = C(\hbar\omega - E_g)^{1/r}$$

where C is a constant dependent on the optical transition matrix element, while r indicates the type of transition in the considered material; in the case of direct gaps it is equal to 2, while in the case of indirect gaps it it equal to 0.5. If we isolate α^r (the *Tauc function*) we get a function of the energy

$$\alpha^r = C(\hbar\omega - E_g)$$

which is linear for values of $\hbar\omega$ just above E_g. Thus it is enough to know α and set $\hbar\omega = 0$ to get a bandgap value. Since this method was developed for crystalline material, a variation has been used here [66] which is more appropriate for amorphous materials. The absorption coefficient for the material was calculated from the Lambert-Beer law as

$$\alpha = -\frac{1}{d} ln \frac{T}{1-R}$$

The plots concerning 6 Pa, 8 Pa and 10 Pa samples are reported in figure 3.17. The Tauc coefficient used in this case was $r = 0.5$, which is valid for anatase (indirect gap). While the 6 Pa sample definitely has a strong anatase fraction, this assumption is not exact in the case of more porous films, as highlighted by Raman analyses (section 3.2.3). Thus, Tauc calculations were also performed assuming $r = 2$, which would be suitable for rutile (direct gap). Unfortunately, the linear region was not wide enough and attempts at calculating the direct gap resulted in values of the order of 3.6 eV, which is too high and inconsistent with previous works and literature [50]. Even the indirect gap calculations are quite baffling: while the ultrafast annealed samples are consistently stable at just above 3.20, the obtained values for standardly annealed ones are not consistent among each other. This could be – again – attributed to an insufficiently wide linear trend range. Conversely, if the UFA plots are assumed to be reliable, it would mean that the effect of doping was scarce.

Summary A preliminary study on annealing processes was made on TaTO compact films, and on its outcome it was decided to treat the nanoparticles with a standard vacuum annealing treatment and a vacuum ultrafast annealing treatment. By exploring the 4–15 Pa pressure range, films having different porosity were deposited. After a post annealing treatment, not all samples crystallized into anatase. The more compact ones had definite Raman signals (successful crystallization) while nanoparticle spectra were tampered by photoluminescence effects, and showed high levels of noise, attributed to a strong amorphous fraction. A compared analysis of the spectra revealed that the ultrafast annealing treatment promotes a slightly better crystallization, albeit into rutile. Fast annealed samples showed a higher NIR transmittance and lower absorbance, and more reliable Tauc plot calculations; however, they did not show signs of successful doping. The main goal of obtaining high carrier density nanostructure was not reached. This could be either due to the deposition process or the post-annealing treatment. In order to assess this, more test should be done. Depositions at different gas compositions should be performed, and the effects of different annealing cycles should be explored.

Chapter 4

Bilayered compact films

In this chapter, the possibility of depositing compact TaTO films on top of undoped TiO_2 substrates is explored. In turn, the substrates were deposited on Si(100) and soda lime glass substrates. Such configurations can be interesting for two reasons. First, TaTO has the basically same lattice structure of titania and this would allow lattice-matched growth of TaTO (albeit in several crystalline domains!) possibly leading to a better crystallinity and smaller surface effects (e.g. surface scattering of carriers). Second, TaTO and titania have different permittivities, and this is a necessary condition to sustain surface plasmon polaritons (SPPs). Such excitations propagate along, but are spatially confined at the interface. Their frequency/wavelength can be modulated by acting on the permittivities of the two materials, as reported in chapter 1 and in the Appendix. Hence the motivations to deposit TaTO on top of undoped titania.

All films (both the bottom and the top layers) were deposited in a pure O_2 atmosphere at the pressure of 1 Pa. The bottom layer was thermally treated in different ways, in order to obtain different values of conductivity, and therefore of permittivity; however, the measurement of the materials' dielectric function is beyond the scope of this work. All samples were characterized by SEM, Raman spectroscopy and, when possible, by four point probe analysis.

4.1 TaTO on reduced titania substrates

The first scheme to be explored was that of reduced substrates. This means that the bottom titania layers were thermally annealed in a vacuum, according to the standard annealing cycle described in section 2.2. This kind of treatment has been shown to lead to a moderate electrical conductivity, entirely relying on oxygen vacancies, of the order of 150 S/cm ($\rho = 7 \times 10^{-3}\ \Omega$cm) [53]. Even though such a material is not exactly an insulator, its conductivity differs from that of TaTO of about one order of magnitude.

Two samples were produced, following two different procedures, as shown in figure 4.1. The first one, which for simplicity's sake will be referred to as *sample A*, was deposited in two steps. An amorphous titania layer, 50 nm thick, was deposited, and subsequently vacuum annealed, to induce anatase crystallization. On top of this polycrystalline layer, a TaTO layer was deposited again 50 nm thick, and the sample was thermally treated again. The second sample (B), was instead synthesized by depositing in series the two layers (50 nm + 50 nm) and annealing the whole thing only once. Two

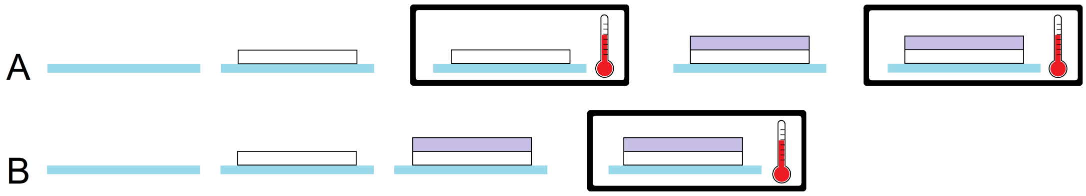

Figure 4.1: Synthesis scheme of titania-TaTO bilayers in which the bottom layer is made of reduced titania. This can be obtained by performing two separate annealing treatments (A) or by annealing both layers at the same time (B).

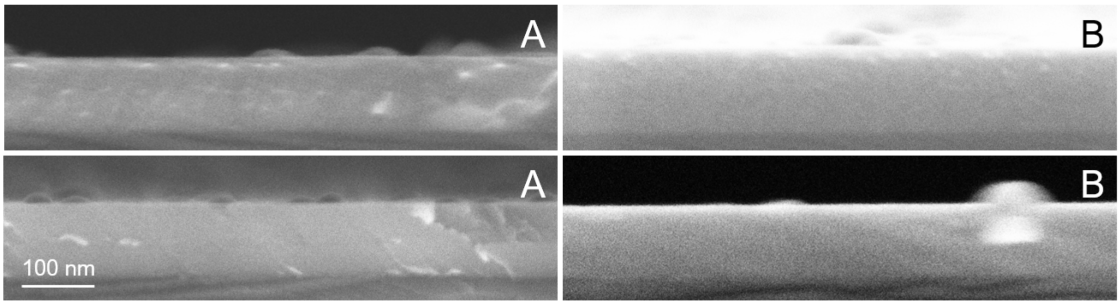

Figure 4.2: SEM images of titania-TaTO bilayers whose bottom layer is made of reduced titania. No clear sign of the interface is visible. The pictures were taken before the final annealing and afterwards.

differences can be expected. One concerns the crystallinity of the TaTO layer. When TaTO is deposited on a previously annealed titania layer, it is actually growing on a crystal (a poly-crystal of course!) which almost matches its lattice constant. Therefore, we might expect the *as deposited* film to partially have a crystalline structure, even before the annealing process. Another difference that can be envisioned between the two films is the different annealing treatment received by the bottom layer. In one case, it is heated twice, the first time being a direct exposure to the vacuum. In the other one it is heated only once, and never exposed directly to a reducing atmosphere. For the aforementioned reasons, *sample A* is expected to show better overall electrical properties than *sample B*.

4.1.1 Characterization

The samples were characterized by SEM before and after the final annealing treatment, as shown in figure 4.2. The films appeared compact, as it is to be expected from 1 Pa films, but no sign of the interface was clearly visible.

Sample A was electrically characterized after depositing the TaTO layer, before annealing it for a second time: a small current could flow through the sample (0.1 mA, about two orders of magnitude lower than in optimized compact films). This is likely due to the film growth happening on a crystalline substrate, which promotes at least a partial crystallization of the film during the deposition. The low current value is due to the imperfect crystallinity of the TaTO film (see also the Raman spectra in figure 4.3). Moreover, it is unclear what share of the overall current flows into which layer, therefore electrical properties of the single layers, of course, could not be measured. Both samples were then characterized at the very end of the treatment, but again, the

Table 4.1: Electrical properties of TaTO on reduced titania bilayers. All values are referred to the 50 nm thick TaTO layer only, in the hypothesis that TaTO has a much greater conductivity than titania.

Sample	Resistivity (Ωcm)	Carrier density (cm^{-3})	Mobility ($cm^2V^{-1}s^{-1}$)
A	6.0×10^{-4}	1.2×10^{21}	8.3
B	1.0×10^{-3}	1.0×10^{21}	5.9

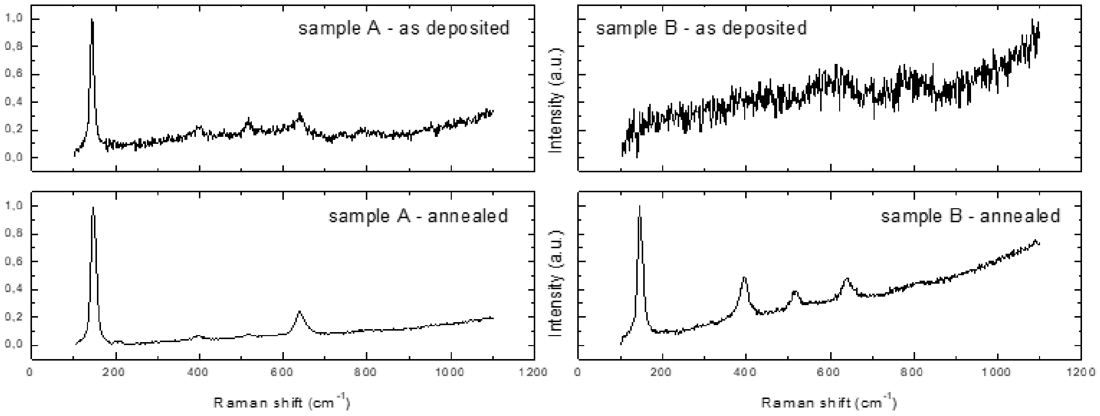

Figure 4.3: Raman spectra of bilayer sample whose bottom layer is made of reduced titania. Spectra were acquired before and after the final thermal treatment. The spectrum of Sample A has the lowest noise to signal ratio, indicating that it achieved a better crystallization.

real material properties could not be calculated because – after the final treatment – *both layers are conductive*: the only meaningful physical quantity that can be extracted from such measurements is the sheet resistance, which refers to the whole bilayered film (in both cases, 100 nm thick). *Sample A* had $R_{SH} = 120\ \Omega/\square$, while *sample B* had $R_{SH} = 209\ \Omega/\square$. Nevertheless, when performing the electrical characterization, some *effective values* for resistivity, carrier density and mobility were obtained for the TaTO film only, assuming that $\rho_{TaTO} \ll \rho_{TiO_2}$ (table 4.1). As expected, *sample A* proved to have better electrical properties compared to *sample B*.

Raman spectroscopy was performed to assess whether the various layers had crystallized or not. Figure 4.3 shows the samples' spectra before and after the final annealing cycle. The position and the width of the $E_g(1)$ peaks of anatase are reported in table 4.2.

The spectrum of *sample A* before the final treatment exhibits a peak at 144 cm^{-1} (the reference value for undoped titania) and a significant amount of noise, indicating a top layer of badly crystallized or amorphous TaTO. A significant change can be observed after

Table 4.2: $E_g(1)$ peak position and width.

Sample	Peak position (cm^{-1})	Peak width (cm^{-1})
A – before	144.1	10.4
A – after	147.4	14.2
B – after	146.5	14.9

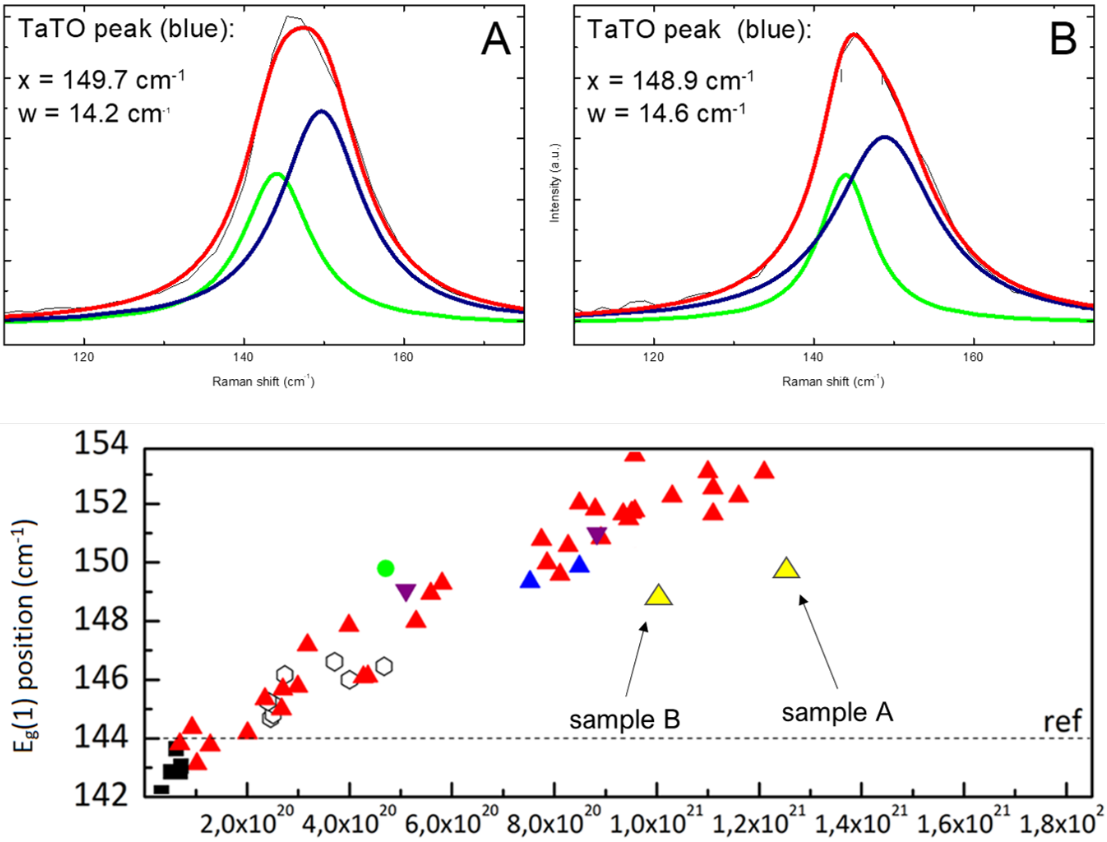

Figure 4.4: Top: TaTO peak deconvolution for titania-TaTO bilayers in which the bottom layer is made of reduced titania; the overall peak signal comes from reduced titania and TaTO. Titania substoichiometry is revealed from the weaker Raman signal (less crystalline order). Bottom: as calculated TaTO peaks are plotted against effective carrier density values [50], in the hypothesis that TaTO has a much greater conductivity than titania.

the annealing treatment. The noise basically disappears, and the $E_g(1)$ peak experiences a blueshift of 3.5 cm^{-1}.

If one believes that the doped and undoped layers remain essentially separate, then the contribution to this peak must come from two separate signals, one from titania, which is believed to be at around 144 cm^{-1}, and one from the TaTO top layer. By performing peak deconvolutions (figure 4.4) it was found that the TaTO peak lies at 149.7 cm^{-1} in the case of *sample A* and at 148.9 cm^{-1} in the case of *sample B*. It is interesting to observe that the titania signal is *weaker* than that of TaTO. This is due to the titania substoichiometry (less order, weaker peak) and to its *location* (buried below a TaTO layer). As it will be seen in section 4.2 and 4.3, stoichiometric titania has generally a stronger Raman signal than TaTO, even when buried beneath a thick TaTO layer.

The found values can be plotted against the *effective carrier* density (table 4.1) under the hypothesis that $\rho_{TaTO} \ll \rho_{TiO_2}$. There is a significant discordance (either a higher-than-expected carrier density or a lower-than-expected peak shift) from the predicted trend, which can be attributed to two reasons. One is the effect of the substrate: a lattice matching substrate, albeit polycristalline, probably reduces the stress states experienced by the TaTO lattice (which partially contribute to the peak blueshift). The other is the

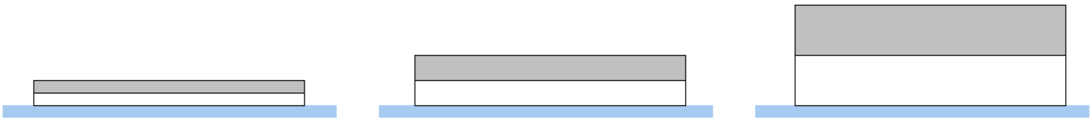

Figure 4.5: Deposition schemes for stoichiometric titania-TaTO bilayers. Overall thicknesses are 100, 200 and 400 nm, respectively.

fact that the assumption made regarding the two material's conductivity is not entirely justified. Indeed, they differ of about one order of magnitude. It is sufficient to have an estimate of the TaTO conductivity, but not enough to compare the latter to other samples' values.

4.2 TaTO on stoichiometric titania substrates

After the deposition of TaTO on reduced titania substrates, a different approach was taken: depositing TaTO on stoichiometric – and thus insulating – titania. Compared to the previous one, this approach allowed for a more complete electrical characterization of the samples which included intrinsic properties as well. Bottom layers were grown by PLD and later annealed at 500°C in air at 1 atm. This kind of thermal treatment has been shown to promote anatase formation, but to yield an electrically insulating material. This is due to the fact that in atmospheric conditions the anatase-to-rutile transition temperature is above 500°C; on the other hand, exposure to O_2 at such a temperature results in the neutralization of oxygen vacancies, which are responsible for conduction in undoped titania.

After depositing and annealing the bottom layers, top layers were deposited, with thicknesses matching those of the underlying titania film, as shown in figure 4.5. The bilayers were subsequently annealed according to the standard annealing process described in section 2.2. However, since the TaTO layer was grown over an anatase substrate, even the *as deposited* film could have – at least partially – a crystalline structure.

4.2.1 Characterization

The samples were characterized by SEM before and after the vacuum annealing, as shown in figure 4.6. In both cases, the films appear compact, coherently with what is expected for 1 Pa depositions. A difference in color between top and bottom layers can be observed when the TaTO layer is amorphous. This could be due to the different crystalline structure of titania (pure anatase) and TaTO (presumably an amorphous-anatase mixture). Conversely, the vacuum annealed samples show no visible marks, possibly due to the continuity in crystal structure.

Likewise SEM analyses, electrical characterization was performed before and after the vacuum annealing treatment. While annealed samples were expected and turned out to be conductive, the electrical characterization of the *as deposited* TaTO top layers gave mixed results. Only the 200 nm thick sample was successfully characterized, and exhibited a resistivity of $0.45\,\Omega$cm and unreliable Hall-figures. The other two samples ($50+50$ nm and $100+100$ nm) were too unstable, maybe due to an insufficient raw

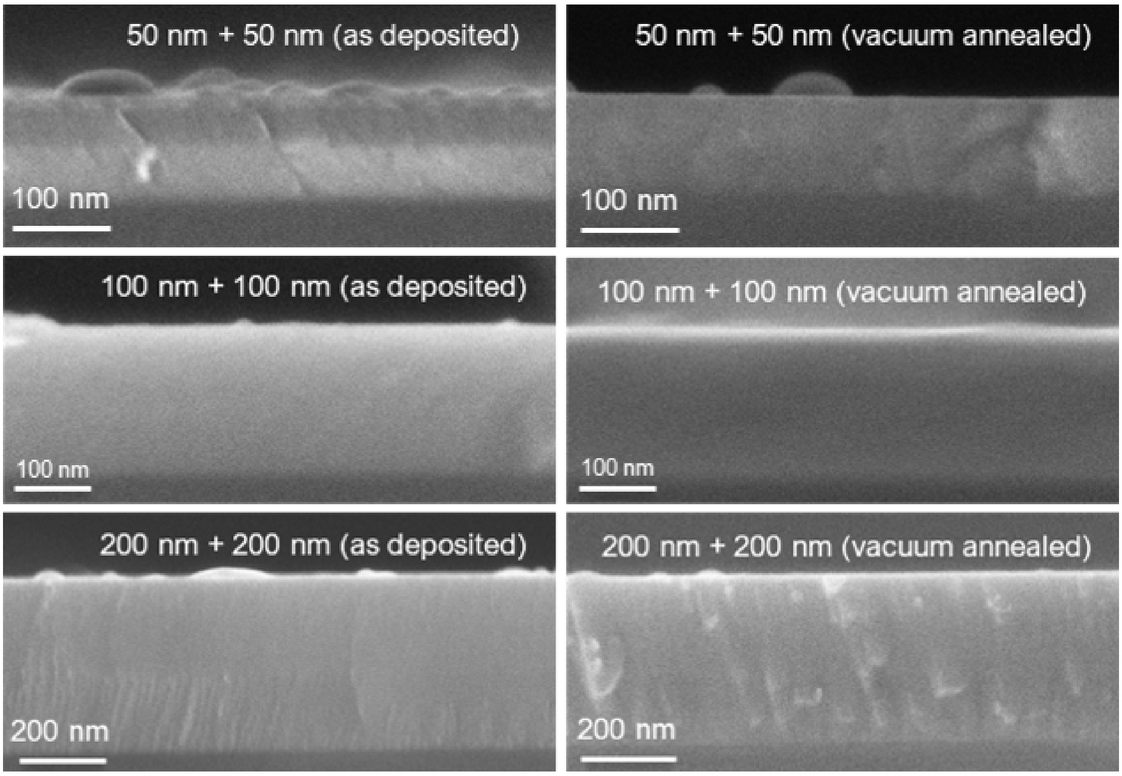

Figure 4.6: SEM images of the stoichiometric titania-TaTO bilayers. A greater difference is observed between air-annealed titania and amorphous TaTO, more than in vacuum annealed films.

amount of crystal fraction. The conductivity of the *as deposited* TaTO film is likely due to a partially successful crystallization into anatase, driven by the titania bottom layer. Annealed samples were conductive instead, as expected. Electrical properties are plotted against film thickness in figure 4.7. If compared to the those obtained with a mismatching substrate [54] these values belong to the same order of magnitude (figure 4.8). The $100+100$ nm sample exhibited the lowest resistivity ever achieved for TaTO under the employed deposition conditions. This one and the $200+200$ nm films were more conducting than their mismatched counterpart, while, oddly enough, the $50+50$ nm sample showed slightly worse electrical properties. This was initially ascribed to some mistake in the deposition process, but the reason for it will be clearer later after discussing ultrathin films in section 4.3.1.

Raman spectroscopy was performed to assess crystallization. Each sample was analyzed three times: after the titania bottom layer had been air-annealed, after the deposition of the TaTO top layer, and after the vacuum annealing treatment. Spectra are reported in figure 4.9. Nothing is clearly discernible other than the typical spectrum of anatase. However, it must be kept in mind that all spectra (except for the first column) are the result of two different contributions, coming from the two layers. In one case, it is pure anatase plus an amorphous or partially crystallized top, while in the second case it's two layers of anatase at different doping levels (thus, in principle, with different $E_g(1)$ peak position). By looking at the $50+50$ nm sample spectra, a lot of noise can be observed for the pre-annealed sample. Also, the spectra features a peak at ~ 790 cm^{-1}. A striking difference with the thicker samples can be observed. These samples show basically no noise, as if they had a much better crystal quality, driven solely by

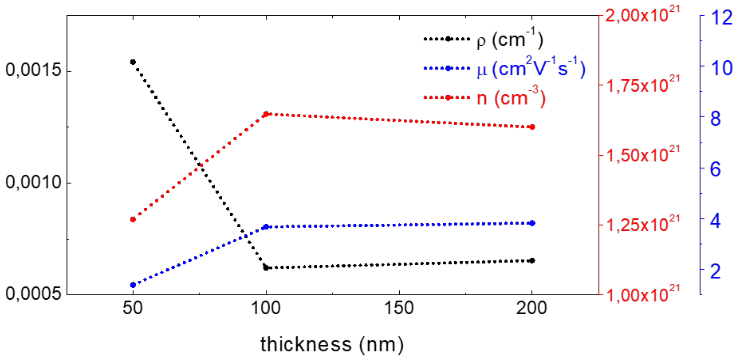

Figure 4.7: Electrical properties of annealed samples as a function of thickness. The reported thickness values refer to the TaTO layer only.

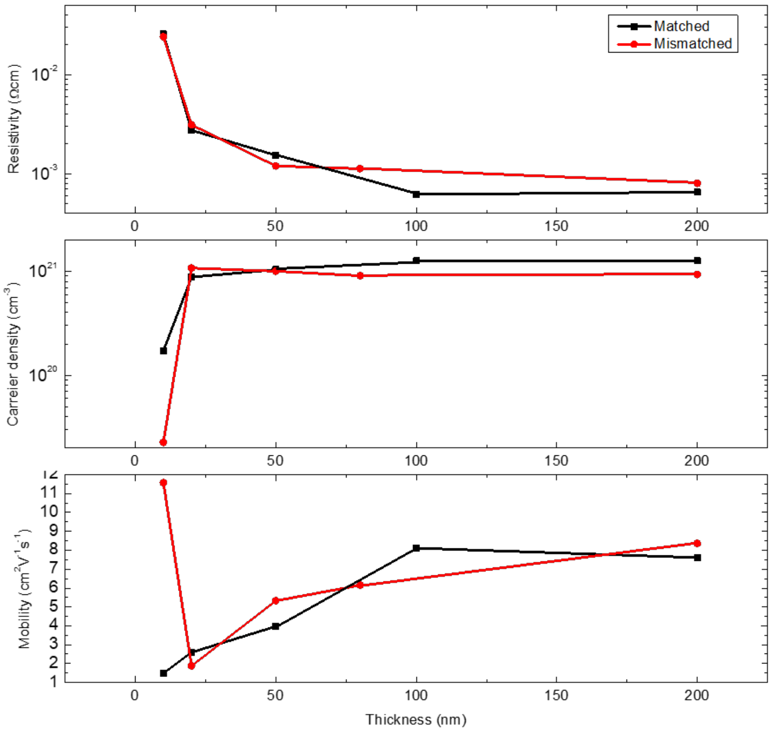

Figure 4.8: Electrical properties as a function of thickenss for lattice matched and mismatched films. Lattice mismatched values are taken from [54].

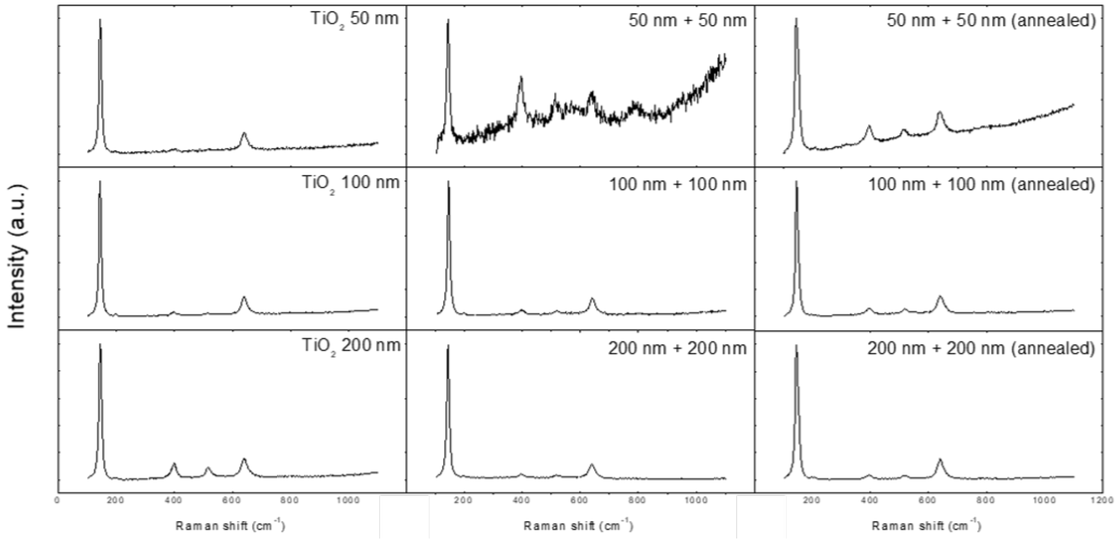

Figure 4.9: Raman spectra of stoichiometric titania-TaTO bilayers. Spectra were taken at different steps of film synthesis. Left column: after the air-anneling treatment of titania. Middle column: After the deposition of TaTO. Right column: after the vacuum annneling treatment.

the underlying titania layer. The noisy spectrum could be due to a completely absent crystallization of TaTO during growth-on-substrate.

After the vacuum annealing treatment all samples showed an improved crystallinity, as suggested by the reduced noise. Also, coherently with the increased carrier density, the $E_g(1)$ peaks experienced a blueshift. Since for each sample the total spectrum is the combination of two separate ones, a peak deconvolution (figure 4.10) based on the spectrum of the bottom layer can be made, in order to calculate the peak position for the TaTO film only. By looking at figure 4.10 it can be noticed that the titania peaks are more intense than the TaTO peaks, despite the titania layers being buried beneath the TaTO ones. This is due to the more ordered structure of stoichiometric titania. For a comparison, figure 4.4 shows the Raman signal of TaTO and substoichiometric titania. Once the peak positions are calculated, they can be plotted against the corresponding carrier density (figure 4.10). The samples fit into the trend, although not perfectly. It must be stressed that the peak positions used here were not directly measured, but calculated, and also that all measurements have a resolution of ~ 1 cm^{-1}, therefore some error is acceptable. However, it is easy to notice that all values are off the main trend in the same manner; they have either carrier density too high, or a peak shift too small. A parallel can be drawn with the case discussed in section 4.1 (even though in *this* case the measured resistivity value should be reliable). Lattice matched deposition could be able to reduce stress states allowing thus a slight redshift towards the 144 cm^{-1} nominal $E_g(1)$ peak position.

4.3 Ultrathin TaTO films

The air-annealed titania scheme was later used to attempt the deposition of films thinner than 50 nm. In particular, deposited films were 20, 10 and 5 nm thin. The investigation of ultrathin films has already been done [54], but using Si(100) and soda-

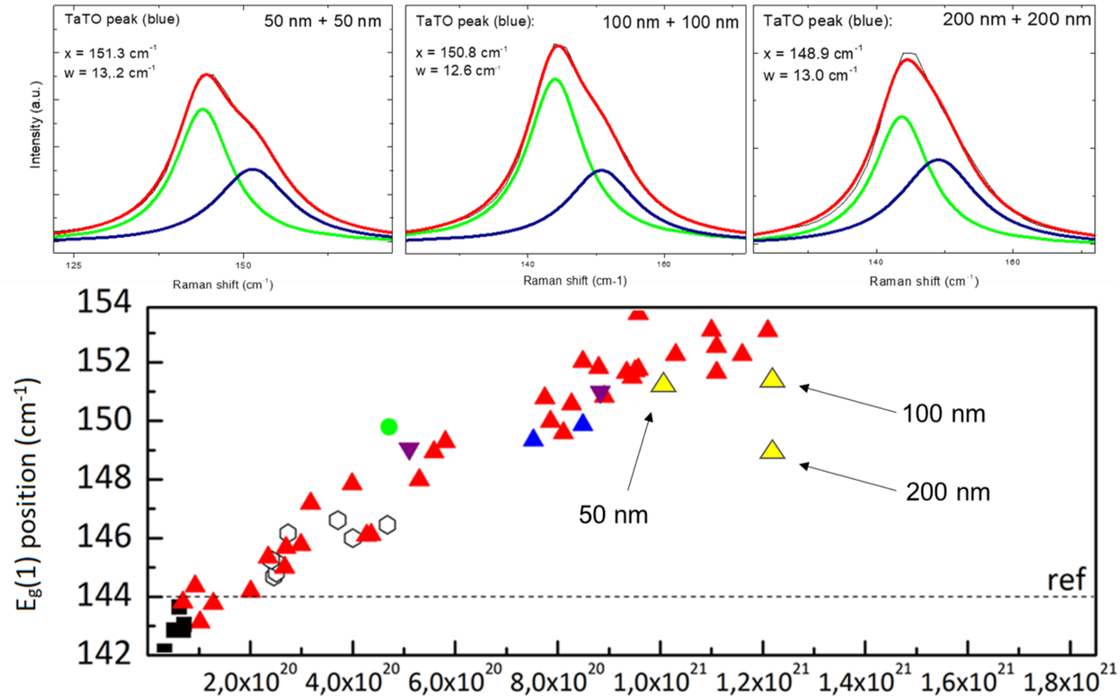

Figure 4.10: Deconvolution of $E_g(1)$ peaks for bilayers in which the bottom layer is made of stoichiometric (insulating) titania. The titania peak at 144 cm^{-1} is stronger than the TaTO peak, coherently with the higher crystalline order of stoichiometric titania.

lime glass substrates, rather than titania. The main issue concerning thin films is that, as thickness decreases, surface effects become more relevant, and conductivity decreases (see section 1.1.4). The cause for this is to be to be looked for in a decrease in mobility due to greater surface scattering of carriers, which statistically spend more time close to the interface [12] than than they would in a thick film. The presumed advantage of depositing on titania, rather than silicon or glass, is the fact that TaTO and titania have the same crystalline structure: the bottom layer could act as a lattice matching substrate to the top one [13]. This would reduce the effects of surface and grain boundary scattering and grant an overall higher surface mobility. Another feature of this deposition scheme, as already mentioned in the previous sections, is the possibility of having a partially crystalline film growth driven by the titania layer.

The samples were prepared in two steps. First, 50 nm thick titania bottom layers were deposited by PLD and later annealed in air at 500°C. Then, TaTO layers of varying thickness were deposited on top and vacuum annealed. The same observations made in section 4.2 are valid: the air-annealing treatment promotes anatase crystallization but hinders conductivity. As a result, it becomes possible to measure the electrical properties of TaTO without interference from the substrate.

4.3.1 Characterization

The samples were characterized by SEM before and after the vacuum annealing, as shown in figure 4.11. In both cases, the films appear compact, coherently with what is expected for 1 Pa depositions. A difference in color between top and bottom layers can be

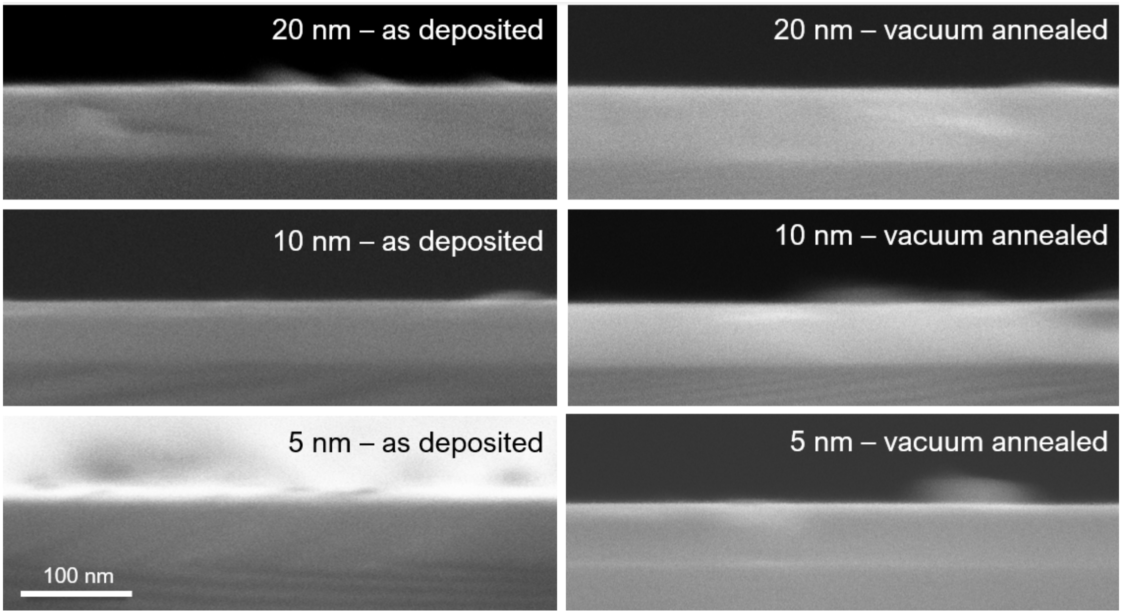

Figure 4.11: SEM images of ultrathin films, before and after a standard annealing treatment. Due to their very low thickness, TaTO layers are barely visible.

Table 4.3: Electrical properties of ultrathin TaTO films deposited on stoichiometric titania bilayers. The properties of the 50 nm thick TaTO film are reported for comparison.

Thickness	Resistivity (Ωcm)	Carrier density (cm^{-3})	Mobility ($cm^2V^{-1}s^{-1}$)
50 nm	1.5×10^{-3}	1.0×10^{21}	4.0
20 nm	2.8×10^{-3}	8.8×10^{20}	2.6
10 nm	2.6×10^{-2}	$\sim$	$\sim$
5 nm	–	–	–

observed when the TaTO layer is amorphous. This could be due to the different crystalline structure of titania (pure anatase) and TaTO (presumably an amorphous-anatase mixture). Conversely, the vacuum annealed samples shows no visible marks, possibly due to the continuity in crystal structure. As thickness decreases, it becomes more and more difficult to tell the difference between bottom and top layer.

Electrical characterization was also performed before and after the vacuum annealing treatment. *As deposited* films proved far too insulating to sustain a current, analogously to what is observed for samples discussed in 4.2.1. Vacuum annealed samples were characterized only to a certain extent: the 20 nm film allowed to measure all electrical properties with sufficient accuracy, the 10 nm film yielded a value for resistivity, but unreliable Hall-figures, and the 5 nm film proved too insulating to be measured. As expected, and coherently with previous works [54], a decrease in thickness is accompanied by a worsening in the electrical properties. Values are reported in table 4.3.

These values belong to the same order of magnitude as those of films deposited on Si(100) and soda-lime glass, suggesting that having a lattice-matching substrate does not improve the electrical properties of TaTO. A more detailed analysis can be done by plotting the sheet carrier density against the film thickness (values from 50 nm, 100 nm

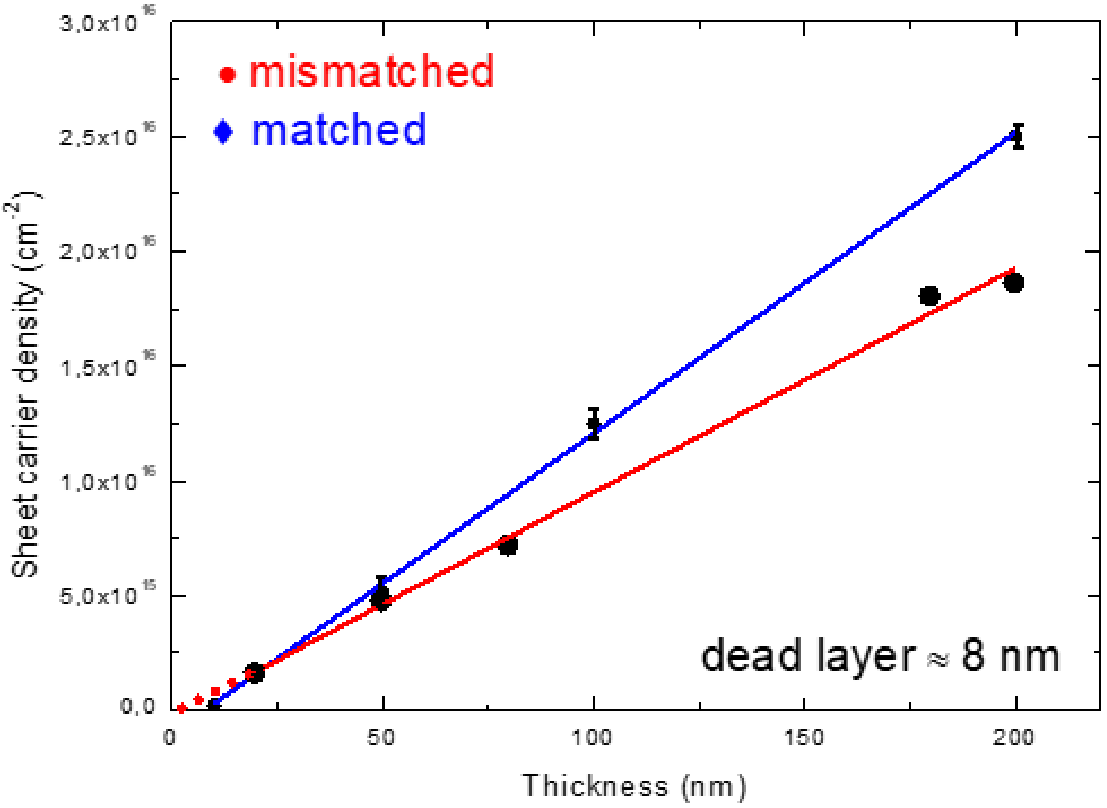

Figure 4.12: Look plot for TaTO deposited on lattice matched and mismatched substrates

and 200 nm films were used too). The resulting graph is a straight line (figure 4.12), which according to Look's model (section 1.1.4) intercepts the entity of the dead layer (if any) on the abscissa [12] . Conversely, the *slope* tells the value of the *bulk* carrier density. Both mismatching [54] and matching film properties were considered, and the results are remarkable. Having a titania substrate allows for a slightly higher bulk carrier density (greater slope), presumably due to improved crystalline structure, but also brings a dead layer of $\sim$ 8 nm, as opposed to the mismatched case, where the dead layer is about 2 nm. This means that having a lattice matching substrate is convenient, but not at low thicknesses! This result can be related to was observed by Look [13] when comparing the electrical properties of GZO deposited on ZnO versus GZO deposited on silicon. However, in that case, no dead layer was found when depositing on zinc oxide. The reason for this might be looked for in the different synthesis procedures used for GZO and TaTO. Depositing doped zinc oxide doesn't require a post-annealing treatment, as opposed to TaTO. A thermal treatment (especially if it has a significant dwell time) may promote the diffusion of tantalum into the undoped titania lattice and thus reduce the electrically conducting section. Another possibility is that the treatment activates the oxidation of the TaTO films, which is in contact with a stoichiometric titania lattce. Of course, the thinner a film is, the more it is affected by the presence of a dead layer. As an extreme case, the 5 nm film is even thinner than it, and is unable to bear any current. Conversely, glass or silicon substrate seem to hinder the formation of such dead layer. Further studies in this direction should be made to assess the role of surface oxidation or dopant diffusion into the bottom layer. For the latter hypothesis a possibility is making

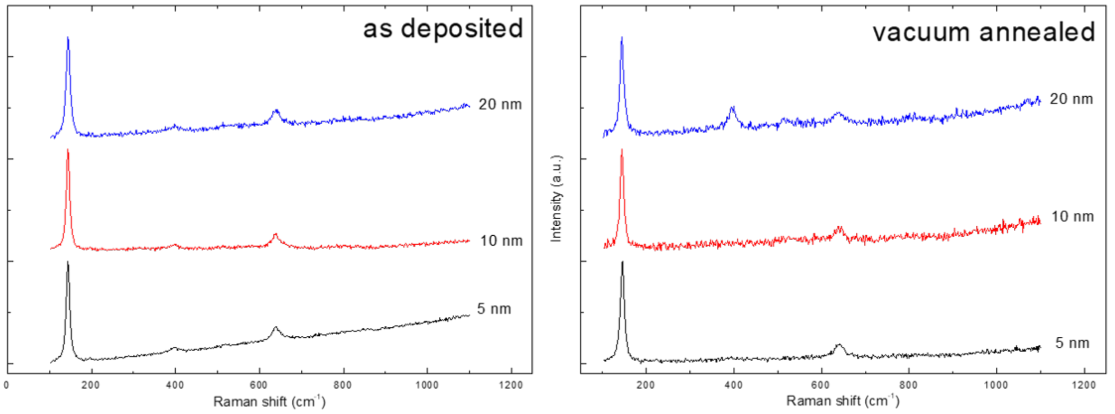

Figure 4.13: Raman spectra of ultrathin films, before and after the vacuum annealing. The most prominent feature is the $E_g(1)$ peak of anatase, in most cases due to the underlying titania substrate only.

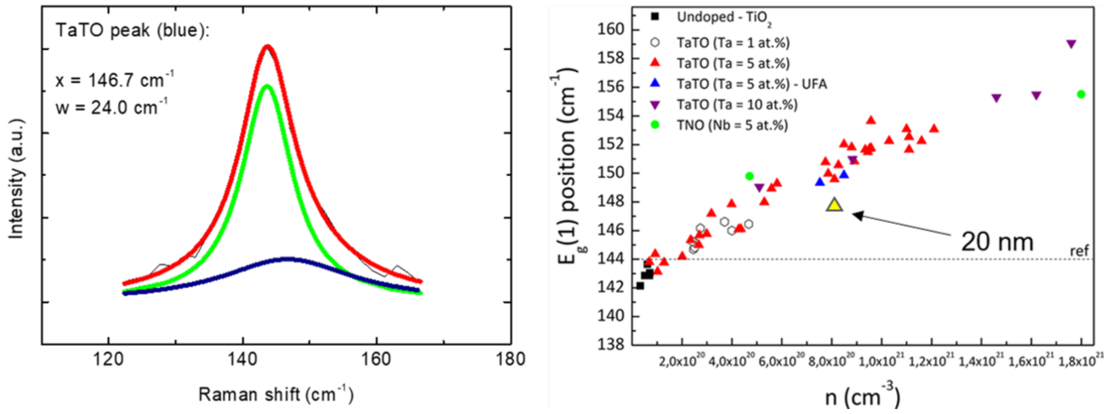

Figure 4.14: Left: peak deconvolution for a 20 nm film; the TaTO peak has a width much greater than commonly observed for TaTO. Right: the obtained value for TaTO is plotted against the carrier densit; the sample fits fairly well, considering all the criticalities concerning the peak values.

it out of air-annealed *TaTO*, rather than titania, in order to have a constant tantalum concentration throughout the whole film. Of course this this idea is not guaranteed to work since tantalum is not the only responsible for conduction.

Samples were Raman characterized before and after the vacuum annealing treatment (figure 4.13). The resulting spectra always have two contributions, coming from the two layers. While the bottom layer is definitely titania in the anatase form, it is not always clear whether the top layer should be considered amorphous or crystalline. In the case of *as deposited* samples, the TaTO layer is likely amorphous, as also suggested by the complete inability to conduct electricity. In the case of annealed samples, the TaTO layer is definitely crystalline in thicker films, while in the case of 10 and 5 nm films this is uncertain. To this respect, the Raman spectra do not help, since the titania signal is much stronger than anything else. A peak deconvolution (figure 4.14) of the $E_g(1)$ peaks was performed for the 20 nm thick sample, which is likely crystalline and has a carrier density value comparable to those of thicker films. The peak position is plotted against the carrier density. As it was the case for thicker samples, the 20 nm film lies a bit off the main distribution. This can be attributed to some imprecision in the peak acquisition and subsequent deconvolution, jointly the Raman measurements resolution, or – again – to the lattice match-induced redshift. Furthermore, the signal of the TaTO thin layers is weaker (see figures 4.4, 4.10) and the position of the $E_g(1)$ TaTO peak is strongly dependent – when calculated – on the imposed value for titania.

Summary Two deposition schemes were explored. TaTO was deposited on reduced (vacuum annealed) titania films and insulating (air-annealed) titania films. The second scheme was later employed in order to deposit ultrathin films, down to 5 nm in thickness. Depositing on reduced titania yielded conducting films, whose properties could not be measured, because of the substrate's nature. Depositing TaTO on insulating titania gave very interesting results. Compared to depositions on glass or silicon, better electrical properties were observed in the case of thick films, attributed to the better crystal quality driven by the titania lattice, and worse electrical properties in the case of thin films, attributed to dopant diffusion into the titania lattice an/or to TaTO oxidation. A dead layer of 8 nm was estimated, implying that films thinner than that cannot be conductive. While this strategy was not successful, a possibility could be to deposit conductive ultrathin films on top of air-annealed TaTO substrates, in order to verify whether changes arise. Another significant finding was that all TaTO films deposited on titania substrates seem to lie off the main carrier-peak distribution (fairly independently of the titania stoichiometry). This was attributed to a redshift related to lower stress states in the lattice.

Chapter 5

Advanced architectures

In this chapter the deposition schemes employed in the previous two chapters are combined, to create layered films whose parts are deposited at different pressure and thus exhibit different porosity and conductivity. For this reason they differ from the compact films discussed in chapter 4, but not just that: in fact, unlike compact titania-TaTO bilayers, they are made of TaTO only. However, since material properties differ significantly when the porosity changes, it is possible to create a TaTO-TaTO interface. This can be exploited to create multilayered compact films with alternating electrical properties, as discussed in section 5.2. Another possibility, discussed in section 5.1 consists in depositing a compact layer on top of a hierarchical nanoparticle assembly, which is thus "capped" by the top layer. Of course, many more schemes can be thought of. While not investigated in this work, it is possible in principle to have the various layers deposited in different background gases. Depositing a TaTO-only bilayer or multilayer has a great advantage from a practical point of view: a film with many layers can be deposited "all at once" without having to open the vacuum chamber (chapter 2). Indeed, it is sufficient to turn off the laser and change the in-chamber pressure (or background gas) by mass flow control. This is very convenient in PLD systems which can host only one target and could be extended to other vacuum coatings techniques in which pressure plays a role in determining film properties.

5.1 Capped TaTO nanoparticles

The idea of depositing a compact layer on top of a hierarchical structure has been studied by Gondoni [63] in the case of AZO. The aim of that work was to combine the compact layer's conductivity with the haze properties of the porous layer below. In the case of TaTO, the compact layer could have an additional role: protecting the nanoparticle assembly underneath from the highly reducing environment which the film experiences during the annealing treatment. This way it could be possible to achieve a better crystallization of the nanoparticles. The technical challenges in this deposition scheme are related to the ability or inability of the lower porous layer to sustain the formation of a more compact layer on top of itself. If the lower layer is too porous, it can be squeezed by the top one, which in turn will have an irregular topology (and poor percolation) due to the unstable substrate.

Three samples were deposited, as explained in table 5.1. *Sample A* and *sample B*

Table 5.1: Deposition specifics for capped nanoparticles. The reported deposition atomospheres refer to both layers. Since the 10 Pa porous layers were able to sustain a 3 Pa capping, a 1 Pa capping was later tested.

Sample	bottom layer pressure	top layer pressure	deposition atmosphere
A	10 Pa	3 Pa	$Ar : O_2 = 5 : 1$
B	10 Pa	3 Pa	O_2
C	10 Pa	1 Pa	O_2

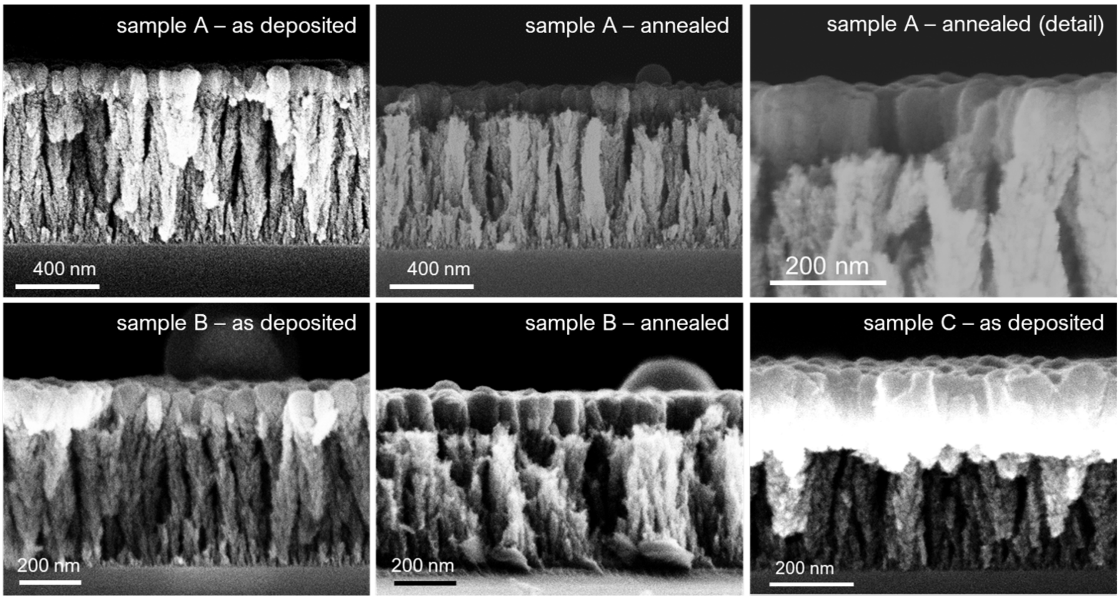

Figure 5.1: SEM images of capped nanoparticles. All samples show a well connected compact upper layer.

were annealed in a vacuum according to the standard annealing process (section 2.2), while *sample C* was not treated due to technical issues.

5.1.1 Characterization

The samples were characterized by SEM, and clear evidence of a bilayered film was observed. Figure 5.1 shows the overall structure and some details of such films. There is a sharp separation between the porous and compact parts. The latter appears well connected. This means that the chosen pressure values are compatible. Such a connected morphology should allow for the flow of some current. *Sample A* ($Ar{:}O_2$) was characterized after a standard annealing process and exhibited a resistivity of 9.7×10^{-3} Ωcm, a carrier density of 4.0×10^{20} and a mobility of 1.5 $cm^2V^{-1}s^{-1}$. *Sample B* (oxygen) had instead $\rho = 5.3 \times 10^{-2}$ Ωcm and unreliable Hall figures. These values (especially the resistivities and the mobility in the case of *sample A*) are comparable with those of films deposited on glass. This means that the films achieved a non-negligible percolation, despite the uneven deposition substrates.

The samples were characterized by Raman spectroscopy before the thermal treatment (an uninteresting amorphous band was observed and thus not reported) and afterwards.

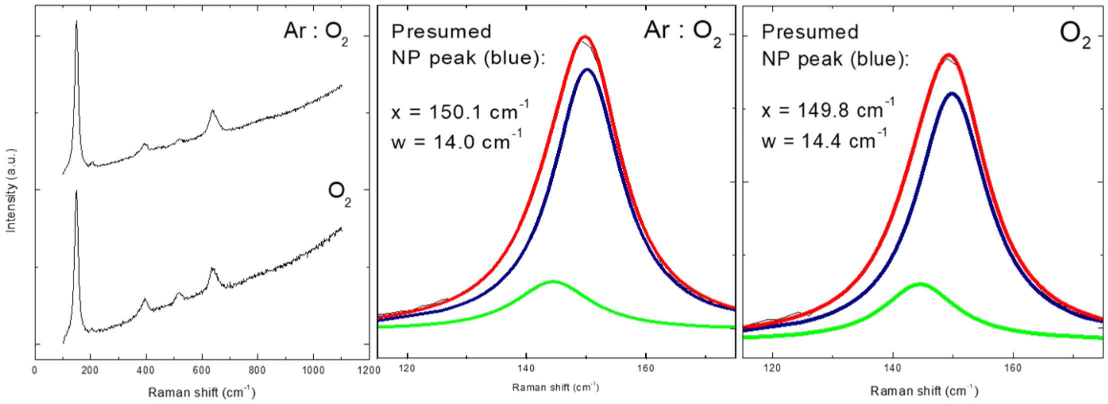

Figure 5.2: Left: Raman spectra of capped nanoparticle assemblies, deposited in Ar:O_2 and in pure oxygen. Center and right: Deconvolution of the $E_g(1)$ peak for both films.

The Raman spectra of the samples capped at 3 Pa are shown in figure 5.2. The usual anatase peaks are visible, meaning that *something* crystallized into this phase. Also, a photoluminescence background can be observed. At first glance, by keeping in mind what was discussed in the previous chapters, one might be tempted to interpret this result as coming from two well-distinguishable contributions: a reasonably crystalline compact layer and a porous layer damaged by the thermal treatment; in this scenario, the $E_g(1)$ peak would sit around 144 $\sim$ 145 cm^{-1}. In fact, the peak position in this case is about 149 cm^{-1} ! Some additional contribution must exist, other than that of the compact layer. The observed peaks can be deconvoluted by taking as a reference the peak positions for 3 Pa compact films deposited on glass substrates (respecticely, at 145 and 144 cm^{-1}). In both cases, the calculated peaks are much more intense than the reference compact layer peaks (indeed, if they had comparable intensity, they would appear as separate peaks). This is quite puzzling, since it would mean that the porous structures have a much greater Raman sensitivity than the compact layer above it. This would not be surprising *if the lower layers were compact* – they are very thick, and would naturally have a very strong signal. The calculated peak position is quite high, and if it were used to extrapolate a value for carrier density [51] it would yield about $n = 8 \times 10^{20}$ cm^{-3}. Other factors may play a role in the peak shift.

A study on the Raman spectrum of undoped titania nanoparticles produce by flame pyrolysis by Li Bassi *et al.* [61] has shown that nanoparticle size and oxygen substoichiometry can influence the position of the $E_g(1)$ peak. The maximum observed shift due to quantum confinement was of about 3 cm^{-1} (in the case of 5 nm nanoparticles), while the maximum shift due to oxygen substoichiometry was 5 cm^{-1}.

However, it is unclear what characteristic size should be attributed to the TaTO hierarchical structures. Plus, a parallel cannot be drawn between the two synthesis methods when it comes to judging the role of substoichiometry. An educated assumption could be to exclude the significance of the latter effect, since oxygen excess is what so far has hindered the successful doping of porous TaTO. If we assume that quantum-confinement-derived shifts don't exceed the aforementioned value, *something else* has to be responsible for the shift and this may be evidence for a successful doping of titania nanoparticles. Of course, the relative significance of these two/three effects cannot be determined with these pieces of data.

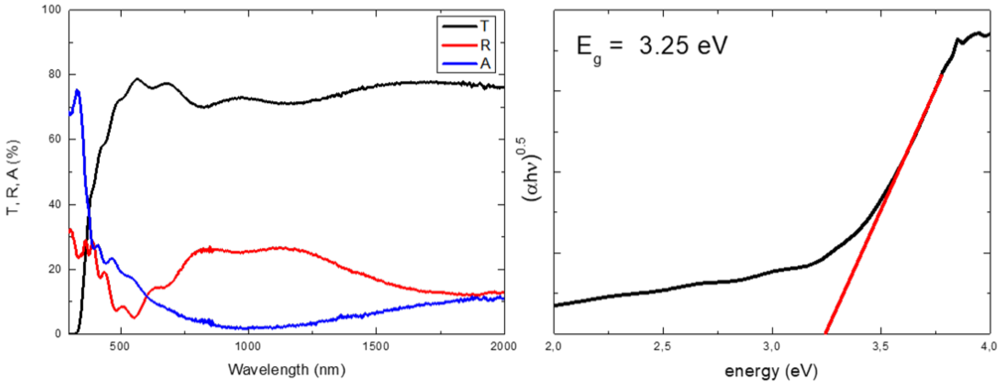

Figure 5.3: Optical properties of a capped nanoparticle film. On the left, a T-A-R spectrum is shown. The transmittance value, given by the compact layer, fits into a thickness-transmittance trend highlighted by previous works [54][51]. On the right, the optical bandgap is calculated by means of a Tauc plot.

The transmittance, absorbance and reflectance spectra of *sample A* is reported in figure 5.3. The 75% NIR transmittance is likely due to the compact 3 Pa layer and is in accordance with trends highlighted in past works [54][51]. An attempt was made at calculating the optical bandgap by means of a Tauc plot. The obtained value was 3.25 eV, slightly higher compared to undoped anatase. This could be due to the Moss-Burstein effect. However, it is not possible to tell whether the successful doping of titania concerns the compact layer or the porous one.

5.2 TaTO-only multilayers

The second deposition scheme presented here allows to deposit multilayered films. While all layers are made of TaTO, they are deposited at different pressures, and thus have different electrical behaviors. This allows to make films with alternating layers having different dielectric functions. This concept is at the base of hyberbolic metamaterials, as discussed in section 1.2.2.

While traditionally the layers of such materials have different chemical composition, in this case they are all made of TaTO, but with different morphology, stoichiometry and electrical properties. In particular, layers deposited at high deposition pressure will have a lower carrier density, to the point of behaving as a dielectric. This method allows to deposit multilayered films by PLD without opening the chamber, drastically reducing deposition times. At the same time, however, it is important to choose compatible pressure values for the deposition of adjacent layers, otherwise too porous structures might collapse when pressed by more compact ones.

Two film types were synthesized: one with alternating 1 Pa and 3 Pa layers (henceforth referred to as 3/1) and another one with alternating 1 Pa and 6 Pa layers (6/1). All films consisted of 10 layers in total $(5+5)$ and were deposited in a pure oxygen atmosphere. The deposition times were chosen in order to obtain equal-thickness layers (each being 50 nm thick). As it will be clearer later, doing so is not straightforward. All samples had their topmost layer being deposited at 1 Pa. Due to technical reasons, it was possible to thermally treat only one sample.

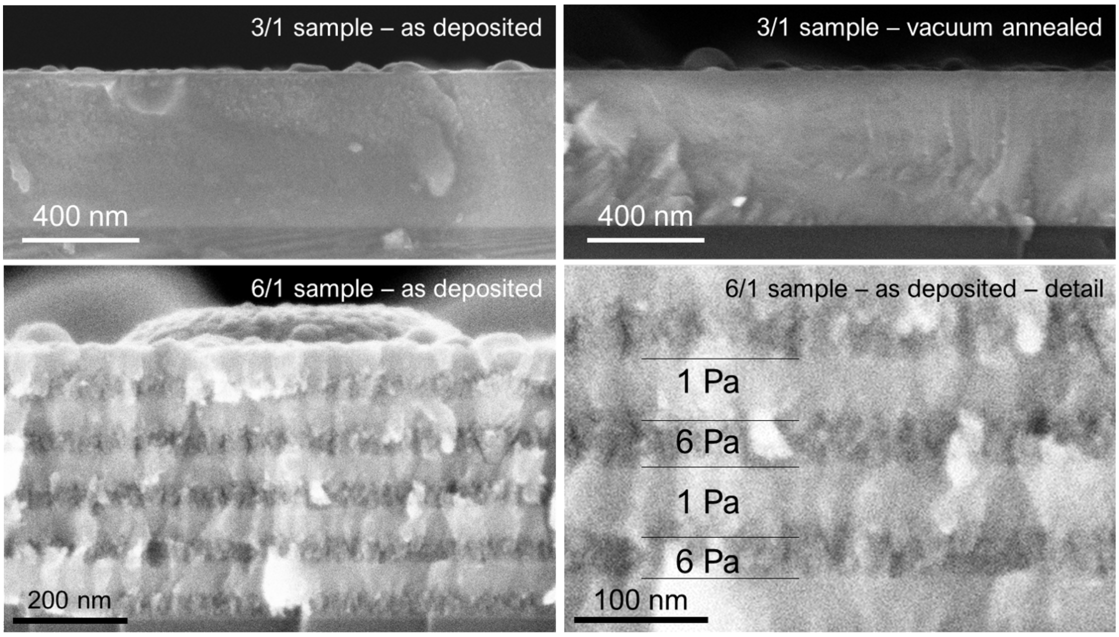

Figure 5.4: SEM images of TaTO-only multilayers; thickness 500 nm. Top left: as deposited 3/1 multilayer. Top right: vacuum annealed 3/1 multilayer. Bottom: as deposited 6/1 multilayer and detail; thickness 500 nm.

5.2.1 Characterization

A striking difference between the 3/1 and the 6/1 films can be observed when the films are characterized by SEM. The former looks completely uniform, and no sign of layer alternation is visible. This is due to the fact that both 3 Pa and 1 Pa atmospheres yield compact morphologies. Things change when a greater pressure divide is employed. A deposition background of 6 Pa is enough to promote columnar growth, therefore a difference is easily observable between the various layers, which appear clearly distinguishable. It is interesting to notice that 6 Pa layers are thinner than 1 Pa layers. This can be attributed to a squeezing-effect which every compact film deposition round exerts on the porous substrate, or to some penetration of the former into the latter. It means that 1) the electrical properties of *squeezed* films are different that those of their standalone counterparts and 2) deposition times have to be adjusted by trial and error in order to obtain equally thick layers. The thermal treatment does not seem to change the morphology, but allows for the film to be conductive.

Four point probe characterization of the 3/1 sample gave the following values

$$\rho = 8.4 \times 10^{-4}\ \Omega\text{cm}$$

$$n = 9.6 \times 10^{20}\ \text{cm}^{-3}$$

$$\mu = 7.5\ \ \text{cm}^2\text{V}^{-1}\text{s}^{-1}$$

which are to be interpreted as effective values. Strictly speaking, the only physical value that was measured was the sheet resistance ($16.1\,\Omega/\square$), but it is also meaningful to treat the multilayer as a material of its own – a *metamaterial* – with intensive physical properties.

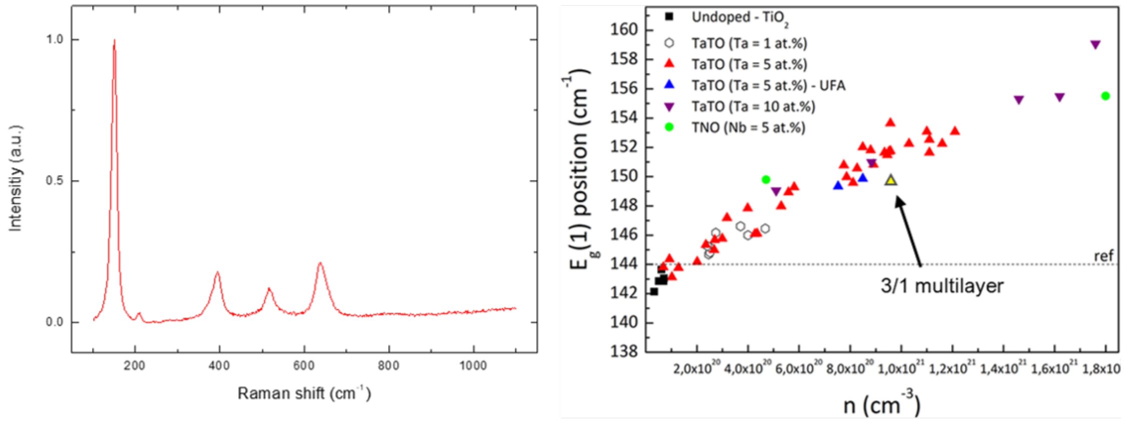

Figure 5.5: Raman spectra of a multilayered film and its correlation with the effective carrier density.

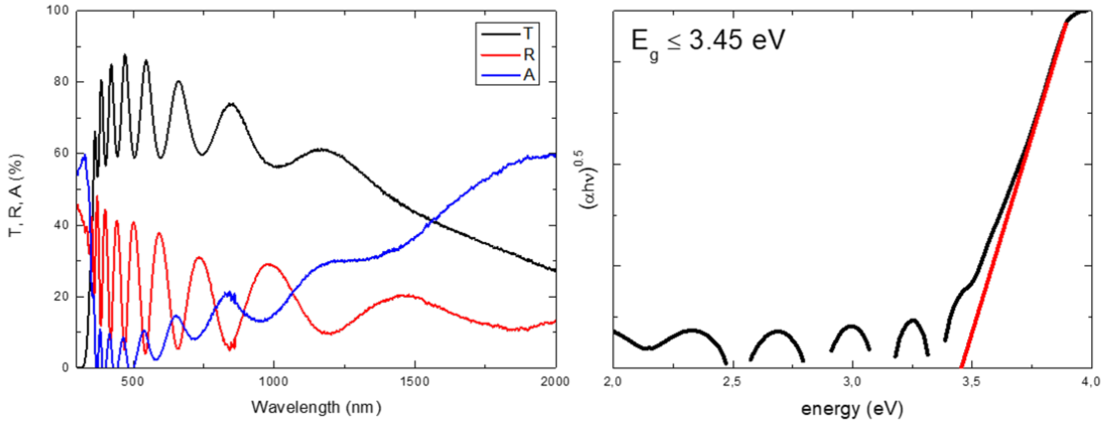

Figure 5.6: Optical properties of a TaTO-only multilayer. Left: T-A-R spectra of multilayer. Right: Tauc plot for a multilayered film.

The 3/1 film was Raman characterized (figure 5.5.a) and showed an $E_g(1)$ peak at 149.8 cm^{-1} (width = 15.45 cm^{-1}). A peak deconvolution for this spectrum was not performed due the difficulties in discerning among the various contributions, jointly to the impossibility of extracting real conductivity values for each layer. However, the film is considered *as one material*, the position of the overall $E_g(1)$ peak can be plotted against the *effective carrier density* (figure 5.5.b).

Finally, the optical properties are reported in figure 5.6. A strong interference pattern is observed in the transmittance and reflectance curves, because of the significant film thickness (500 nm) . A strong absorption can be seen in the NIR region. Tauc plots calculations were performed as well, but the linear region was short and and allowed for a poor fitting (and many possible bandgap values!) However, all of them were in the range $3.30 \sim 3.45$ eV, which are sensible values since they sit between the expected values of bandgap expected for the 3 Pa and 1 Pa layers considered singularly. The shift from the bandgap value of undoped titania is obviously due to the Moss-Burstein effect. This bandgap can be interpreted as an effective value, coming from the various contributions, or as the actual bandgap *of the metamaterial*.

Summary. TaTO-only bilayers and multilayers with different properties were deposited. Two main scheme were explored: capped nanoparticle assemblies and multilayered film at alternating deposition pressures. Both film types possess a significant technological advantage, and were deposited simply by changing the in-chamber pressure, without breaking the vacuum. Nanoparticles capped by a compact layer showed an intense Raman signal at 150 cm^{-1}, which may be due to a successful doping by substitutional tantalum. This could be a great leap forward in the quest for depositing TaTO nanostructures with a high carrier density. Structurally speaking, it was observed that a 10 Pa porous layer can sustain a compact 1 Pa film. Multilayered films were successfully deposited, but a full characterization of their dielectric properties was not possible. Structurally, it was found that 6 Pa depositions are compatible with 1 Pa ones.

The results of this last chapter are particularly promising. In the case of capped nanoparticles we may have found a winning strategy in order to make TaTO nanostructures for NIR plasmonics. More analyses should be done, in order to better understand what is the cause of the 150 cm^{-1} peak. The samples could be annealed in air, to check the effect of the annealing atmosphere; the TaTO capping could be mechanically removed (assuming it being possible), to exclude any Raman signal from it; an AZO capping may be used instead (but in this case, vacuum breaking may be necessary). There are many possibilities. As far as multilayered films are concerned, more pressure combinations should be explored in order to assess their compatibility, and deposition times should be adjusted for equal layer thickness. The dielectric properties of the individual layers should be studied by ellipsometric analyses, and the refractive properties of the metamaterial [33] should be investigated.

Conclusions and perspectives

This thesis work investigated the properties of thin films of tantalum doped titanium oxide (TaTO), deposited by the pulsed laser deposition method (PLD), in the light of future applications in the field of plasmonics. Both synthesis and characterization were performed. Since TCOs tend to have a plasma frequency in the near or mid infrared, and no instrumental setup at our disposal allowed to reach this frequency range, this work focused on studying the films' morphology, their electrical properties (resistivity, carrier density, mobility), their crystalline structure, and their optical properties at $\lambda < \lambda_P$. These properties were tuned by acting on some of the many deposition parameters: in-chamber pressure, gas composition, and deposition time.

The synthesis of TaTO nanoporous films and nanoparticles was performed by depositing at pressures higher than those needed to get compact films. The range spanning from 4 Pa to 15 Pa was explored. While some control samples were deposited in pure oxygen, the main deposition atmosphere used was a mixture of argon and oxygen in a 5 to 1 ratio. The reason for using this mixture stemmed from the fact that while it is necessary to increase pressure to promote nanoparticle growth, this inevitably leads to an excessive amount of oxygen in the chamber, which hinders TaTO substoichiometry. Hence the idea of depositing in a mixed atmosphere of argon and oxygen, to make it possible to increase the pressure while keeping the oxygen partial pressure low. In addition to this variation in the *deposition* some modifications to the post-annealing treatment were made. After a preliminary study on compact films, it was chosen to study the effect of an *ultrafast annealing process*, to assess whether the annealing treatment had any influence on the films properties. Standardly annealed films were compared to fast annealed ones. Unfortunately, these procedures did not make possible to synthesized nanoparticle assemblies with high carrier density. Optical measurements and subsequent bandgap calculations revealed a weak or negligible Moss-Burstein shift, pointing to an unsuccessful doping efficiency for the nanoparticles. Raman analyses highlighted the presence of a high amorphous fraction in the nanoparticles as well as a co-presence of rutile and anatase. No significant difference was observed between standard and ultrafast annealing cycles, except for a possible tendency to promote rutile growth with the ultrafast process. To summarize, this approach did not lead to the expected results. One of the causes might reside in an incorrect mixture for the deposition atmosphere. It is likely that for every deposition pressure, there exists an *optimal gas ratio*, and in order to verify this, one should deposit TaTO according to different combinations to assess whether differences arise.

The synthesis of titania-TaTO interfaces was performed by successive deposition of compact layers (1 Pa) of titania and TaTO by PLD, using different targets. While the possibility of sustaining SPPs was not explored, bilayered configurations of different thickness were investigated, and characterized electrically and by Raman spectroscopy. TaTO was deposited on both substoichiometric and stoichiometric titania substrates, vacuum and characterized by four point probe analysis, SEM and Raman spectroscopy. All samples correctly crystallized into anatase, and the position of the $\mathrm{E}_g(1)$ peak of anatase was correlated with the measured carrier density of the films. Since both the titania substrates and the overlying TaTO layer had anatase spectra, a peak deconvolution was necessary to isolate the TaTO signal from that of the underlying titania. A slight deviation from the expected trend was observed and attributed to the different substrate used for the deposition of TaTO. The use of a lattice matching substrate could reduce the stress state experienced by the grains, a factor that is known to contribute to the main peak's blueshift. Thick films (200 and 100 nm) deposited on titania substrates showed slightly improved electrical properties, likely thanks to an improved crystallinity. The next steps in the study of bilayers should be the dielectric characterization of the various materials employed (through ellipsometric analyses) to assess from a theoretical point of view whether they satisfy all conditions to sustain SPPs, with the ultimate goal of activating and observing such excitations in ad-hoc fabricated structures.

The study of bilayered configurations made of stoichiometric (thus insulating titania) and TaTO was used as a starting point to achieve the synthesis of ultrathin conducting films, which is necessary in the perspective of creating plasmon-equivalents of integrated circuits. TaTO layers having thickness of 20 nm, 10 nm and 5 nm were deposited on insulating titania layers, vacuum annealed, and characterized electrically: unexpectedly, the films exhibited worse electrical properties that those of films of equal thickness deposited on glass! This was attributed to the presence of a dead layer. By comparing sheet carrier density values for all films deposited on titania (even the thick ones) the dead layer was estimated to be 8 nm thick. This meant that the 5 nm film was not conductive at all. Deposition on titania is thus convenient for thick films (the improved crystallinity offsets the presence of a dead layer), and vice versa detrimental for thin films. Two hypotheses were made to justify the presence of such layer: the diffusion of dopant into the titania lattice and the oxidation of TaTO when in contact with stoichiometric titania at high temperatures. In order to assess whether any of the two hypothesis is true, two things can be made, respectively. TaTO should be deposited either on air annealed (insulating) TaTO, to assess the role of tantalum diffusion, or on vacuum annealed (reduced) titania, to check whether oxidation plays a part.

In the last part of this thesis work new ideas were explored. A strategy to deposit nanoparticles was devised, and a study of multilayer was started. The common feature of the last topic covered by this thesis work is the fact that all investigated architectures only use TaTO, albeit deposited at different pressures, in order to create interfaces between electrically different layers. This was very convenient from a technological point of view since it allowed us to deposit many different layers without having to open the vacuum chamber. The first idea that was explored using this setup is that of *capped nanoparticles* in which a hierarchical nanoparticle assembly is covered by a compact layer, which acts a protecting layer towards the outer environment (in particular, the reducing character of a vacuum coupled to high temperatures). Samples were deposited and vacuum annealed. Raman characterization of these samples showed an unexpected anatase peak at 149 cm^{-1} (a shift of about 5 cm^{-1} from the expected position) which *could* be due to a successful doping and anatase crystallization of TaTO nanoparticle. Further investigation is obviously needed, since other factors other than the presence of substitutional tantalum may contribute to the peak blueshift. Possible developments for this study include: a variation of the thickness of the porous and compact layers; a mechanical removal of the upper layer, after the vacuum annealing; using a different material for the capping layer (although this would require opening the deposition chamber).

Another TaTO-only architecture that was explored was that of multilayered structures made of alternating compact and porous layers, which would – once thermally treated - act as dielectric and conductive layers respectively. This could be one route to synthesize TaTO-based hyperbolic metamaterials. This topic was just scrapped on the surface by the thesis work: the structural compatibility of different pressure ranges was assessed, but the behavior of the metamaterial was not investigated. Further work to be done includes a wider analysis of the pressure ranges that can be used to deposit such structures without having them collapse, the electrical characterization of single compact layers, the measurement of the dielectric constants and finally more sophisticated negative refraction experiments, once their feasibility is proven.

The entirety of this work was focused on the properties of TaTO, in particular on those which could hint at the presence of a plasma frequency in the NIR range. The next step should be to assess directly the presence of such behavior. For example, optical characterization in the NIR and MIR ranges should be performed. A strong absorption peak around 4000 nm would be a good indicator of a plasma frequency in this region.

Finally, in a long-term view, if TaTO is shown to be a good candidate for NIR plasmonic applications, it will be necessary to design devices which incorporate it and consequently devise scalable synthesis techniques that can be easily integrated into the common microfabrication processes.

Appendix

A brief outline of the concepts of plasma, plasma frequency and plasmonic excitations, with a focus on surface plasmon polaritions, is reported here. This appendix (pictures included) can be considered an extreme condensate of the first three chapters of Stefan A. Maier's *Plasmonics: Fundamentals and Applications*, to which the interested reader can refer to for futher insights. A thorough discussion of the physical principles at the bases of plasmonics and its possible applications is not needed to understand this thesis work, however a basic knowledge of the topic can help frame the goals, the achievements and the open issues regarding this research field.

What is a plasma?

A possible definition of plasma is *a population of charged particles, whose kinetic energy is greater than their potential energy*. This definitions applies not just to plasmas in a strict sense (astronomical or thermonuclear) but also to the behavior of delocalized electrons in condensed matter. The most obvious example can be found in metals: while ions are orderly arranged into crystalline structures, electrons move freely, only slightly interacting with the lattice. Nevertheless, their motion is regulated by the weak lattice potential. The Coulomb force exerted by the ions is never enough to trap them into bound states. Instead, the system *oscillates* with a characteristic frequency, known as *plasma frequency*, given by

$$\omega_P = \left(\frac{ne^2}{m^*\varepsilon}\right)^{1/2} \tag{5.1}$$

where n is the electron number density, m^* is the electron effective mass and ε is the dielectric constant of the medium ($\varepsilon = \varepsilon_\circ \varepsilon_R$). It is important to understand that this frequency does not refer to a single electron, but to the whole plasma instead, which behaves as if it were a single entity, featuring collective modes called *plamsa oscillations*. The plasma frequency for a metal, which has $n \approx 10^{22}$ cm^{-3}, is of the order of 10^{16} Hz.

The simplest description that can be made of a plasma is the so called *cold plasma model*, which assumes immobile lattice ions and negligible interaction between electrons. This approximation is true if the oscillation timescale is much smaller than the average time between collisions. When electromagnetic radiation with frequency ω interacts with a plasma, a separate description of the two systems often cannot be given. This is certainly true when

$$\omega \approx \omega_P \tag{5.2}$$

The dispersion relation for electromagnetic radiation propagating in a cold plasma is shown in figure 5.7.

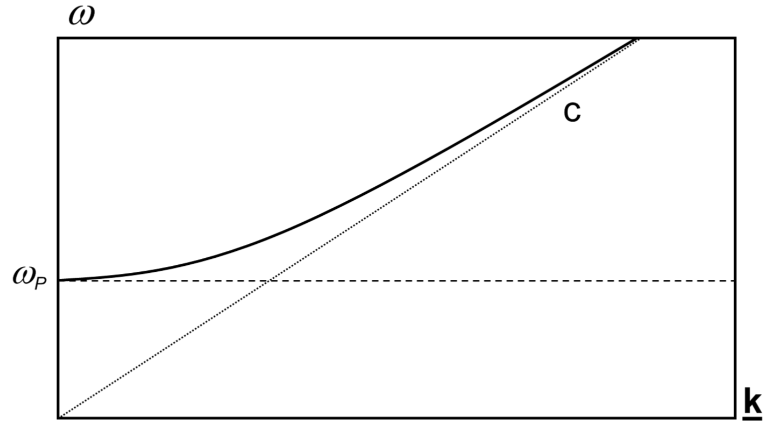

Figure 5.7: Dispersion relation for electromagnetic radiation in a cold plasma. The plasma frequency serves as a cutoff frequency for the propagation of light. At very high frequencies, the plasma is transparent to radiation and can be approximated as a vacuum.

For $\omega \gg \omega_P$ a plasma will be transparent to radiation: we can imagine the electromagnetic field as propagating through a static dipole assembly (don't forget the ions!). As an example, this happens when hard x-rays penetrate through metals. We call this phenomenon *transmission*. For $\omega \approx \omega_P$ a strong interaction between the radiation and the plasma is observed. In the case of metals, this happens in the UV range. It's called *absorption*. From the graph it is not obvious to understand what happens for $\omega < \omega_P$, other than that ω_P serves as a cutoff frequency for light propagation (no mode exists). However, experience tells us that metals *reflect* light in the visible range. From this comparison we can observe how metals act as dielectric when ω is high (in the limit of a perfect dielectric – the vacuum) and as...metals when ω is low. No material is truly a dielectric or a conductor: it all depends on the timescale of the applied electric field. Indeed, the ideas of conductivity (σ) and the permittivity (ε) are two faces of the same coin. If we assume a Drude conductivity

$$\sigma = \frac{ne^2\tau}{m^*} \tag{5.3}$$

where τ is the average time between collisions (relaxation time), then

$$\varepsilon_R = 1 + \frac{i\sigma}{\varepsilon_\circ} \tag{5.4}$$

The relative permittivity (also called *dielectric function*) can be expressed also as

$$\varepsilon(\omega) = 1 - \frac{\omega_P^2}{\omega^2 + i\gamma\omega} \tag{5.5}$$

and so related to the plasma frequency. The damping parameter γ is the inverse of the relaxation time τ. From here we can clearly see that a material approaches a pure dielectric behavior when the electromagnetic field frequency is much greater than the plasma frequency.

Plasmonic excitations

Plasma oscillations can be given a quantum description. The electron density oscillating field can be quantized into *bulk plasmons*, having energy equal to $\hbar\omega_P$. Because of the axial nature of the electric interaction, bulk plasmons have a *longitudinal* character. Therefore, they cannot be *excited* by photons, which are transverse in nature. One should not confuse the intensification of light absorption around the plasma frequency with the possibility of exciting said quanta of oscillation. Absorption is strong around ω_P because at this (resonant!) frequency the interaction between photons and conduction electrons is maximized. Bulk plasmons can be excited (i.e. their energy can be increased of a multiple of $\hbar\omega$) by charged particle impact – for example. However, there are other plasmonic excitations, beside the bulk plasmon. *Surface plasmons* are particular excitations which usually exist at the interface between a metal and a dielectric. The two main embodiments of this excitations are the *surface plasmon polariton* (SPP) and the *localized surface plasmon resonance* (LSPR). The former (which will be discussed more in detail later) is a propagating mode able to travel along a metal-dielectric interface. The latter is a quasi-static electron resonance, usually found on simlar interfaces, but with a *finite* area: the most common example are metal nanoparticles. According to the simplest model that can be envisioned to describe a LSPR, the resonant frequency of such system is given by

$$\omega_{LSPR} = \frac{\omega_P}{\sqrt{1+2\varepsilon_m}} \tag{5.6}$$

where ω_P is the metal plasma frequency and ε_m is the dielectric constant of the surrounding medium. Localized surface plasmons are able to produce a strong local amplification of the electric field. This can be exploited in various applications, such as *surface enhanced Raman spectroscopy* (SERS), hot-electron based solar cells and cancer treatment.

Surface plasmon polaritons

Since a great part of this thesis work revolves around the synthesis of TCO-dielectric interfaces, which may be able to sustain SPPs, this plasmonic excitation will be discussed more in detail. Surface plasmon polaritons are traveling excitations that exist at the interface between a metal and a dielectric (and hopefully, between a TCO and a dielectric as well!). From their very name it can be understood that both electron oscillations in the metal (the plasmon) and electromagnetic waves in the dielectric (the polariton) are involved. The excitation is spatially confined at the interface and takes the form of an evanescent wave in the direction perpendicular to it (figure 5.8).

The properties of SPPs can be understood by calculating the values of the electric and magnetic fields with Maxwell's equations. Two significant results emerge.

- SPPs have a transverse magnetic (TM) polarization, i.e. the magnetic field always lies parallel to the metal-dielectric interface;

- conditions are set on the two materials' dielectric constants in order for the mode being a propagating one;

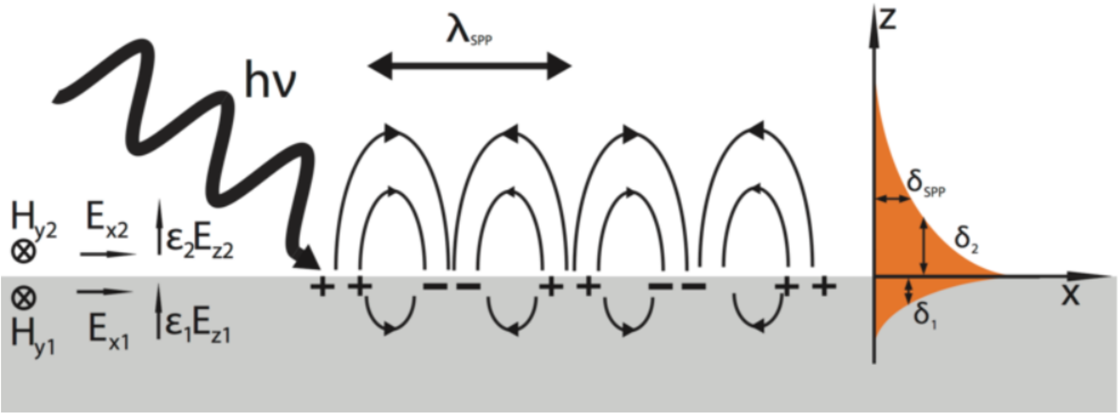

Figure 5.8: Representation of a surface plasmon polariton. The excitation propagates along the surface and is spatially confined in the form of an evanescent wave.

In particular the in-plane propagation wavevector, given by

$$\mathbf{k} = \frac{\omega}{c}\sqrt{\frac{\varepsilon_{metal}\varepsilon_{dielectric}}{\varepsilon_{metal}+\varepsilon_{dielectric}}} \tag{5.7}$$

must be real. This sets quite tight conditions on the material properties. Since one is a metal ($\varepsilon < 0$) and one is a dielectric ($\varepsilon > 0$), the sum of the two epsilons must be negative. This approach is valid in the hypothesis of an undamped electron gas (we therefore assume that $\varepsilon_{dielectric}$ and ε_{metal} are entirely real). The dispersion relation for such system is shown in 5.9. The frequency of SPP modes is asymptotically limited to

$$\omega_{SP} = \frac{\omega_P}{\sqrt{1+\varepsilon_{dielectric}}} \tag{5.8}$$

which simplifies to approximately

$$\omega_{SP} = \frac{\omega_P}{\sqrt{2}} \tag{5.9}$$

when the considered dielectric is air.

A similar reckoning can be made in the case of nonzero damping term. Without digging into details, it just needs to be understood that the same condition that was set on the real dielectric functions must be set to their imaginary parts as well. The corresponding dispersion relation is shown in figure 5.10.

Surface plasmon polaritons can be excited by different methods. These include prism coupling, grating coupling, near-field excitation and excitation by highly focused optical beams. A brief description of prism coupling techniques, the first ones to be developed and possibly the easiest to understand, follows.

Prism coupling relies on attenuated total internal reflection. It involves the excitation of the SPPs by the evanescent electro-magnetic field that is formed at the interface between a material with a higher epsilon and another material with a lower one. There are two configurations that can be adopted, as shown in 5.11. The Kretschmann configuration requires the deposition of thin metallic films on top of a dielectric prism, while the Otto configuration can be used on thick films or bulk metals. It is important to notice that

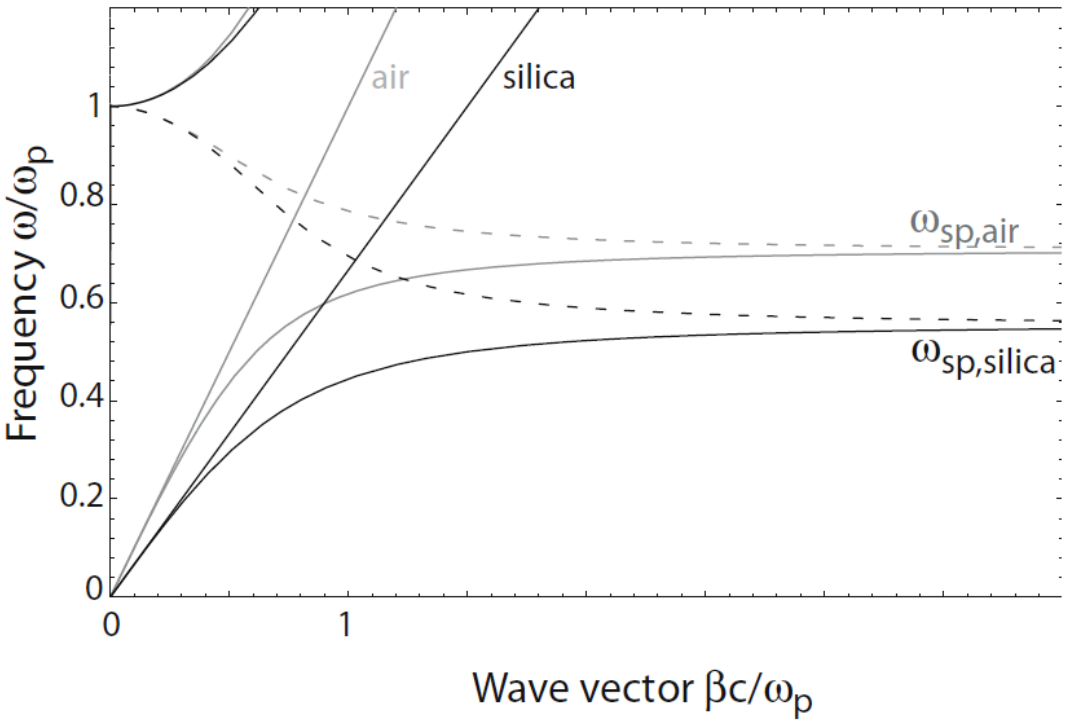

Figure 5.9: Dispersion relation for SPPs in the case of undamped electron gas. The asymptotic value for the excitation frequency is given by ω_{SP}, and the entire curve lies to the right of the light line. This implies that the SPP frequency is always lower than that of free-space radiation.

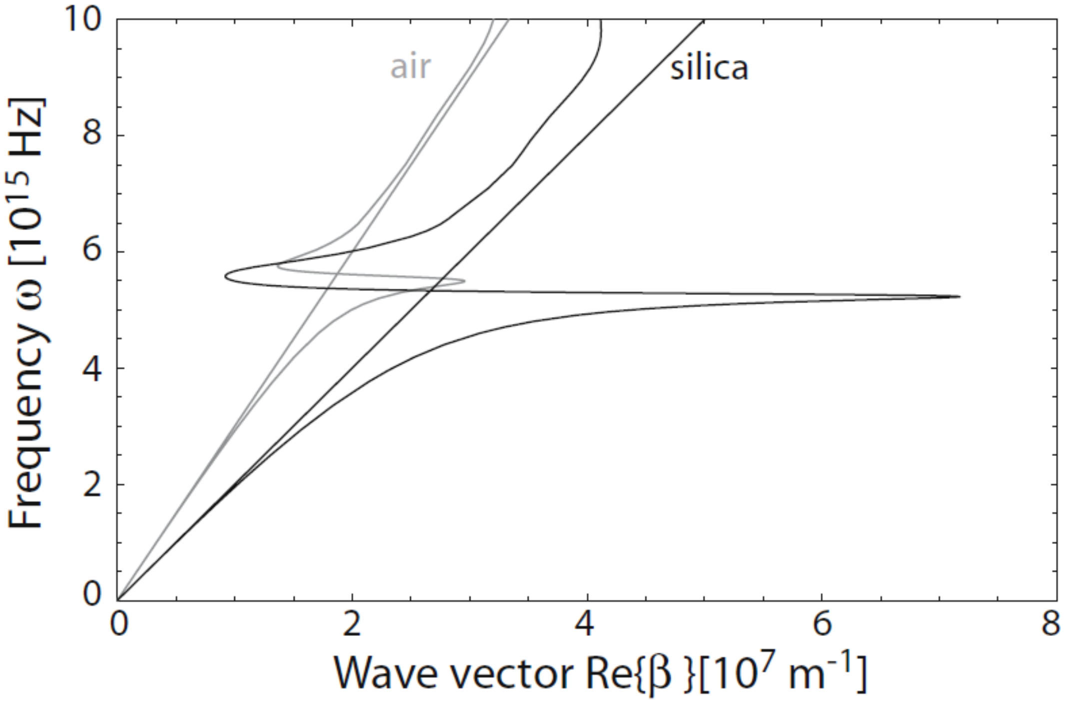

Figure 5.10: Dispersion relation for SPPs in the case of a damped electron gas.

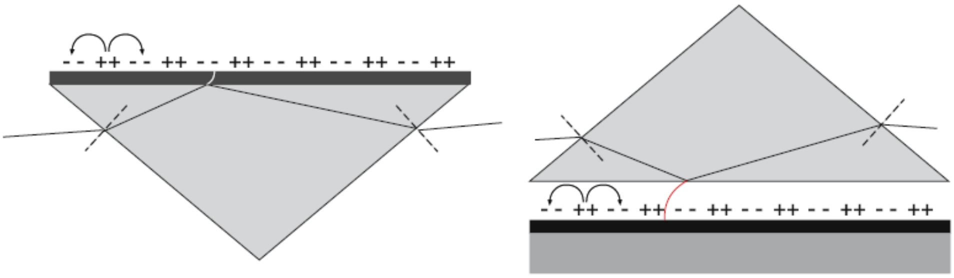

Figure 5.11: Prism coupling configurations. Left: the Kretschmann configuration can be used for thin films; the metal is evaporate onto the prism. Right: the Otto configuration can be used for thicker films and even bulk metals.

while in both cases the evanescent wave is generated at the prism surface, the SPP itself is not. The excitation is always generated at the *other* interface: the evanescent wave has to tunnel through the metal in one case, through the air in the other.

Applications of SPPs revolve around their ability of confining light at subwavelength scale. This is possible because the wavelength of the plasmonic excitations is much smaller than that of the exciting electromagnetic field. This could be exploited in plasmonic waveguides, which could guide electromagnetic radiation along paths much narrower than what is done today with fiber optics, or it could allow an optical characterization of small features below the traditional diffraction limit; in the latter case we speak about *scanning near-field optical microscopy* (SNOM).

Bibliography

[1] David S Ginley, Hideo Hosono, David C Paine, et al. *Handbook of transparent conductors*. Springer, 2010.

[2] Jenny Nelson. *The physics of solar cells*. World Scientific Publishing Company, 2003.

[3] US Geological Survey. *Mineral Commodity Summaries, 2009*. Government Printing Office, 2009.

[4] Stefan Alexander Maier. *Plasmonics: fundamentals and applications*. Springer Science & Business Media, 2007.

[5] Hiroshi Kawazoe, Masahiro Yasukawa, Hiroyuki Hyodo, Masaaki Kurita, Hiroshi Yanagi, and Hideo Hosono. P-type electrical conduction in transparent thin films of CuAlO2. *Nature*, 389(6654):939–942, 1997.

[6] Elias Burstein. Anomalous optical absorption limit in InSb [4]. *Physical Review*, 93(3):632–633, 1954.

[7] T. J. Coutts, D. L. Young, X. Li, W. P. Mulligan, and X. Wu. Search for improved transparent conducting oxides: A fundamental investigation of CdO, Cd2SnO4, and Zn2SnO4. *Journal of Vacuum Science & Technology A: Vacuum, Surfaces, and Films*, 18(6):2646–2660, 2000.

[8] B. E. Sernelius, K. F. Berggren, Z. C. Jin, I. Hamberg, and C. G. Granqvist. Band-gap tailoring of ZnO by means of heavy Al doping. *Physical Review B*, 37(17):10244–10248, 1988.

[9] S. Ghosh, A. Sarkar, S. Chaudhuri, and A. K. Pal. Grain boundary scattering in aluminium-doped ZnO films. *Thin Solid Films*, 205(1):64–68, 1991.

[10] Klaus Ellmer. Past achievements and future challenges in the development of optically transparent electrodes. *Nature Photonics*, 6(12):809–817, 2012.

[11] Neil W Ashcroft, N David Mermin, et al. *Solid state physics [by] Neil W. Ashcroft [and] N. David Mermin.* New York: Holt, Rinehart and Winston,, 1976.

[12] David C Look, Kevin D Leedy, Arnold Kiefer, Bruce Claflin, Naho Itagaki, Koichi Matsushima, and Iping Surhariadi. Model for thickness dependence of mobility and concentration in highly conductive zinc oxide. *Optical Engineering*, 52(3):033801, 2013.

[13] David C. Look. Mobility vs thickness in n+-ZnO films: Effects of substrates and buffer layers. *Materials Science in Semiconductor Processing*, 69(September 2016):2–8, 2017.

[14] Gururaj V Naik, Vladimir M Shalaev, and Alexandra Boltasseva. Alternative plasmonic materials: beyond gold and silver. *Advanced Materials*, 25(24):3264–3294, 2013.

[15] P.B. Johnson and R.W. Christy. Optical-Constants Of Noble-Metals Phys. Rev. B 6(12), 4370–4379 (1972). *Physical Review B*, 1318(1970):4370–4379, 1972.

[16] Jennifer A Dionne, Kenneth Diest, Luke A Sweatlock, and Harry A Atwater. Plasmostor: a metal- oxide- si field effect plasmonic modulator. *Nano letters*, 9(2):897–902, 2009.

[17] Ho W Lee, Georgia Papadakis, Stanley P Burgos, Krishnan Chander, Arian Kriesch, Ragip Pala, Ulf Peschel, and Harry A Atwater. Nanoscale conducting oxide plasmostor. *Nano letters*, 14(11):6463–6468, 2014.

[18] Ortwin Hess, John B Pendry, Stefan A Maier, Rupert F Oulton, Joachim M Hamm, and Kosmas L Tsakmakidis. Active nanoplasmonic metamaterials. *Nature materials*, 11(7):573, 2012.

[19] Jin-Soo Kim and Jin Tae Kim. Silicon electro-optic modulator based on an ito-integrated tunable directional coupler. *Journal of Physics D: Applied Physics*, 49(7):075101, 2016.

[20] U. Betz, M. Kharrazi Olsson, J. Marthy, M. F. Escolá, and F. Atamny. Thin films engineering of indium tin oxide: Large area flat panel displays application. *Surface and Coatings Technology*, 200(20-21):5751–5759, 2006.

[21] Hiromichi Ohta, Masahiro Orita, Masahiro Hirano, Hiroaki Tanji, Hiroshi Kawazoe, and Hideo Hosono. Highly electrically conductive indium–tin–oxide thin films epitaxially grown on yttria-stabilized zirconia (100) by pulsed-laser deposition. *Applied Physics Letters*, 76(19):2740–2742, 2000.

[22] Jia-Yu Lin, Kun-Da Zhong, and Po-Tsung Lee. Plasmonic behaviors of metallic AZO thin film and AZO nanodisk array. *Optics Express*, 24(5):5125, 2016.

[23] Chuanbin Wang, Sijun Luo, Qiang Shen, and Lianmeng Zhang. Effect of oxygen partial pressure on epitaxial growth and properties of laser-ablated AZO thin films. *Journal Wuhan University of Technology, Materials Science Edition*, 31(1):27–30, 2016.

[24] SooHo Cho, SungJoon Kim, YooShin Jo, and SangHo Kim. Electrical, Optical and Electrochemical Corrosion Resistance of AZO, GZO, AGZO Films Depending on the Hydrogen Content. *Journal of Nanoscience and Nanotechnology*, 19(7):3854–3858, 2019.

[25] SeungWook Shin, S.M. Pawar, Jong-Ha Moon, JinHyeok Kim, and SungDae Kim. Epitaxial Growth and Characterization of Highly Ga-doped ZnO ThinFilms Deposited on Al$_{2}$O$_{3}$ (0001) Substrates by Using the RFMagnetron Sputtering Method. *Journal of the Korean Physical Society*, 55(3(1)):1093–1097, 2009.

[26] Zhewei Wang, Chaonan Chen, Ke Wu, Haining Chong, and Hui Ye. Transparent conductive oxides and their applications in near infrared plasmonics. *physica status solidi (a)*, 216(5):1700794, 2019.

[27] Salah A Aly, Zhenning Kong, New Haven, and Emina Soljanin. (12) Patent Application Publication (10) Pub . No .: US 2009 / 0265141 A1. 1(61), 2009.

[28] Junxi Zhang, Lide Zhang, and Wei Xu. Surface plasmon polaritons: Physics and applications. *Journal of Physics D: Applied Physics*, 45(11), 2012.

[29] Tatjana Gric and Ortwin Hess. Controlling hybrid-polarization surface plasmon polaritons in dielectric-transparent conducting oxides metamaterials via their effective properties. *Journal of Applied Physics*, 122(19):1–8, 2017.

[30] Lorenzo Ferrari, Chihhui Wu, Dominic Lepage, Xiang Zhang, and Zhaowei Liu. Hyperbolic metamaterials and their applications. *Progress in Quantum Electronics*, 40:1–40, 2015.

[31] F Michelotti, L Dominici, E Descrovi, N Danz, and F Menchini. Thickness dependence of surface plasmon polariton dispersion in transparent conducting oxide films at 1.55 μm. *Optics letters*, 34(6):839–841, 2009.

[32] Kevin Santiago, Rajeh Mundle, Chandan B Samantaray, M Bahoura, and AK Pradhan. Nanopatterning of atomic layer deposited al: Zno films using electron beam lithography for waveguide applications in the nir region. *Optical Materials Express*, 2(12):1743–1750, 2012.

[33] Gururaj V. Naik, Jingjing Liu, Alexander V. Kildishev, Vladimir M. Shalaev, and Alexandra Boltasseva. Demonstration of Al:ZnO as a plasmonic component for near-infrared metamaterials. *Proceedings of the National Academy of Sciences of the United States of America*, 109(23):8834–8838, 2012.

[34] Yun Zhang, Tiaoxing Wei, Wenjing Dong, Chanyan Huang, Kenan Zhang, Yan Sun, Xin Chen, and Ning Dai. Near-perfect infrared absorption from dielectric multilayer of plasmonic aluminum-doped zinc oxide. *Applied Physics Letters*, 102(21), 2013.

[35] James ES Haggerty, Laura T Schelhas, Daniil A Kitchaev, John S Mangum, Lauren M Garten, Wenhao Sun, Kevin H Stone, John D Perkins, Michael F Toney, Gerbrand Ceder, et al. High-fraction brookite films from amorphous precursors. *Scientific reports*, 7(1):15232, 2017.

[36] Akira Fujishima and Kenichi Honda. Electrochemical photolysis of water at a semiconductor electrode. *nature*, 238(5358):37–38, 1972.

[37] MW Ribarsky. Titanium dioxide (tio2)(rutile). In *Handbook of optical constants of solids*, pages 795–804. Elsevier, 1997.

[38] Luca Mascaretti. *Hydrogen-treated titanium dioxide hierarchical nanostructures for water splitting applications*. PhD thesis, Italy, 2018.

[39] J Nowotny, T Bak, MK Nowotny, and LR Sheppard. Titanium dioxide for solar-hydrogen ii. defect chemistry. *International journal of hydrogen energy*, 32(14):2630–2643, 2007.

[40] WK Wong and MA Malati. Doped tio2 for solar energy applications. *Solar Energy*, 36(2):163–168, 1986.

[41] Vesna Đorđević, Bojana Milićević, and Miroslav D Dramićanin. Rare earth-doped anatase tio2 nanoparticles. *IntechOpen [online]. Copyright*, 2:25–52, 2017.

[42] Mitsunobu Iwasaki, Masayoshi Hara, Hiromi Kawada, Hiroaki Tada, and Seishiro Ito. Cobalt ion-doped tio2 photocatalyst response to visible light. *Journal of Colloid and Interface Science*, 224(1):202–204, 2000.

[43] Scot T Martin, Colin L Morrison, and Michael R Hoffmann. Photochemical mechanism of size-quantized vanadium-doped tio2 particles. *The Journal of Physical Chemistry*, 98(51):13695–13704, 1994.

[44] Yutaka Furubayashi, Taro Hitosugi, Yukio Yamamoto, Kazuhisa Inaba, Go Kinoda, Yasushi Hirose, Toshihiro Shimada, and Tetsuya Hasegawa. A transparent metal: Nb-doped anatase TiO2. *Applied Physics Letters*, 86(25):1–3, 2005.

[45] T. Hitosugi, A. Ueda, S. Nakao, N. Yamada, Y. Furubayashi, Y. Hirose, T. Shimada, and T. Hasegawa. Fabrication of highly conductive Ti1-x Nbx O2 polycrystalline films on glass substrates via crystallization of amorphous phase grown by pulsed laser deposition. *Applied Physics Letters*, 90(21):2–5, 2007.

[46] Meagen A. Gillispie, Maikel F.A.M. Van Hest, Matthew S. Dabney, John D. Perkins, and David S. Ginley. Rf magnetron sputter deposition of transparent conducting Nb-doped Ti O2 films on SrTi O3. *Journal of Applied Physics*, 101(3):3–7, 2007.

[47] Yasushi Sato, Hideo Akizuki, Toshihisa Kamiyama, and Yuzo Shigesato. Transparent conductive Nb-doped TiO2 films deposited by direct-current magnetron sputtering using a TiO2 - x target. *Thin Solid Films*, 516(17):5758–5762, 2008.

[48] Masahiko Matsubara, Rolando Saniz, Bart Partoens, and Dirk Lamoen. Doping anatase TiO2 with group V-b and VI-b transition metal atoms: A hybrid functional first-principles study. *Physical Chemistry Chemical Physics*, 19(3):1945–1952, 2017.

[49] Taro Hitosugi, Yutaka Furubayashi, Atsuki Ueda, Kinnosuke Itabashi, Kazuhisa Inaba, Yasushi Hirose, Go Kinoda, Yukio Yamamoto, Toshihiro Shimada, and Tetsuya Hasegawa. Ta-doped anatase tio2 epitaxial film as transparent conducting oxide. *Japanese journal of applied physics*, 44(8L):L1063, 2005.

[50] Piero Mazzolini. Functional Properties Control of Doped TiO2 for Transparent Electrodes and Photoanodes. page 157, 2015.

[51] P. Mazzolini, P. Gondoni, V. Russo, D. Chrastina, C. S. Casari, and A. Li Bassi. Tuning of electrical and optical properties of highly conducting and transparent Ta doped TiO2 polycrystalline films. *Journal of Physical Chemistry C*, 119(13):6988–6997, 2015.

[52] P. Mazzolini, V. Russo, C. S. Casari, T. Hitosugi, S. Nakao, T. Hasegawa, and A. Li Bassi. Vibrational-Electrical Properties Relationship in Donor-Doped TiO2 by Raman Spectroscopy. *Journal of Physical Chemistry C*, 120(33):18878–18886, 2016.

[53] Piero Mazzolini, Tolga Acartürk, Daniel Chrastina, Ulrich Starke, Carlo Spartaco Casari, Giuliano Gregori, and Andrea Li Bassi. Controlling the electrical properties of undoped and ta-doped TiO2 polycrystalline films via ultra-fast-annealing treatments. *Advanced Electronic Materials*, 2(3):1–9, 2016.

[54] Luca Ornago. Synthesis of tantalum-doped titanium oxide thin films: a bridge to infrared plasmonics. 2018.

[55] Robert Eason. *Pulsed laser deposition of thin films: applications-led growth of functional materials*. John Wiley & Sons, 2007.

[56] Carlo Spartaco Casari and Andrea Li Bassi. Pulsed laser deposition of nanostructured oxides: from clusters to functional films. 2011.

[57] Federica Romeo. Molybdenum coatings on rough graphite for applications in nuclear fusion devices and particle accelerators. 2019.

[58] Beatrice Roberta Bricchi, Matteo Ghidelli, Luca Mascaretti, Andrea Zapelli, Valeria Russo, Carlo Spartaco Casari, Giancarlo Terraneo, Ivano Alessandri, Caterina Ducati, and Andrea Li Bassi. Integration of plasmonic au nanoparticles in tio2 hierarchical structures in a single-step pulsed laser co-deposition. *Materials & Design*, 156:311–319, 2018.

[59] Anwar Ul-Hamid. *A Beginners' Guide to Scanning Electron Microscopy*. Springer, 2018.

[60] Ian R Lewis and Howell Edwards. *Handbook of Raman spectroscopy: from the research laboratory to the process line*. CRC Press, 2001.

[61] Andrea Li Bassi, Diego Cattaneo, Valeria Russo, Carlo Enrico Bottani, E Barborini, T Mazza, P Piseri, P Milani, FO Ernst, Karsten Wegner, et al. Raman spectroscopy characterization of titania nanoparticles produced by flame pyrolysis: the influence of size and stoichiometry. *Journal of Applied Physics*, 98(7):074305, 2005.

[62] Leo J van der Pauw. A method of measuring the resistivity and hall coefficient on lamellae of arbitrary shape. *Philips technical review*, 20:220–224, 1958.

[63] Paolo Gondoni. *Nanostructured transparent conducting oxides for advanced photovoltaic applications*. PhD thesis, Italy, 2014.

[64] J Tauc, Radu Grigorovici, and Anina Vancu. Optical properties and electronic structure of amorphous germanium. *physica status solidi (b)*, 15(2):627–637, 1966.

[65] Fabio Di Fonzo, Carlo Spartaco Casari, Valeria Russo, Maria Francesca Brunella, Andrea Li Bassi, and Carlo Enrico Bottani. Hierarchically organized nanostructured tio2 for photocatalysis applications. *Nanotechnology*, 20(1):015604, 2008.

[66] D Bruce Buchholz, Jun Liu, Tobin J Marks, Ming Zhang, and Robert PH Chang. Control and characterization of the structural, electrical, and optical properties of amorphous zinc- indium- tin oxide thin films. *ACS applied materials & interfaces*, 1(10):2147–2153, 2009.